GUIDING LINES

DIRECTING REACTION-DIFFUSION PROCESSES TO CREATE FUNCTIONAL MATERIALS

Ph.D. Thesis, University of Amsterdam, February 2024
Guiding Lines — Directing Reaction-Diffusion Processes to Create Functional Materials
Christiaan Thomas van Campenhout

Cover image:
The cover depicts a Turing pattern gradually transitioning into well-defined lines.
The cover was designed by Tom van Campenhout.

ISBN: 978-94-6506-533-5

The work described in this thesis was performed at
AMOLF, Science Park 104, 1098 XG, Amsterdam, The Netherlands.

This work is part of the Dutch Research Council (NWO). This research received funding from the Dutch Research Council (NWO) in the framework of the ENW PPP Fund for the top sectors and from the Ministry of Economic Affairs in the framework of the "PPS-Toeslagregeling".

A digital version of this thesis can be downloaded from
http://amolf.nl and https://dare.uva.nl/

All movies and scripts used in this thesis can be downloaded from
https://github.com/cvcampenhout/Scripts-and-Movies-Thesis.

Guiding Lines

Directing Reaction-Diffusion Processes to Create Functional Materials

ACADEMISCH PROEFSCHRIFT

ter verkrijging van de graad van doctor
aan de Universiteit van Amsterdam
op gezag van de Rector Magnificus
prof. dr. ir. P.P.C.C. Verbeek
ten overstaan van een door het College voor Promoties ingestelde commissie,
in het openbaar te verdedigen in de Aula der Universiteit
op woensdag 11 december 2024, te 11.00 uur

door Christiaan Thomas van Campenhout
geboren te Amsterdam

Promotiecommissie

Promotores:	prof. dr. W.L. Noorduin	Universiteit van Amsterdam
	prof. dr. M.L. van Hecke	Universiteit Leiden
Overige leden:	prof. dr. J.N.H. Reek	Universiteit van Amsterdam
	prof. dr. K. Keune	Universiteit van Amsterdam
	dr. J.A. Kaandorp	Universiteit van Amsterdam
	prof. dr. M.M.G. Kamperman	Rijksuniversiteit Groningen
	dr. M.M. Lerch	Rijksuniversiteit Groningen

Faculteit der Natuurwetenschappen, Wiskunde en Informatica

"I got stripes"

Johnny Cash

Contents

1 Introduction **1**
- 1.1 Form and function: complex functional materials . . . 1
- 1.2 Natural Patterns and Self-Organization . . . 2
- 1.3 Reaction-Diffusion Processes . . . 3
- 1.4 Liesegang Patterning . . . 7
- 1.5 Liesegang Materials . . . 9
- 1.6 Applications of Reaction-Diffusion Processes . . . 11
- 1.7 Diffusion Limitations . . . 12
- 1.8 Aim of this Thesis . . . 14

2 Reaction-Diffusion Processes in Mechanically Responsive Hydrogels **17**
- 2.1 Introduction . . . 18
- 2.2 Results and Discussion . . . 20
- 2.3 Conclusion . . . 26
- 2.4 Materials and Methods . . . 27
- 2.5 Supporting Information . . . 29

3 Patterning Complex Line Motifs in Thin-Films Using Immersion-Controlled Reaction-Diffusion **37**
- 3.1 Introduction . . . 38
- 3.2 Results and Discussion . . . 41
- 3.3 Conclusion . . . 48
- 3.4 Materials and Methods . . . 50
- 3.5 Supporting Information . . . 52

4 Photography Inspired Customization of Micropatterned Thin-Films **55**
- 4.1 Introduction . . . 56
- 4.2 Results and Discussion . . . 59
- 4.3 Conclusion . . . 65
- 4.4 Supporting Information . . . 67

5 Reaction-Diffusion Modeling **73**
5.1 Reaction-diffusion modeling 74
5.2 Reaction-diffusion coupled to mechanical responsiveness 79
5.3 Immersion controlled reaction-diffusion 81
5.4 Downscaling Liesegang patterning 83

1 Introduction

1.1 Form and function: complex functional materials

Spatial organization of components can enhance and exceed properties of materials beyond what would be achievable by simply the sum-of-their-parts[1–5]. As such, patterned materials are key for the next generation of advanced functional materials[6–9]. From cooling applications (Figure 1.1A)[10], to data- (Figure 1.1B)[11], and energy storage (Figure 1.1C)[12], careful shaping of materials into well-defined architectures provides functionalities beyond those of their components. Take for instance this example of structural color: by creating well-defined shapes, specific wavelengths of light are preferentially reflected back, resulting in vibrant colors made from colorless materials (Figure 1.1D)[13]. Another example of patterns providing functionality is found in diffraction gratings, optical devices where a nano- or microscopic periodic structure splits and disperses light (Figure 1.1E)[14]. These diffraction gratings are currently found in many high-tech applications, such as 3D displays[15], biomedical monitoring devices[16], and laser systems[17].

Currently, complex nanomaterials are almost exclusively made using lithography techniques. In such processes, shapes are drawn either by etching with an electron beam or produced photo-chemically with ultraviolet light. These precise patterning techniques manufacture the most advanced chips currently in circulation, but are incredibly high-tech and thus expensive. Additionally, because every feature has to be drawn by either an e-beam or UV light, these processes are inherently poorly scalable: producing a nanoscale diffraction grating of centimeter size requires drawing tens of thousands individual stripes. Therefore, alternative routes towards complex functional materials are highly sought after.

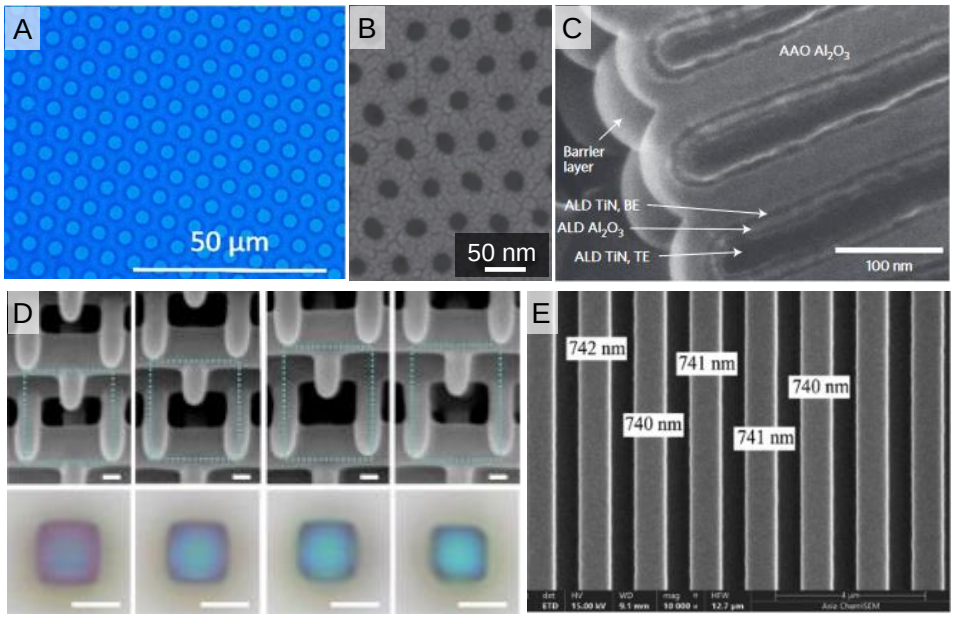

FIGURE 1.1: Complex functional materials. (A) Microcylinder array for cooling applications, reprinted from Akkerboom et al.[10] (B) Nanocapacitor for data storage, reprinted from Lee et al.[11] (C) Nanocapacitor for high-efficiency energy storage, reprinted from Banerjee et al.[12] (D) Heat-sensitive structural color from 3D-printed photonic crystals. SEM scale bars represent 100 nm and micrograph scale bars represent 5 µm, reprinted from Liu et al.[13] (E) Optical diffraction grating, reprinted from Gu et al.[14]

1.2 Natural Patterns and Self-Organization

Nature possesses the remarkable ability to produce functional complex shapes and patterns seemingly out of thin air. Examples of such patterns are found on the skin or fur of animals (Figure 1.2A-C), but also on much smaller scales, such as the structures giving Morpho butterflies their bright blue wings (Figure 1.2D, E) or the iridescent nacreous shell of oysters (Figure 1.2F, G). For this, nature relies on self-organization: autonomous processes where building blocks spontaneously arrange into complex shapes and patterns, driven by local physical and chemical interactions. In the following sections we will describe how local interactions can lead to pattern formation, and how such processes can potentially be used to generate functional materials. Specifically, we will introduce a fundamental class of processes that can result in self-organization: reaction-diffusion systems.

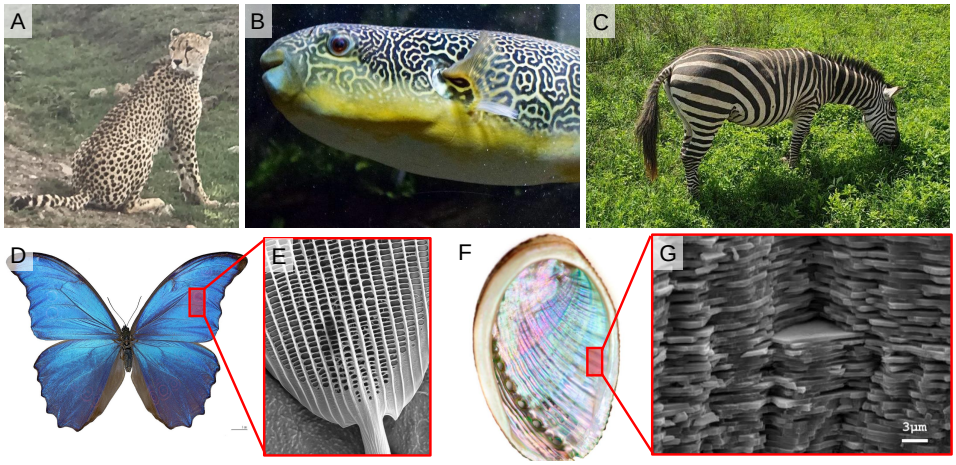

FIGURE 1.2: Natural shapes and patterns. (A) A jaguar with dot patterned fur. (B) A pufferfish with a distinct Turing pattern on its skin, image by Tiia Monto[18]. (C) Zebra stripes. (D) Structural colored morpho butterfly, image by Didier Descouens[19], with (E) an SEM micrograph of the complex nanostructures giving color to the wing. (F) Iridescence of a mother-of-pearl oyster shell, with (G) an SEM micrograph of the nanoscale $CaCO_3$ platelets that generate structural color, micrograph by Fabian Heinemann[20].

1.3 Reaction-Diffusion Processes

In 1952, the British mathematician Alan Turing published *The Chemical Basis of Morphogenesis*, an article in which he describes how "a good knowledge of mathematics, some biology, and some elementary chemistry" can actually describe many of the patterns found in the natural world[21]. Turing demonstrates that systems where there exists some form of short-range promotion and long-range inhibition, can spontaneously generate spatial inhomogeneities, even from perfectly homogeneous starting conditions. In particular, Turing discusses so-called reaction-diffusion (RD) systems, where the combination of chemical reactivity and diffusion provides complex chemical feedback loops to generate patterns. To understand how RD systems generate patterns, we investigate their main components. All RD systems can be described by the following differential equation, here shown for a one dimensional system (Equation 1.1)[22]:

$$\frac{\partial u}{\partial t} = D\frac{\partial^2 u}{\partial x^2} + R(u). \tag{1.1}$$

This equation describes the change in concentration of a certain species u, as a result of two components: 1. a diffusion term in the form of Fick's second law, where D is the diffusion coefficient of species u, and 2. a reaction term that describes any reactivity of species u. Here we will briefly expand on these two components.

1.3.1 Diffusion

Diffusion describes the movement of a species as a result of a concentration gradient. Specifically, a species will spontaneously move from high concentration regions to low concentration regions. Here we show a numerical example of diffusion (Figure 1.3A), where we initially have introduced a high concentration of a species in the center of the system ($t = 0$). Because there exists a sharp concentration gradient, the species will diffuse away from the center, spreading the species throughout the system ($t = 2$). As time continues, the species will spread even further towards the edges ($t = 10$), until eventually the concentration equilibrates ($t = 500$) and is evenly distributed throughout the system. In short, diffusion causes spatial concentration gradients to slowly equilibrate.

1.3.2 Chemical Reactions and Autocatalysis

Besides diffusion, RD systems require some transformation of species, described by the reaction term in the equation above (Equation 1.1). Such a transformation can for instance be gene expression in cells[23], or even a fox getting infected with rabies[24]. In this thesis we focus on chemical RD systems, where this transformation is the result of one or more chemical reactions. A simple chemical reaction can be described as follows (Equation 1.2):

$$A + B \xrightarrow{k_1} C, \tag{1.2}$$

where A and B are two reactants and C is some product. The rate at which product C is formed by such a reaction can be described by a second-order rate equation (Equation 1.3):

$$\frac{\partial [C]}{\partial t} = k_1 [A][B] \tag{1.3}$$

where k is a rate constant and [A] and [B] are the concentrations of A and B respectively. Second-order reactions alone will not result in Turing patterns, or any other complex behavior, because for that some feedback mechanism is required. One example of such a feedback mechanism is an autocatalytic reaction, where a reaction product actually works as a catalyst to accelerate the reaction rate (Equation 1.4)[25,26]:

$$A + B + C \xrightarrow{k_{cat}} C, \tag{1.4}$$

Including the autocatalytic reaction, the rate equation then becomes (Equation 1.5):

$$\frac{\partial[C]}{\partial t} = [A][B](k_1 + k_{cat}[C]). \tag{1.5}$$

This rate equation shows that the reaction speeds up in the presence of its product, and therefore is self-amplifying and non-linear, especially when $k_{cat} >> k_1$. Such self-amplification provides the short-range activation required for RD. Besides autocatalytic reactions, many more self-amplifying mechanisms exist, from crystallization, where growth rates are related to the crystal surface, to self-amplifying mRNA vaccines[27].

As described by Turing, RD systems need both short-range activation and long-range inhibition and it is precisely the unique combination of chemical reactivity and diffusion that provides both. Here we show a concept reaction-diffusion system (Figure 1.3B), based on an autocatalytic process: from homogeneous starting conditions a stochastic reaction occurs, locally creating an inhomogeneity. Here, this inhomogeneity is self-amplifying, and thus rapidly converts the neighboring material. However, in order to convert material, reactant is required. This reactant is thus rapidly consumed near the inhomogeneity, creating a concentration gradient, causing diffusion to transport the reactant from the surrounding area to the inhomogeneity. This transport depletes the surrounding area of reactant, which prevents formation of any new reactive site, effectively inhibiting all areas distant from the initial inhomogeneity. The end result then becomes areas with high product concentration (shown in green) and areas without product (shown in red), spatially separated by an initial stochastic event.

Numerical modeling reveals that a wide variety of spatial patterns can be created with such autocatalysis-depletion RD systems, from jaguar spots and zebra stripes to the complex Turing patterns found on a pufferfish (Figure 1.2B). In some cases, the spatial inhomogeneities generated by RD are not permanent, as is the case in the famous Belousov-Zhabotinsky (BZ) reaction, where many complex coupled autocatalytic reactions provide mesmerizing colored oscillations.

Comparing the RD patterns shown (Figure 1.3C, D) to functional nanomaterials (Figure 1.1) shows that RD patterns are much more disordered, with many misaligned patches as opposed to well-defined and well-aligned features. This is a result of the homogeneous starting conditions used to create these patterns: because there is no directionality in the system, there is no preferential orientation for any region to adhere to and thus patches form with random orientation, resulting in disordered patterns. For the production of functional materials, patterns require a high degree of ordering and thus require directionality to be imparted onto the system.

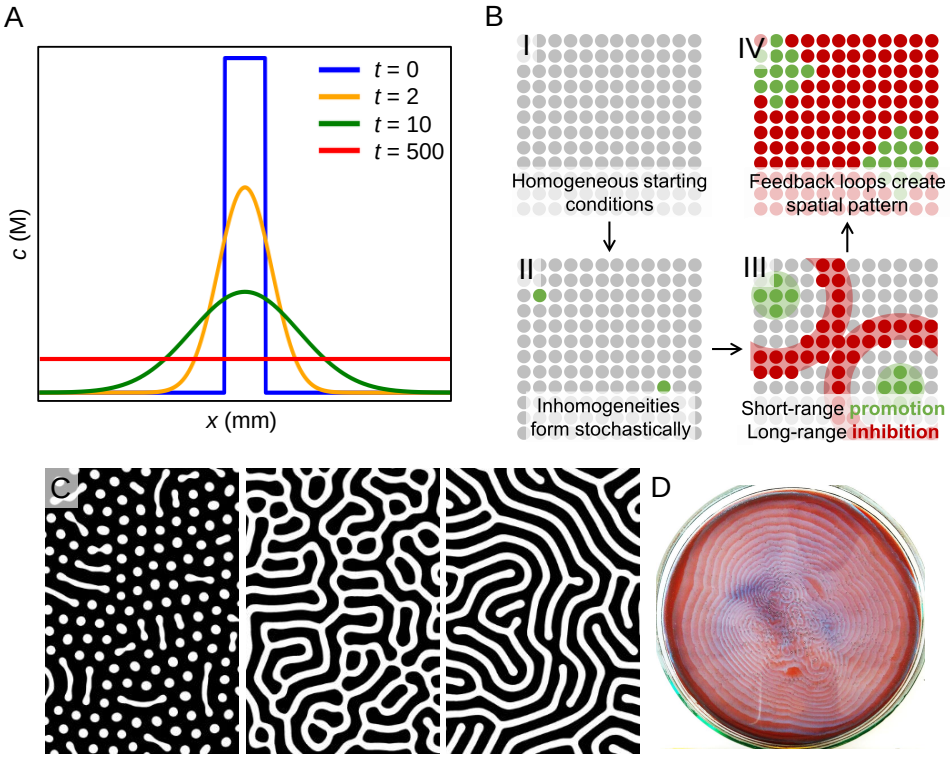

FIGURE 1.3: Reaction-diffusion systems. (A) Modeled development of a concentration profile by diffusion over time. (B) Schematic representation of an autocatalytic-depletion RD system. (C) Schematic turing patterns. (D) Snapshot of the Belousov-Zhabotinsky reaction performed in a petri-dish, image by Wiktor[28].

1.4 Liesegang Patterning

One type of reaction-diffusion system that shows such directionality is called Liesegang patterning[29]. In such a system, a simple precipitation is performed by mixing two solutions that produce an insoluble product. For instance, mixing a solution of silver nitrate with a solution of potassium dichromate will induce precipitation of the insoluble silver dichromate (Figure 1.4A). In a typical high school experiment, such a precipitation reaction is performed in water, and subsequently a cloud of precipitate is formed, which sediments over time. The trick in Liesegang patterning is to perform the same precipitation reaction, but now inside of a hydrogel. Initially, the reactants are spatially separated by dissolving one reactant in the gel, called the gel reagent (GR) and dissolving the second reactant in a solution that is placed on top of the gel, called the immersion or infiltrating reagent (IR). This spatial separation creates a strong concentration gradient, inducing diffusion of the IR into the gel network, where it reacts with the GR to form an insoluble product. Remarkably, this insoluble product is not dispersed evenly throughout the gel, but instead produces distinct precipitation bands perpendicular to the direction of diffusion (Figure 1.4B, C). In such processes, the gel plays a critical role: it prevents sedimentation of the precipitate, ensuring that any pattern formed stays in place, and prevents convective flow, allowing only diffusive transport to occur. Having diffusion as the only means of transport is critical to produce highly ordered precipitation bands with uniform directionality.

To understand why diffusion controlled transport is so important, we need to look into the mechanisms underlying Liesegang pattern formation. Although tremendous research has been conducted into these processes, the key steps leading to pattern formation are still not well understood. Nevertheless, multiple convincing theories exist that can describe many of the experimentally observed patterns. These theories can be divided into two main classes: pre-nucleation or post-nucleation. In this thesis, we work exclusively with Liesegang processes that are accurately described by pre-nucleation models and therefore that is where our focus lies. For a more detailed discussion on the complexities of Liesegang patterning, including descriptions of both pre- and post-nucleation models, see[30]. In a typical Liesegang process, the following reaction and crystallization steps are key (Equations 1.6 - 1.8):

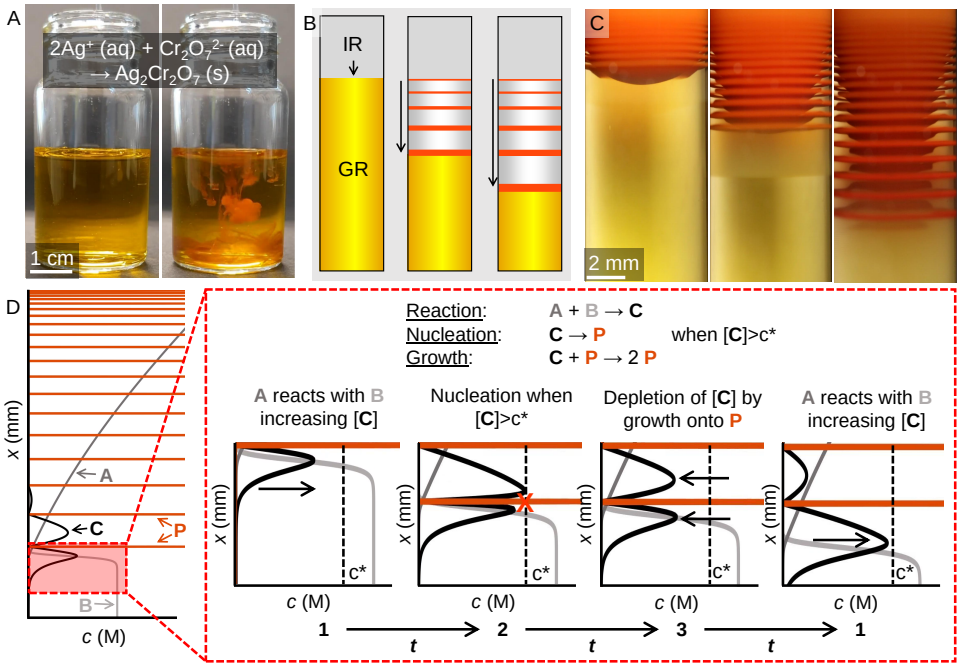

FIGURE 1.4: Liesegang patterning. (A) Precipitation induced by adding drops of silver nitrate to a solution of potassium dichromate. (B) Schematic representation of Liesegang patterning. (C) Liesegang pattern obtained with silver nitrate as IR and potassium dichromate as GR inside a gelatin hydrogel. (D) Propagation of concentration gradients of all species during the Liesegang process, following pre-nucleation theory.

$$Reaction: A(aq) + B(aq) \rightarrow C(aq) \tag{1.6}$$

$$Nucleation: C(aq) \rightarrow P(s), if\ [C] > c^* \tag{1.7}$$

$$Growth: C(aq) + P(s) \rightarrow 2P(s) \tag{1.8}$$

Where A is the IR, B is the GR, C is the poorly soluble product, P is the final precipitate and c* is the nucleation threshold.

Typically, Liesegang patterning is initiated by placing a solution of A in contact with a gel containing B. From this initial interface, A will diffuse into the gel matrix and react with B to form the poorly soluble product C (Figure 1.4D 1). As the concentration of C gradually increases due to the influx of A and subsequent reaction with B, the supersaturation of C in the gel increases. If this supersaturation becomes high enough ([C] > c*), a nucleus of solid precipitate P will form (Figure 1.4D 2). Growth onto this nucleus is autocatalytic, and extremely fast, depleting the surrounding area of C (Figure 1.4D 3). Because of this depletion, the concentration of C quickly falls below the nucleation threshold, and therefore no new nuclei will form. Whilst all this is happening, A is still diffusing further into the gel, where it continues to react with B to form new C (Figure 1.4D 1). Only far enough from the previously formed nucleus, the concentration of C can increase again to become supersaturated, after which nucleation can again occur. This reaction-diffusion feedback loop thus autonomously produces spatially separated regions with and without precipitation. By having a directional diffusion gradient, these regions are aligned, creating well-defined precipitation bands perpendicular to the diffusion direction.

1.5 Liesegang Materials

Even though the pre-nucleation model appears general for any precipitation reaction, relatively few materials in specific gel matrices demonstrate Liesegang patterning. Apparently, a delicate balance between diffusion of all species, nucleation and subsequent growth, and chemical reactivity is required to produce a pattern. However, the precise requirements of Liesegang patterning are poorly understood, mainly because nucleation is a sub-nanometer process, and therefore extremely difficult to observe in situ. Nonetheless, through trial-and-error, as well as serendipity, several robust Liesegang patterning systems have been developed.

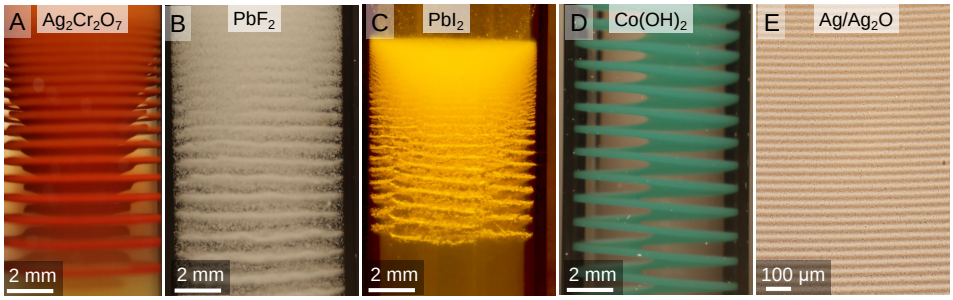

FIGURE 1.5: Liesegang patterns made of different materials (A) The original Liesegang pattern of silver dichromate. (B) Lead fluoride pattern produced by diffusion lead acetate into agarose containing potassium fluoride. (C) Lead iodide pattern produced by diffusing lead acetate into an agarose gel containing potassium iodide. (D) Cobalt hydroxide spiral grown by diffusing cobalt ions into an agarose gel containing ammonium hydroxide. (E) Optical microscopy image of a Liesegang pattern consisting of silver nanoparticles arranged in microscopic stripes.

The very first Liesegang system was a serendipitous discovery, made in the late 19th century by the German scientist and photographer after whom the process is named: R. E. Liesegang. The story goes that Liesegang, being a photographer working with silver halide photographs, at some point accidentally dropped a silver nitrate crystal onto a gelatin film, containing potassium dichromate. Instead of a simple stain, this accidental act created the first ever Liesegang patterns, consisting of silver dichromate (Figure 1.5A). This silver dichromate system is studied to this day and produces some of the most striking Liesegang patterns. After this seminal work, Liesegang patterns were produced of magnesium hydroxide[31], lead fluoride (Figure 1.5B), lead iodide (Figure 1.5C), cobalt hydroxide (Figure 1.5D), cobalt phosphate and copper chromate. Currently, Liesegang patterning is not as widely studied as it was in the early 20th century, however, more recent work developed an exciting microscopic Liesegang system, where silver nanoparticles are formed inside a gelatin hydrogel in well-defined microscopic stripes (Figure 1.5E)[32]. In short, while several Liesegang patterning systems exist, it is still poorly understood what makes a material show this type of patterning behavior. Nonetheless, exciting opportunities exist for Liesegang patterns and reaction-diffusion processes as whole.

1.6 Applications of Reaction-Diffusion Processes

In the past few decades, researchers have realized that Liesegang patterns are not only an interesting curiosity, but actually hold the potential to autonomously create functional materials. Most notably, the work of Grzybowski has demonstrated this potential of Liesegang patterning to generate complex materials, with interesting optical applications, such as the Fresnel lenses shown here (Figure 1.6A)[33]. Additionally, Liesegang patterning, and RD processes in general, can be used for sensing. Because Liesegang patterns take time to develop, environmental changes during the patterning process are imprinted and thus saved. Using such an approach, researchers have developed a compression sensor, by performing Liesegang patterning in a compressible gel matrix (Figure 1.6B)[34], as well as a temperature sensor (Figure 1.6C)[35]. In different work, researchers have shown that performing a RD nanoparticle synthesis provides spatial morphology control, where different nanoparticle morphologies are obtained at different locations of the system, based on the distance from an initial interface, highlighting the controlled and precise reaction conditions generated by RD (Figure 1.6D)[36]. While these applications are exciting, they are few in number, suggesting that fundamental limitations exist that hinder successful applications of Liesegang patterning and reaction-diffusion processes in general.

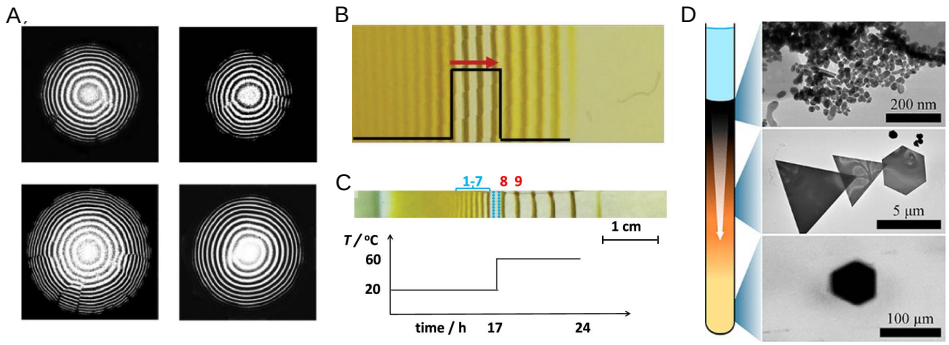

FIGURE 1.6: Applications of reaction-diffusion. (A) Fresnel lenses produced by a Liesegang patterning process called WETS, reprinted from Campbell et al.[33] (B) Compression sensing using Liesegang patterning, reprinted from Morsali et al.[34] (C) Temperature sensing using Liesegang patterning, reprinted from Khan et al.[35] (D) Morphology control during nanoparticle synthesis with RD, reprinted from Farkas et al.[36]

1.7 Diffusion Limitations

Surprisingly, the main limitation hindering reaction-diffusion based fabrication of functional materials lies in one of its two main constituents: diffusion. Diffusion hampers applicability in three ways: 1. the total size of the system is severely limited, because diffusion is slow over long distances, 2. the patterns generated by RD are non-uniform, because reaction conditions near the initial interface are not equal to those further along the system, and 3. the tunability and shaping of patterns is difficult, because of the autonomy of the process. These limitations, which are inherent to diffusion driven processes, render large-scale fabrication of complex functional materials using RD practically impossible.

The reason diffusion imposes these limitations lies in the driving force of this transport mechanism: diffusion moves species as a result of concentration gradients. Because of diffusion, concentration gradients spread out, and thus become less steep over time, resulting in a lower driving force for diffusion. This self-limiting effect makes diffusion slow down over time and ineffective for transporting species over long distances. The distance a species travels over time as a result of diffusion can be described as (Equation 1.9):

$$x_f = 2\sqrt{Dt}, \tag{1.9}$$

where x_f is the diffusion length scale, a descriptor for the distance traveled by the diffusing species, D is the diffusion coefficient of that species, and t is time.

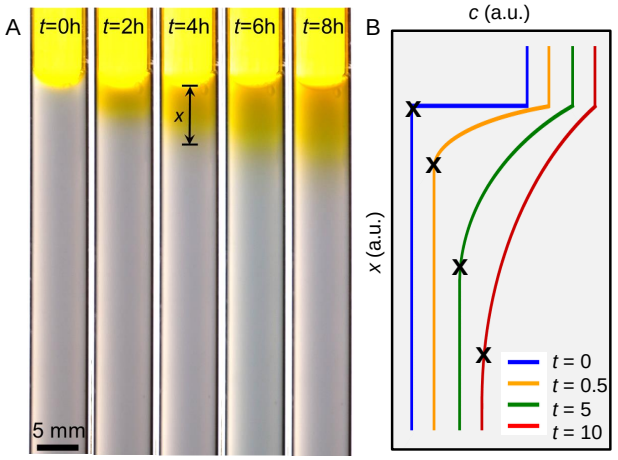

FIGURE 1.7: Diffusion limitations. (A) Diffusive transport of the dye fluorescein into a gelatin hydrogel. (B) Numerical simulation of diffusive transport with a fixed reservoir concentration, highlighting the changing concentration gradient.

From this equation it becomes clear that as time progresses, diffusive transport indeed slows down. This is experimentally demonstrated when a solution of fluorescein is placed on top of a gelatin hydrogel and allowed to diffuse (Figure 1.7A). Evident from this experiment, and confirmed by numerical simulations (Figure 1.7B), diffusion causes concentration gradients to become less and less steep over time, resulting in different reaction conditions at every position in the system. Diffusion thus poses a strange conundrum: on the one hand it is crucial for the functioning of RD processes, but on the other it drastically limits their scalability and therefore applicability. Unlocking the full potential of RD processes for the self-organization of functional materials thus requires the development of a fundamentally different approach; one that overcomes the limitations inherent to diffusion, whilst retaining the control and order of diffusion driven pattern formation.

1.8 Aim of this Thesis

In this thesis, we aim to overcome the classical limitations of Liesegang patterning, to enable reaction-diffusion driven self-organization of large-scale complex functional materials. To this end, we develop fundamentally new principles for Liesegang patterning and introduce two strategies to overcome diffusive limitations inherent to reaction-diffusion: mechanically responsive hydrogels and immersion controlled patterning. Subsequently, we demonstrate that patterns can be post-processed by applying photography inspired manipulation processes, to contour and convert patterns into user-defined shape and chemical composition. Lastly, we describe the numerical reaction-diffusion model used in chapters 2 and 3. Here follows a brief summary of each chapter in this thesis.

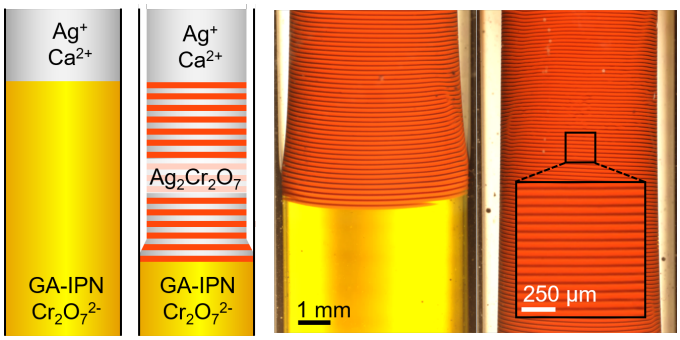

FIGURE 1.8: Chapter 2: By embedding the Liesegang process in mechanically responsive hydrogels we overcome diffusion limitations to generate highly uniform patterns on large scale.

In chapter 2, we introduce a strategy to overcome diffusive limitations of RD by embedding the Liesegang process in mechanically responsive hydrogels (Figure 1.8). Here, coupling between a moving reaction front and hydrogel contraction induces the formation of a self-regulated transport channel that ballistically carries reactants towards the area where patterning occurs. This ensures rapid and uniform patterning. Specifically, large-scale ($> 5cm$) uniform banding patterns are produced with tunable band distance. By overcoming the inherent limitations of diffusion, this strategy unlocks the potential of reaction-diffusion processes for the manufacturing of uniformly layered materials.

In chapter 3, reaction-diffusion driven, immersion controlled patterning (R-DIP) is introduced, a self-organization strategy using immersion controlled reaction-diffusion for targeted line patterning in thin films (Figure 1.9). By modulating immersion speeds, the movement of a reaction-diffusion front over gel films is controlled, which induces precipitation of highly uniform lines at the reaction front. A balance between the immersion speed and diffusion provides both hands-on tunability of the line spacing ($d = 10 - 300$ μm) as well as error-correction against defects. This immersion-driven patterning strategy is widely applicable, which is demonstrated by producing line patterns of silver/silver oxide nanoparticles, silver chromate, silver dichromate, and lead carbonate. Through combinatorial stacking of different line patterns, hybrid materials with multi-dimensional patterns such as square-, diamond-, rectangle- and triangle-shaped motifs are fabricated. The functionality potential and scalability is demonstrated by producing both wafer-scale diffraction gratings with user-defined features as well as an opto-mechanical sensor based on Moiré patterning.

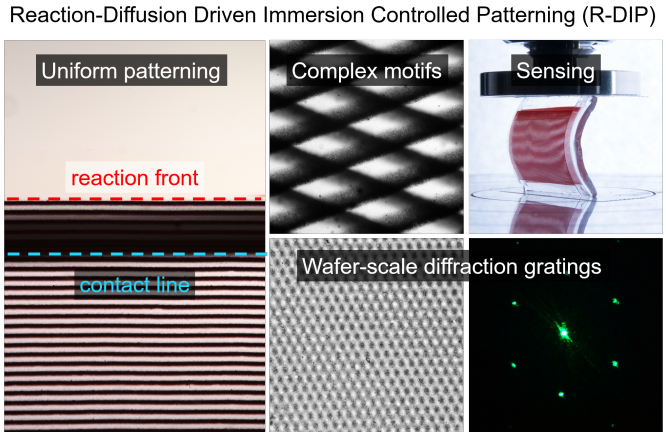

FIGURE 1.9: Chapter 3: We introduce reaction-diffusion driven, immersion controlled patterning to generate complex motifs, wafer-scale diffraction gratings, and a sensor based on Moiré patterning.

In chapter 4, we introduce a strategy to shape and convert self-organized micropatterned thin-films (MPF's) into complex motifs using photography inspired manipulation processes (Figure 1.10). By tapping into a century's worth of photographic research, we contour and chemically convert patterns. Inspired by composite photography, we design stacks of MPF layers, in which the shape and composition of each layer is controlled, to create complex tapestries.

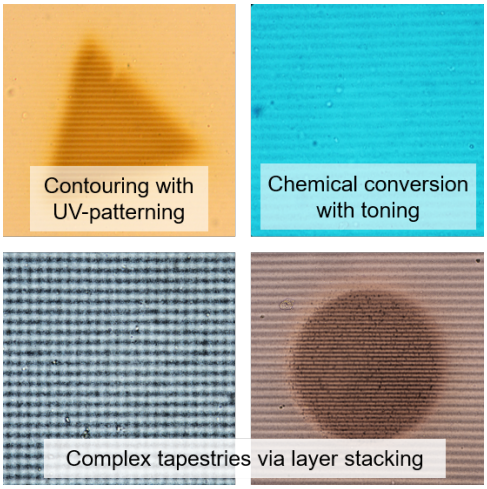

FIGURE 1.10: Chapter 4: We introduce photography inspired manipulation of self-organized thin films. With this strategy, we expand the design space of patterns generated with reaction-diffusion processes and demonstrate this by creating complex tapestries of micropatterned layers, where each layer has a tunable pattern, shape and chemical composition.

In chapter 5 we discuss the numerical model used throughout this work. First, we explain the basics of reaction-diffusion modeling, and then we introduce the different versions of the model used in this thesis. Lastly, we describe some key lessons learned from these numerical models regarding reaction-diffusion pattern formation, specifically looking at key parameters that define pattern spacing.

All scripts and movies described and used in this thesis are publicly available for download via: `https://github.com/cvcampenhout/Scripts_thesis`.

2 Reaction-Diffusion Processes in Mechanically Responsive Hydrogels

Straightforward manufacturing pathways towards large scale, uniformly layered composites may enable the next generation of materials with advanced optical, thermal, and mechanical properties. Reaction-diffusion systems are attractive candidates to this aim, but while layered composites theoretically could spontaneously arise from reaction-diffusion, in practice randomly oriented patches separated by defects form, yielding non-uniformly patterned materials. A propagating reaction front can prevent such non-uniform patterning, with Liesegang processes in which a moving reaction front produces aligned layers of precipitate playing a key role. However, while diffusion is crucial to control the patterning, it slows down transport of reactants to the front and results in a steady increase of the band spacing as the front advances. Here we circumvent these diffusive limitations by embedding the Liesegang process in mechanically responsive hydrogels. The coupling between a moving reaction front and hydrogel contraction induces the formation of a self-regulated transport channel that ballistically carries reactants towards the area where patterning occurs. This ensures rapid and uniform patterning. Specifically, large-scale ($> 5cm$) uniform banding patterns are produced with tunable band distance ($d = 60 - 160$ μm) of silver dichromate crystals inside responsive gelatin-alginate hydrogels. The generality and applicability of our mechano-reaction-diffusion strategy is demonstrated by forming patterns of precipitates in significantly smaller microscopic banding patterns ($d = 10 - 30$ μm) that act as self-organized diffraction gratings. By circumventing the inherent limitations of diffusion, our strategy unlocks the potential of reaction-diffusion processes for the manufacturing of uniformly layered materials.

The work described in this chapter is published in:
C. T. van Campenhout, D. N. ten Napel, M. van Hecke and W. L. Noorduin, *Proc. Natl. Acad. Sci*, **2022,** 119 (39): e2123156119.

2.1 Introduction

Self-organization strategies offer powerful routes for the fabrication of the next generation of complex structured materials with advanced functionalities[37,38]. Such self-organization approaches may be particularly advantageous for the fabrication of uniformly layered materials because of their desirable mechanical, optical and electronic properties[39–46]. Whilst such layered materials have gained tremendous attention, their manufacturing remains challenging. Therefore, simple routes towards uniformly layered materials are of fundamental interest with practical ramifications for new manufacturing approaches.

A potentially powerful self-organized manufacturing approach is offered by reaction-diffusion (RD) systems, where a delicate balance between reaction and diffusion rates induces the spontaneous formation of spatial patterns[21,38,47–49]. In theory, such patterns could spontaneously arrange into uniform layers[50]. In practice, however, differently oriented patches separated by defects occur and experimental inhomogeneities lead to additional deviations from uniform patterning.

In order to align patches and prevent defects, patterns can be produced with a moving reaction front, generating the pattern layer-by-layer in a time-ordered manner. The archetypical example of such a system is the Liesegang process[29,51–54]. In such a system, a well-defined chemical gradient is established by placing a solution of an outer electrolyte (OE) on top of a gel matrix containing an inner electrolyte (IE) (Figure 2.1A). The OE diffuses into the gel matrix, resulting in an OE front that moves through the gel and reacts with the IE to form an insoluble product, which precipitates at the precipitation front (x_f). This precipitate is not evenly dispersed throughout the gel matrix, but rather in the form of a characteristic banding pattern, with non-uniform band spacing and band width. The non-uniform patterning behavior can be explained as follows: over time, as the OE diffuses further into the gel matrix, the diffusive zone length (g) is increased, resulting in decreasing OE concentrations at the precipitation front, causing bands to appear progressively further apart.

The non-uniform bands produced by such Liesegang processes are undesirable for most applications. On small scales (< 0.1 cm), this non-uniform behavior is less severe and reaction-diffusion has been applied successfully for the microfabrication of optical and electronic components, as well as composite-like materials[33,55,56]. On larger scales (> 0.1 cm), however, the increased diffusive zone inherently limits practical applicability of reaction-diffusion processes: diffusion renders pattern formation slow and produces non-uniform layers[22]. Unlocking the full potential of the Liesegang process for the self-organization of functional materials thus requires the development of a fundamentally different approach; one that overcomes the limitations inherent to diffusion, whilst retaining the control and order of diffusion driven pattern formation.

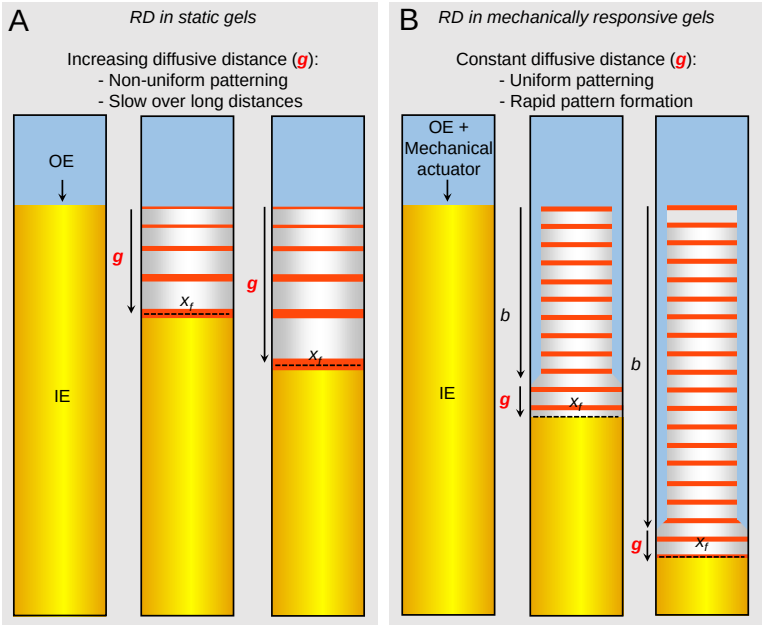

FIGURE 2.1: Schematic representation of the here-introduced concept of reaction diffusion in mechanically responsive gels (MRG). (A) Classical Liesegang-type pattern formation. Note the increasing diffusive distance g and subsequent non-uniform patterning. (B) Pattern formation in MRGs. Note the constant diffusive distance g and subsequent uniform patterning.

In this work, we present a strategy to overcome these limitations by embedding the RD process in a mechanically responsive gel (MRG), instead of a conventional static gel (SG) (Figure 2.1B). The central idea is that contraction of the gel in response to a mechanically actuating chemical that is added to the OE induces the self-regulated formation of a transport channel that follows the precipitation front at a constant distance. This transport channel effectively divides the system into two zones: a mixing zone (b) and a diffusive zone (g). In the mixing zone, convective mixing renders chemical transport nearly instantaneous, whereas in the diffusive zone chemical transport is diffusion limited. This combination of a constant supply of OE through a transport channel and diffusive transport at the precipitation front ensures spatiotemporally uniform and fast patterning of layered materials. In particular, the reaction front then moves ballistically (i.e. with constant speed) and not diffusively (i.e. slowing down). Hence, this strategy overcomes the inherent diffusive limitations of RD processes, whilst retaining their desired simplicity, to yield highly uniform multilayered materials with precise tunability.

2.2 Results and Discussion

To probe the mechanism where chemically induced gel contraction causes the formation of a channel, which in turn transports reactants ballistically to the front of the channel, we develop a system where transport rates and channel formation can easily be visualized. Specifically, we follow the transport rate of the dye fluorescein in a mechanically responsive gel. We cast a gelatin-alginate interpenetrating network (GA-IPN) in a cylindrical tube and place a solution (10 mL) of fluorescein (1.5 mM) and the mechanical actuator calcium nitrate (2.4 M) on top; calcium ions shrink the gel by crosslinking alginate (Figure 2.2A)[57]. Consistent with our proposed scenario, in MRGs a clearly visible channel (gap between gel and tube) opens, directly connecting the OE reservoir with the reaction zone (Figure 2.2B). In contrast to the diffusive transport observed in SGs, in MRGs we observe that the rate of transport is constant over time, indicative of ballistic transport (Figure 2.2C). Moreover, in a SG chemical transport over 4 cm takes over 99.4 hours, whereas in MGS this same distance is reached more than 10 times faster in merely 8.4 hours, showing that MRGs allow for rapid transport over long distances.

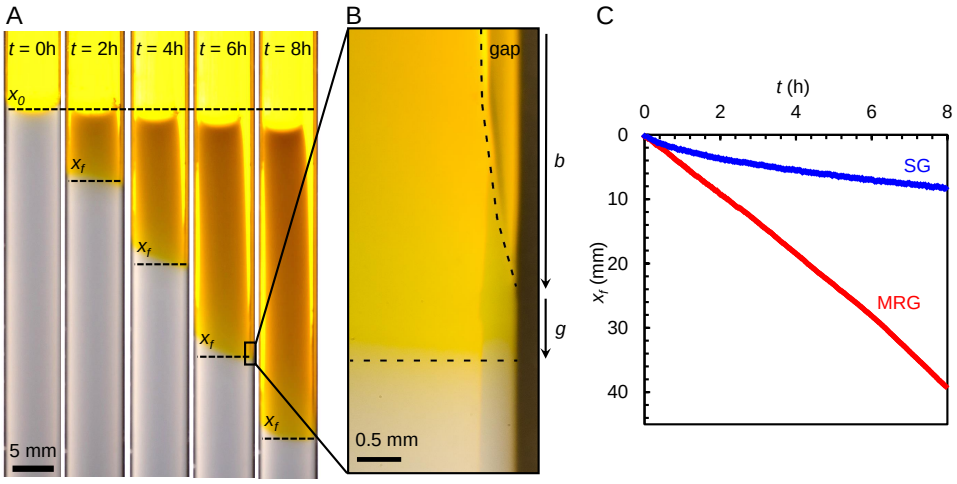

FIGURE 2.2: (A) Time-lapse series showing transport of fluorescein in an MRG. (B) Close up photograph of MRG showing the formation of a channel that enables ballistic transport towards the front. (C) x_f-t plot showing slow diffusive transport in SG (blue line) and rapid ballistic transport in MRG (red line).

To explicitly show that channel formation induces flow through the channel, from the dye reservoir towards the transport front, we monitor the experiment with Schlieren microscopy. This optical technique visualizes flow by revealing differences in refractive index and thus differences in density. Using this technique, we observe convective flow only in the presence of the gap (see supporting Movie C2-S1). Additionally, closer inspection of the transport front shows that gap formation is preceded by a diffusive zone with a constant length (g) (Figure 2.2B). Channel formation in MRGs thus induces ballistic transport towards a diffusion zone of constant width.

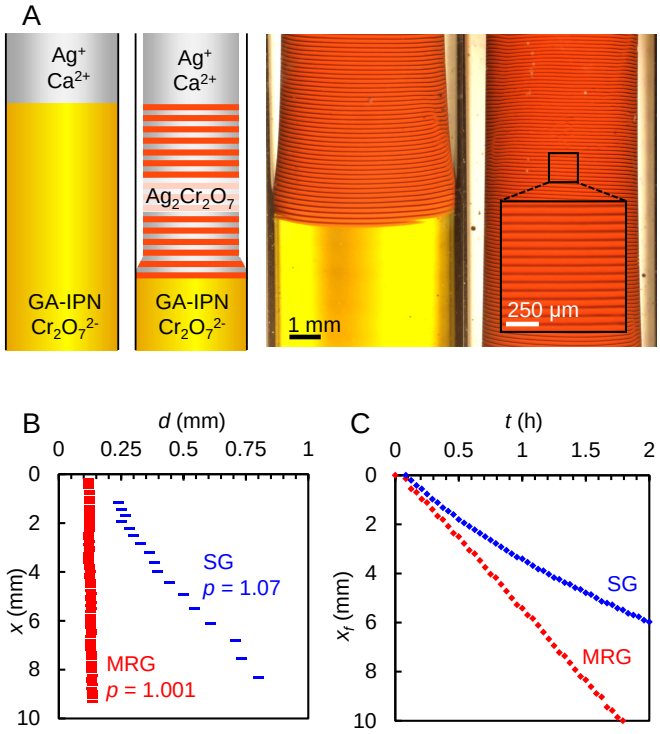

FIGURE 2.3: Periodic precipitation in MRG. (A) Equidistant pattern formation of $Ag_2Cr_2O_7$ in an GA-IPN. (B) The band distance increases for SG ($p = 1.07 \pm 0.03$) and remains constant for MRG ($d = 120$ µm, $p = 1.001 \pm 0.002$). (C) x-t plot shows diffusive precipitation in SG (blue line) and rapid ballistic transport in MRG (red line). Note that the curved appearance of the banding pattern is an optical effect caused by the cylindrical shape of the gel and its container. Cross sectioning of a gel reveals a flat, non-curved pattern (Figure S2.3)

The constant transport rate in MRGs suggests that new types of pattern formation may be achieved by coupling traditional reaction-diffusion processes with mechanically responsive gels. To exploit this potential, we embed Liesegang periodic precipitation in an MRG. We allow a combination of OE (0.8M $AgNO_3$) and a mechanical actuator (2.4M $Ca(NO_3)_2$) to diffuse into an GA-IPN containing the IE (17mM $K_2Cr_2O_7$) which react form a precipitation pattern of $Ag_2Cr_2O_7$ (Figure 2.3A, see supporting Movie C2-S2 for a time-lapse of this pattern forming and supporting figure S2.1 for a larger-scale image). We note that in this example we use a large volume of outer electrolyte (20 mL) compared to the total gel volume (1.5 mL). This is because we want to limit the effect of concentration losses in the outer electrolyte due to dilution and consumption by precipitation. We have investigated the effects of such concentration losses on patterning behavior and found that for sufficiently large yet realistic volumes of outer electrolyte these effects are negligible (See Figure S2.2). Indeed, for the experiment performed here, the patterns appear equidistant under visual inspection (Figure 2.3A, B).

To quantify the equidistant nature of the pattern, we follow the standard approach where we define the spacing fraction as the fraction of subsequent band locations, $p_n := \frac{x_{n+1}}{x_n}$, and then determine $p := \lim_{n\to\infty} p_n$. In SGs, $p > 1$ is observed, which corresponds to a banding pattern where the distance between subsequent bands (d) increases over time. In contrast, in MRGs we observe highly regular equidistantly spaced periodic precipitation with a constant band distance ($d = 126\ \mu m \pm 4.6 \mu m$) (Figure 2.3B) and uniform band width ($w = 67\ \mu m \pm 4.6 \mu m$). For large n, p_n tends to converge to its asymptotic value as $1/n$; hence, a very accurate determination for p, as well as its error bar, is obtained by plotting p_n as function or $1/n$ and extrapolating the data to $n \to \infty$ (see the supplementary information for a detailed explanation on determining the band spacing, the band width and estimating p, Figures S2.1 and S2.3). For our MRG, we find that $p = 1.001 \pm 0.002$; hence for large n and x, our pattern is equidistant within our error bar, confirming the visual observation of constant band spacing (Figure 2.3B and Figure S2.4). Simultaneously, a clearly visible channel is formed, which closely follows the precipitation front which propagates at a constant and high rate (5 mm/h, Figure 2.3C). Hence, MRGs allow periodic precipitation reactions to rapidly form asymptotically equidistant patterns.

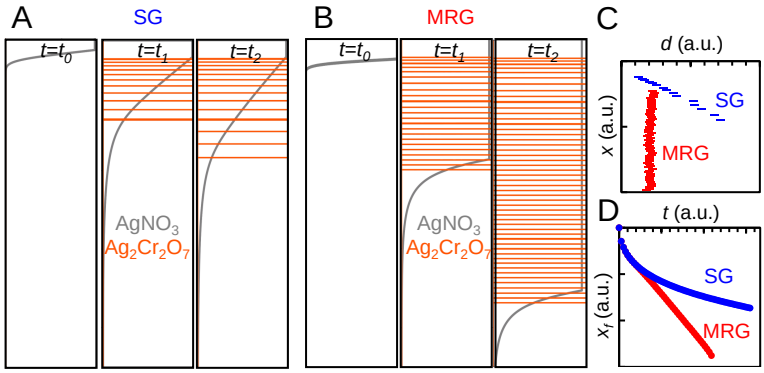

FIGURE 2.4: Numerical modeling accurately reproduces uniform pattern formation in MRGs. (A) Modeling of periodic precipitation shows Liesegang patterns in SG and (B) uniform patterning in MRG. (C) Modeling reproduces different p values found in SGs and MRGs. (D) Modeling confirms diffusive transport observed in SGs and ballistic transport observed in MRGs.

To further verify our channel formation - ballistic transport scenario, and to quantitatively understand the role of the additional parameters introduced, we develop a numerical model. Inspired by previous RD models, we compute the reaction of the inner and outer electrolyte using first- and second-order reaction kinetics (see chapter 5). To describe MRGs, we model the mechanical response via first-order reactivity between calcium and alginate and assume that a transport channel opens once this reaction exceeds a specified threshold, allowing ballistic transport of the outer electrolyte (Figure 2.4). As expected, modeling of periodic precipitation in SGs shows diffusive transport and subsequently non-equidistant Liesegang patterns (Figure 2.4A, C, D), whereas modeling of periodic precipitation in MRGs shows ballistic transport and equidistant patterning (Figure 2.4B, C, D).

Our model allows efficient screening of the increased parameter space of RD processes in MRGs and directly assess its effect on patterning behavior. Crucially, our model shows that increasing the calcium concentration speeds up the front rate v (Figure 2.5A) and lowers the band distance d (Figure 2.5B). We propose that this is caused by the following mechanism: at higher calcium concentrations the shrinkage rate increases and leads to a shorter diffusive zone (Figure 2.5C), which at the precipitation front causes a higher outer electrolyte concentration, in turn resulting in shorter band distances.

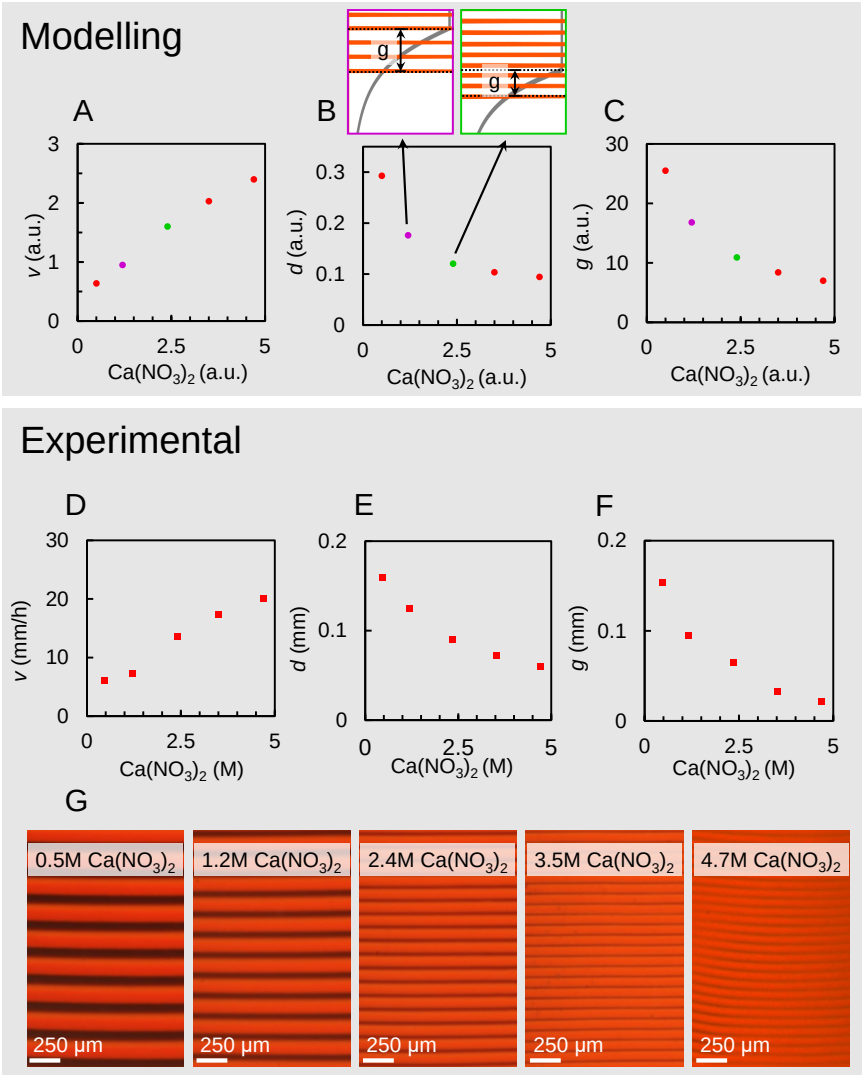

FIGURE 2.5: Model-guided tunability of periodic precipitation in MRG. (A) Modeled relation between the $Ca(NO_3)_2$ concentration and transport rate (v). (B) Model predicts that the band distance decreases for increasing $Ca(NO_3)_2$ concentrations. (C) Model predicts a decreased diffusive zone (g) for higher $Ca(NO_3)_2$ concentrations (D, E, F) Experimental relation between $Ca(NO_3)_2$ concentration and (D) transport rate (v), (E) band distance (d), (F) diffusive zone length (g). (G) Experimental tuning of the precipitation pattern by modulation of the $Ca(NO_3)_2$ concentration.

Guided by the modeling insights, we explore how the band distance in MRGs can be controlled by modulating the calcium ion concentration in the reservoir solution. Consistent with modeling, we observe that higher calcium concentrations indeed result in shorter diffusive zone lengths (Figure 2.5D) and subsequently shorter band distances (Figure 2.5E) as well as increased transport rates (Figure 2.5F). We find that varying the concentration of calcium between 0.47 M and 4.7 M enables tuning of the band distance between $d = 160$ µm and $d = 60$ µm, respectively (Figure 2.5G). Hence, coupling of MRGs with periodic precipitation reactions enables equidistant patterns with unique mechanical-mediated tunability.

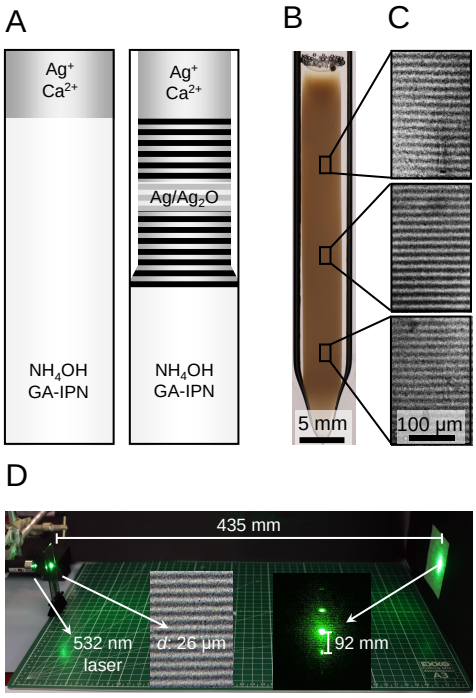

FIGURE 2.6: Generality, scalability and functionality potential of mechanically-coupled periodic precipitation. (A) Schematic representation of the experimental setup used (B) Macroscopic image of a GA-IPN MRG containing a microscopic pattern of silver nanoparticles. (C) A cross-section of the MRG reveals the equidistant microscopic banding pattern ($d = 17$ µm) (D) Irradiation of a different microscopic pattern ($d = 26$ µm) with a green laser (532 nm) yields diffraction patterns.

Our strategy of enhancing periodic pattern formation processes via ballistic transport in MRGs can readily be extended to other pattern formation processes employing responsive gels. This versatility and tunability opens exciting opportunities for fabricating functional self-organized periodic composites. We explore this potential by embedding a reaction-diffusion system that yields patterned silver nanocrystals into our MRGs to form a self-organized optical diffraction grating (Figure 2.6A)[32].

To this aim, we infiltrate a gelatin-alginate MRG containing NH_4OH (5.9 μM) with a solution of $AgNO_3$ (0.8 M) and $Ca(NO_3)_2$ (0.5M - 2.4M, Figure 2.6B), inducing tunable precipitation of equidistant, narrowly spaced bands ($d = 15 - 30$ μm) of silver nanoparticles ($150 - 200$ nm diameter) (Figure 2.6C). Irradiating the periodic composite with a green laser ($\lambda = 532$ nm) shows a diffraction pattern that is in good agreement with the band spacing of the silver nanoparticles ($d = \frac{m\lambda}{2sin(\theta)}$, calculated: $d = 25.2$ μm, observed: $d = 25.8$ μm), Figure 2.6D), illustrating potential for self-organized functional materials.

2.3 Conclusion

In summary, we introduce here a versatile strategy to overcome diffusive limitations of the Liesegang process by exploiting mechanically responsive hydrogels. We show that the self-regulated formation of a transport channel ballistically carries reactants towards a reaction-diffusion zone, where diffusion controlled pattern formation occurs. This combination of long-range ballistic transport and short-range diffusive control allows rapid formation of uniform patterns. Furthermore, we demonstrate straightforward pattern tunability and show that our strategy can readily be applied to other reaction-diffusion systems. Although our method is limited by the compatibility of the mechanically responsive materials, their actuators and the reaction-diffusion systems, we believe that as more and more responsive materials are developed for applications such as drug delivery and sensing, exciting new opportunities will arise[57]. Collectively, by circumventing the inherent limitations of diffusion, our strategy unlocks the full potential of reaction-diffusion processes for the manufacturing of high-performance, uniformly layered materials.

As chemical transport plays essential roles in artificial and natural processes, we envisage that using mechanically active materials to bypass diffusion limitations will enhance our understanding of, and control over, chemical transport in complex artificial and living matter[58]. Additionally, we foresee that embedding reaction-diffusion processes in mechanically responsive meta-materials offers a general strategy to realize complex self-organized materials that are otherwise difficult to make[59]. Finally, we envisage that embedding reaction-diffusion processes in mechanically responsive meta-materials will lead to exciting opportunities for the generation of complex patterns with advanced functionalities.

2.4 Materials and Methods

All chemicals were used without additional purification. Gelatin was purchased from Sigma-Aldrich and was type A from porcine skin, roughly 300g Bloom. Sodium alginate was purchased from PanReac AppliChem and was of medium viscosity (350 - 550 mPas at 1%), with a molecular weight of 10000 - 600000 g/mol.

2.4.1 Rate Analysis

In order to analyze precipitation rates, time-lapses were made of all samples. To prevent imaging complications caused by the curvature of the used glass cylinders, all samples were placed in a custom-built glass container with immersion oil. These time-lapses were analyzed using a Python3 script, which follows the position of the precipitation front over time.

2.4.2 Fluorescein Dye Experiments

In a typical experiment 50 g of gel stock was prepared by dissolving gelatin (2.5 g, 5w%) in hot water (47.5 mL, 65 °C). Aliquots (roughly 1.2 mL) of this hot solution were then transferred to cylindrical glass tubes (60x0.6 mm) and allowed to cool down to RT, by which the gels had solidified. The mechanically responsive counterparts were produced by simply dissolving sodium alginate (0.25 g, 0.5w%) in water prior to the addition of gelatin.

The experiment was started by mounting a syringe (10 mL) without stopper onto these glass tubes, which was subsequently filled with 10 mL of either just fluorescein (1.5 mM) for SGs, or a combination of fluorescein (1.5 mM) and $Ca(NO_3)_2$ (2.4 M) for MRGs.

2.4.3 Potassium Dichromate Gel Preparation

In a typical experiment 50 g of gel stock was prepared by dissolving gelatin (2.5 g, 5w%) in hot water (47.5 mL, 65 °C) and adding $K_2Cr_2O_7$ (250 mg). Aliquots (roughly 1.5 mL) of this hot solution were then transferred to cylindrical glass tubes (60x0.6 mm) and allowed to cool down to RT, by which the gels had solidified. The mechanically responsive counterparts were produced by simply dissolving sodium alginate (0.25 g, 0.5w%) in water prior to the addition of gelatin.

Precipitation was induced by mounting a syringe without stopper onto these glass tubes, which was subsequently filled with 20 mL of either $AgNO_3$ (0.2 - 0.8M) for SGs, or a combination of $AgNO_3$ (0.2 - 0.8M) and $Ca(NO_3)_2$ (0.5 - 4.9M) for MRGs.

2.4.4 Ammonia Gel Preparation

In a typical experiment 50 g of gel stock was prepared by dissolving gelatin (2.5 g, 5w%) in hot water (47.5 mL, 65 °C) and adding NH_4OH (25%, 22 μL). Aliquots (roughly 1.5 mL) of this hot solution were then transferred to cylindrical glass tubes (60x0.6 mm) and allowed to cool down to RT, by which the gels had solidified. The mechanically responsive counterparts were produced by simply dissolving sodium alginate (0.25 g, 0.5w%) in water prior to the addition of gelatin. Precipitation was induced by mounting a syringe without stopper onto these glass tubes, which was subsequently filled with 20 mL of either $AgNO_3$ (0.2 - 0.8M) for SGs or a combination of $AgNO_3$ (0.2 - 0.8M) and $Ca(NO_3)_2$ (0.5 - 4.9M) for MRGs. After precipitation in the entire gel column was complete, gels were cut into thin slices. These slices were analyzed under a Leica DMRX microscope (Figure S2.5).

2.4.5 Schlieren Imaging

Schlieren imaging highlights differences in density and is used to visualize flow. High turbulence indicates convective flow, whereas static areas indicate diffusion limited regions. Since the curved surface of the typically used containers prevented effective Schlieren microscopy, different samples were prepared. Instead of cylindrical glass tubes, an MRG was now cast in-between two glass microscopy slides separated by a rubber spacer (1 mm), which allowed us to observe a flat surface. The aforementioned transport channel now forms in-between these glass slides and the hydrogel surface. The result of this measurements can be seen in Movie C2-S1.

2.5 Supporting Information

2.5.1 Large scale patterning analysis of periodic precipitation in SGs and MRGs

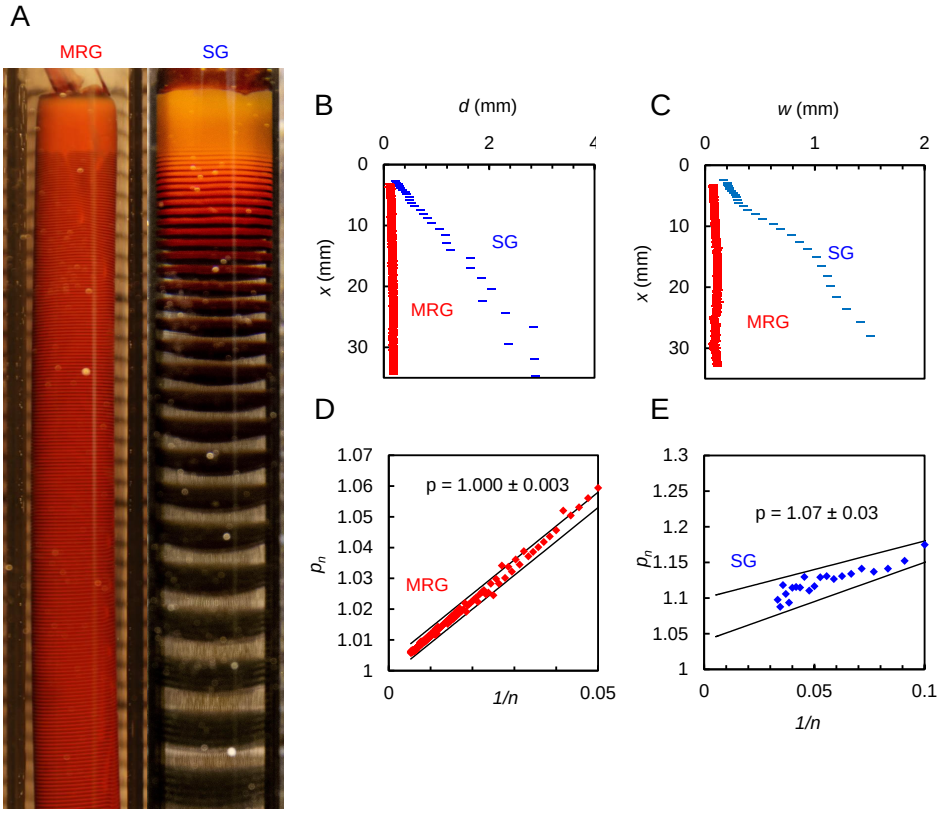

SUPPLEMENTARY FIGURE S2.1: Determining the scaling factor in mechanically responsive gels (MRGs) and static gels (SGs). (A) Large scale patterning in an MRG and an SG. (B) Band distance d versus the location x. (C) Band width w versus the location x. (D) p-value determination of the pattern produced in the MRG, indicating equidistant patterning. (E) p-value determination of the pattern produced in the SG, indicating classical Liesegang patterning.

2.5.2 Influence of volume ratios on patterning behavior

Over the course of an experiment, there are two processes that reduce the concentration of the outer electrolyte. Firstly, the outer electrolyte is consumed by the reaction with the inner electrolyte. Secondly, the outer electrolyte is diluted by transport from the reservoir into the gel, because the total volume which contains the outer electrolyte increases, lowering its concentration. We study the effect of these two processes on the spacing of the pattern, by preparing patterns with varying outer electrolyte to inner electrolyte (OE:IE) ratios (Figure S2). For small OE:IE ratios the decrease in concentration will be large, whereas for large OE:IE ratios the decrease in concentration will be small.

First, with our numerical model we screen a range of outer to inner electrolyte volume ratios (Figure S2.2A). We find that as the relative volume of outer electrolyte increases, the band distance d becomes constant over a large range of x and subsequently the scaling factor p approaches 1 (Figure S2.2 B, C). Repeating these simulations for a range of volume ratios, we find that $p-1$ scales as $\frac{1}{V_{ratio}} = \frac{V_{gel}}{V_{outer}}$ (Figure S2.2 C).

Second, we perform a new series of experiments where we compare experimental patterns for MRG and SG and the effect of increasing the volume of outer electrolyte. We produce patterns of silver dichromate with varying volumes of outer electrolyte and include a pattern produced in an SG (Figure S2.2 D), to show that even with large volumes pattern formation in SGs produces typical non-uniform Liesegang type patterns. This experiment shows that even with low volumes of outer electrolyte, relatively uniform patterns can be obtained with $p-1 = 0.0073$ (Figure S2.2 E). Simultaneously these results show that with a large enough reservoir of outer electrolyte, dilution and consumption effects can be negated to produce equidistant banding patterns at larger spatial scales $p-1 = 0.0017$ (Figure S2.2 F).

Together, these simulations and experiments clarify the importance of large volume ratios for equidistant pattern formation, and show that, for each target precision in p, one can choose an appropriately large volume of the outer electrolyte. Moreover, these experiments show that for practical length and time scales, it is possible to produce highly uniform, asymptotically equidistant, patterns by using large yet realistic outer electrolyte volumes.

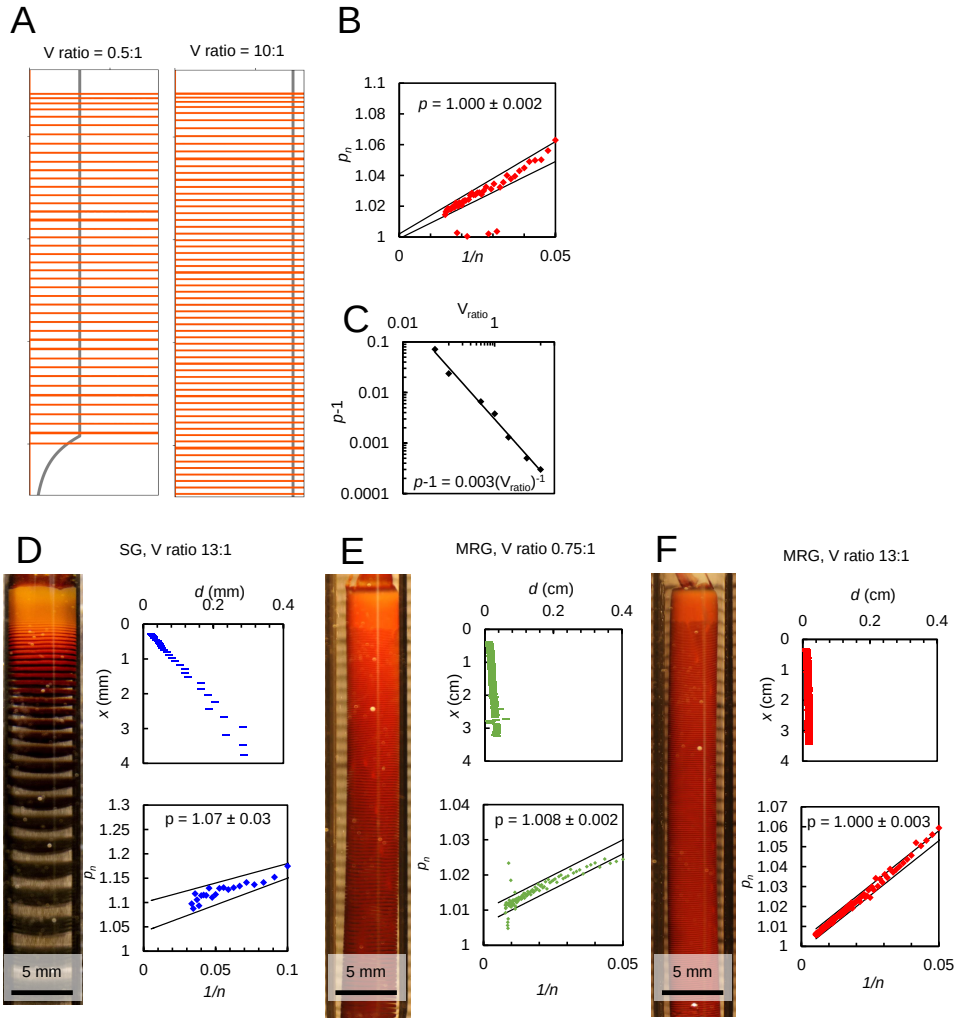

SUPPLEMENTARY FIGURE S2.2: Pattern formation with varying outer electrolyte volumes (V_{outer}) to gel volume (V_{gel}) ratios (V_{ratio}). (A) Numerical model results for two volume ratios, with the pattern depicted in orange and the outer electrolyte concentration in gray. (B) p-value determination for $V_{ratio} = 10$ by plotting p vs n^{-1} (See Figure S2.4 for a detailed explanation on the determination of p). (C) Modeled volume ratios versus $p - 1$ showing that for higher volume ratios p approaches unity, indicative of equidistant pattern formation. (D) Silver dichromate pattern in an SG with a OE:IE ratio of 13:1, showing Liesegang type patterning. (E) Silver dichromate pattern in an MRG with a OE:IE ratio of 0.75:1, showing weakly non-equidistant patterning. (F) Silver dichromate pattern in an MRG with a OE:IE ratio of 13:1, showing equidistant patterning.

2.5.3 Cross sectioned gel reveals flat, non-curved pattern

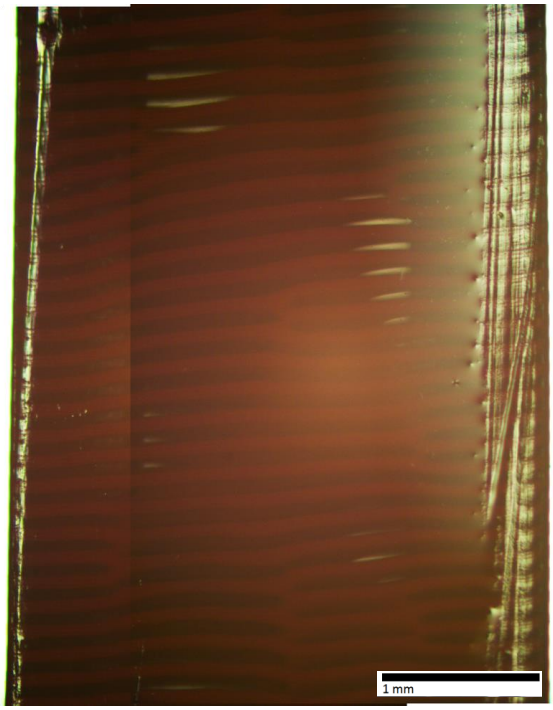

SUPPLEMENTARY FIGURE S2.3: Cross-section of a patterned gel shows non-curved patterning over the entire diameter. Note that the gel is slightly wider than the microscope field of view, such that the figure is a composite of two pictures to show the entire diameter of the gel.

2.5.4 Band spacing, band width and p value determination

In all cases, we use a Python3 script to convert and an image of the pattern (Figure S2.4A) into a cropped grayscale image (Figure S2.4B). Subsequently, the intensity of that image is summed over the horizontal axis to yield an intensity profile (Figure S2.4C). Using the *Scipy signal* package *find peaks* we find the peaks in this intensity profile, which correspond to the location of the bands in the pattern. These peak locations give the locations x_n, from which the locations x_{n+1} are derived. For every nth band p is then calculated with $p_n = x_(n+1)/x_n$. We then plot p_n over n^{-1} (Figure S2.4D) and estimate p for $lim(n \to \infty)$ (Figure S2.4D). Band widths were determined by thresholding an image of the pattern using the *opencv* package *adaptiveThreshold*, followed by the *scipy* packages *find peaks* and subsequently *peak widths* to determine band locations and band widths.

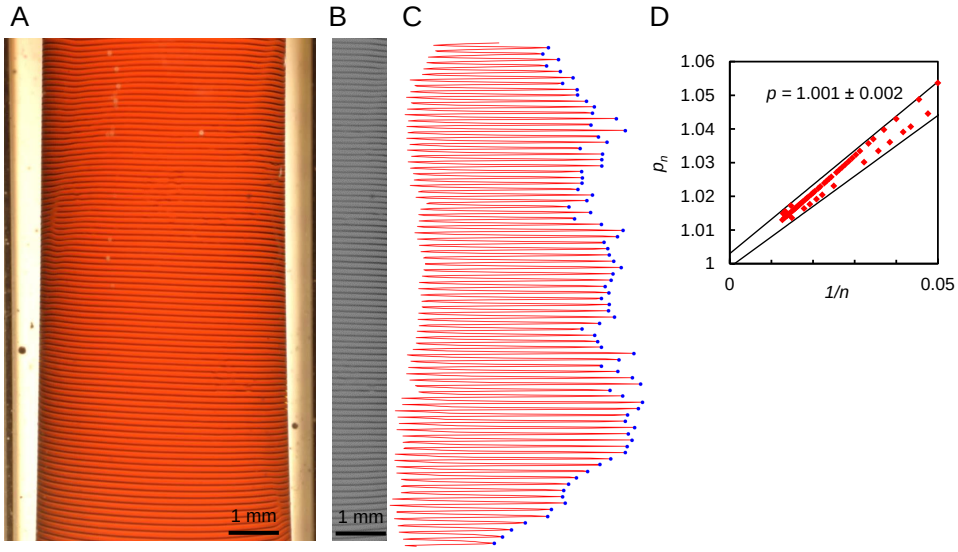

SUPPLEMENTARY FIGURE S2.4: Method used to determine p values. (A) Photograph of a silver dichromate pattern in an GA-MRG. (B) Cropped grayscale image used to determine the intensity profile (C) Corresponding intensity profile, obtained by summing over the horizontal axis, of which the peaks correspond to bands in the pattern (highlighted in blue). (D) p-value estimation by plotting p over n^{-1} and estimating p for $\lim n \to \infty$.

2.5.5 Microscopic banding pattern analysis

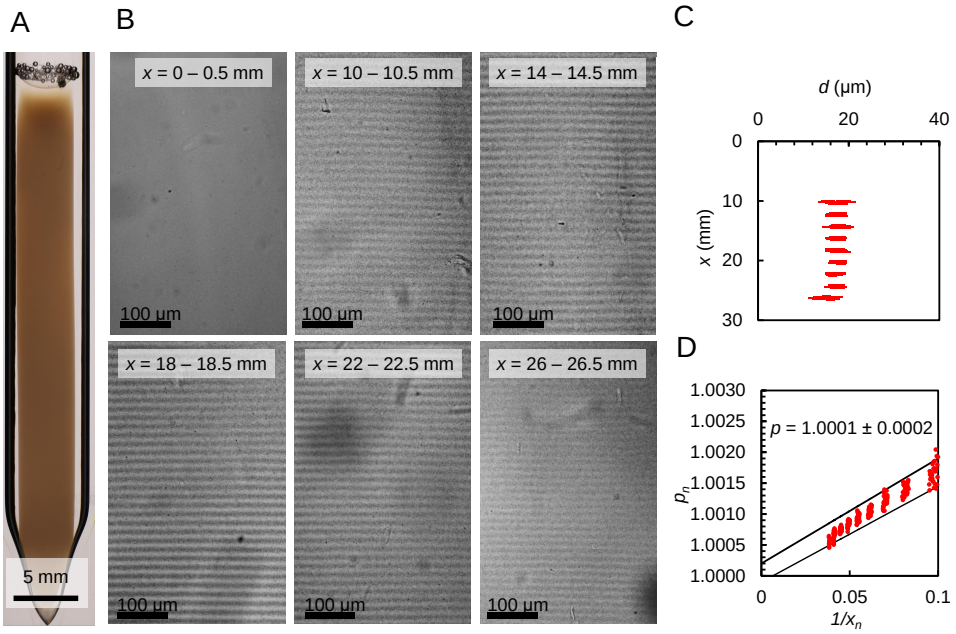

SUPPLEMENTARY FIGURE S2.5: Microscopic banding pattern of silver nanoparticles. (A) MRG containing a pattern of silver nanoparticles. (B) Microscopy images of a longitudinal cross-section, revealing the microscopic pattern. Note that near the interface no banding is observed; only after 10 mm from the initial gel interface patterning begins. (C) Analyzing 2 mm intervals of the microscopic pattern shows highly uniform, equidistant patterning. Near the bottom of the system, spacing is seen to slightly decrease, which is likely due to boundary effects. (D) p-value determination, note that in our fit, we excluded the data from $x = 26 - 26.5$ mm.

2.5.6 Movies

All movies are publicly available via: `https://github.com/cvcampenhout/Scripts-and-Movies-Thesis`.

C2-S1 Schlieren imaging of chemical transport in MRG comp.mp4

In this movie a timelapse is shown, where 1 second of video time corresponds to 720 seconds real-time. This movie was recorded using a Schlieren setup, which highlights differences in density and visualizes flow. In view is a sample holder which consists of two glass slides spaced with a rubber spacer. Between the slides we have casted a GA-MRG. At the start of this movie an outer electrolyte containing both calcium and silver ions is placed on top of this gel. In the outer electrolyte reservoir a lot of convective flow is occurring and as the precipitation front moves through the gel this region increases in size. During the freeze-frame the precipitation front has moved roughly halfway through the gel and a clear contrast between a convective region and the unreacted gel is visible. The top two-thirds of the gel shows chaotic movement, whereas the bottom third is completely static.

C2-S2 Periodic Precipitation in MRG.mp4

In this movie a timelapse is shown, where 1 second of video time corresponds to 720 seconds real-time. Out of view, on top of the hydrogel, is a large outer electrolyte reservoir containing both calcium and silver ions. As these diffuse into the gel, orange bands of silver dichromate precipitate. At the same time, gel contraction, which closely follows the precipitation front, is observed on both the left and right sides of the tube. About halfway through the video the field of view is adjusted to move the precipitation front back into view.

2

3 Patterning Complex Line Motifs in Thin-Films Using Immersion-Controlled Reaction-Diffusion

The discovery of self-organization principles that enable scalable routes towards complex functional materials has proven to be a persistent challenge. Here reaction-diffusion driven, immersion controlled patterning (R-DIP) is introduced, a self-organization strategy using immersion controlled reaction-diffusion for targeted line patterning in thin films. By modulating immersion speeds, the movement of a reaction-diffusion front over gel films is controlled, which induces precipitation of highly uniform lines at the reaction front. A balance between the immersion speed and diffusion provides both hands-on tunability of the line spacing ($d = 10 - 300$ μm) as well as error-correction against defects. This immersion-driven patterning strategy is widely applicable, which is demonstrated by producing line patterns of silver/silver oxide nanoparticles, silver chromate, silver dichromate, and lead carbonate. Through combinatorial stacking of different line patterns, hybrid materials with multi-dimensional patterns such as square-, diamond-, rectangle- and triangle-shaped motifs are fabricated. The functionality potential and scalability is demonstrated by producing both wafer-scale diffraction gratings with user-defined features as well as an opto-mechanical sensor based on Moiré patterning.

The work described in this chapter is published in:
C. T. van Campenhout, H. Schoenmaker, M. van Hecke, and W. L, Noorduin. *Adv. Mater.*, **2023,** 5(39): 2305191.

3.1 Introduction

Nature's extraordinary diversity of complex patterns holds fascination to lay people and scientists alike, and provides an endless source of inspiration for developing new materials with advanced functionalities[1,3,60–66]. Specifically, thins films with complex motifs are of great interest as these can be integral to the next generation of optical, electronic, and mechanical devices[6,7,67]. However, manufacturing of such motifs has remained challenging, with costly lithography techniques being the leading method to produce nanoscale complexity[8,68–70]. From this perspective, bio inspired self-organization can be an attractive starting point, as the inherent autonomous nature of such processes holds the potential to offer simple and scalable production of uniform complex patterns with user-defined control and automatic error correction for tolerance against defects[71–74]. Already, many self-organization strategies have been developed, such as evaporative assembly and dip-pen nanolithography[75–80], but whilst such processes are able to produce highly uniform patterns, delicate and extremely precise setups are often required and scalability can be difficult or practically impossible.

Alternatively, self-organization of patterns is possible via reaction-diffusion processes, in which the interplay between reaction kinetics and diffusion can induce complex patterns spontaneously[22,50,56]. Since these processes rely on chemical feedback loops, there is the potential to achieve inherent error-correction towards robustness for large scale production of uniform patterns[65]. Moreover, reaction-diffusion processes such as Liesegang pattern formation induce rhythmic precipitation of line or band patterns of many different chemical compositions, and combinations with top-down fabrication techniques such as wet-stamping can yield more complex patterns[29,33,81–84]. Unfortunately, because of the diffusive nature of these processes, lines or bands form at increasing spacing, resulting in non-uniform patterning over larger scales, hence limiting scalability[30]. To overcome such drawbacks, we recently have shown highly uniform banding patterns in bulk gels by employing a mechano-chemical feedback loop that transports reagents non-diffusively through opening channels[85]. However, because mechanical opening of a transport channel is integral to the approach, this strategy only works for three-dimensional materials, highlighting that entirely new principles need to be developed to achieve uniform large-scale patterning of complex motifs in thin films.

Here we introduce reaction-diffusion driven immersion-controlled patterning (R-DIP), a method for creating complex line motifs in thin films on wafer scale with user-defined tunability (Figure 3.1A). First, R-DIP is used to pattern uniform lines with user-defined spacing in thin gel films. Second, multiple thin films with different line patterns and chemical compositions are superimposed in combinatorial stacks to realize complex composites and hybrid motifs. Using this strategy, we demonstrate that a large diversity of complex, yet well-defined motifs such as squares, diamonds, rectangles and triangles can be realized, and exploit this control to develop tunable diffraction gratings and opto-mechanical sensors.

The key idea behind R-DIP is that a thin gel film, in which one reagent (the gel reagent) is dissolved, is steadily immersed into a solution of a second reagent (the immersion reagent), which react upon contact at the reaction front to induce rhythmic precipitation of an insoluble reaction product (Figure 3.1B). This reaction product forms highly uniform equidistant line patterns because of a balance between the immersion speed (v) and upwards diffusion of the immersion reagent into the gel film. Consequently, a constant concentration gradient of immersion reagent is maintained at the reaction front, which induces uniform pattern formation. Additionally, because the process relies on chemical feedback loops, it possesses inherent error-correction, enabling large scale production of user-defined line motifs.

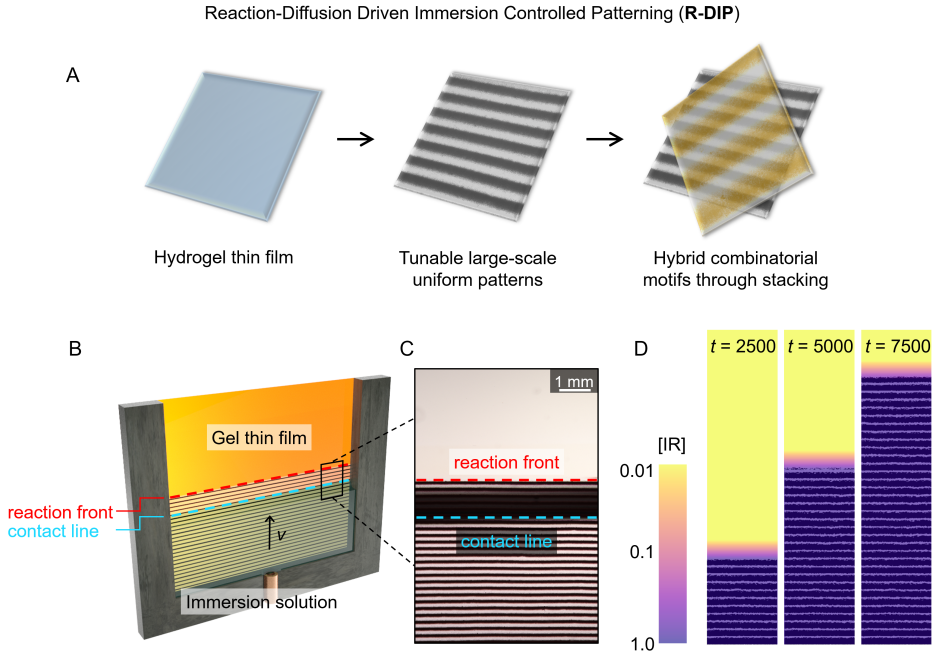

FIGURE 3.1: (A) Overview of the R-DIP process: first a hydrogel thin film is cast, in which an immersion controlled reaction-diffusion process generates large-scale uniform stripe patterns. Multiple of these user-defined patterns can be stacked to produce a large diversity of higher-order composites and hybrid motifs. (B) Concept image depicting the experimental setup: a gel film containing gel reagent is placed in an empty container, into which immersion reagent (IR) is pumped with a syringe pump, steadily immersing the thin film. Preceding the liquid-gel contact line (depicted in blue) at the reaction front (depicted in red) the reaction between the immersion and gel reagent produces a line pattern of precipitate perpendicular to the immersion direction. At constant immersion speed a balance between the immersion speed v and upward diffusion is reached, resulting in highly uniform line distances (d). (C) A close-up during the patterning process reveals the formation of a highly uniform line pattern of silver dichromate precipitate at the reaction front (see Movie C3-S1). (D) Numerical modeling accurately reproduces the experimental pattern and provides mechanistic insights. During the process, the concentration gradient of silver ions at the liquid-gel interface remains constant and therefore patterning is uniform (see chapter 5 for details on the numerical model).

3.2 Results and Discussion

Figure 3.1B shows the general method of inducing pattern formation with immersion-controlled reaction-diffusion. We demonstrate the proof of principle for the well-studied periodic precipitation of silver dichromate ($Ag_2Cr_2O_7$) using silver nitrate as immersion reagent and potassium dichromate as gel reagent following: $2Ag^+(aq) + Cr_2O_7{}^{2-}(aq) \rightarrow Ag_2Cr_2O_7(s)$[86].

Typically, we cast thin hydrogel films consisting of gelatin (10 wt%), agarose (0.5 wt%), potassium dichromate ($K_2Cr_2O_7$, 0.2 wt%), acetic acid (0.9 %v/v) and the surfactant 3-[hydroxy(polyethyleneoxy) propyl] heptamethyltrisiloxane (HPEO-HMTS, 0.15 %v/v) onto glass slides (75x50 mm, see the Materials and Methods for details). These components have the following functions: gelatin promotes pattern formation[87]; agarose offers additional mechanical gel stability; potassium dichromate acts as the gel reagent; acetic acid ensures that the dichromate-chromate equilibrium is shifted towards the desired dichromate anion[88]; and the surfactant prevents pinning of the immersion solution on the gel surface. Note that gel films are thin (<0.6 mm) to ensure that patterning is consistent throughout the depth of the film. To start the process, the gel film is mounted vertically in an empty container. Then, patterning is induced by filling the container at user-defined speeds with the immersion reagent silver nitrate ($AgNO_3$, 0.4 M in water). The filling results in a moving liquid-gel contact line with speed v and in precipitation of separate $Ag_2Cr_2O_7$ particles that arrange in lines perpendicular to the immersion direction. We monitor this pattern formation over long distances by tracking the moving contact line with a custom motorized horizontal microscope (see Figure S3.1 for details). We observe the formation of a line pattern with highly uniform spacing ($d = 200 \pm 6$ μm) throughout the entirety of the thin film (Figure 3.1C, Movie C3-S1).

To explain this uniform pattern formation, we numerically model the 2D reaction-diffusion process. In this model, we replicate gel immersion by calculating the location of the contact line at every time-step and setting the concentration of immersion reagent equal to the starting concentration up to this location. All reactants diffuse following a forward-in-time-central-in-space scheme, and the reaction of the gel and immersion reagent is computed using first- and second-order reaction kinetics (see chapter 5 for further details). This model accurately reproduces the observed uniformity and immersion speed dependent line spacing. Monitoring concentration gradients in the model reveals the formation of a steady-state which balances the upwards diffusion of immersion reagent into the gel and the immersion speed v (Figure 3.1D). Because of this steady-state, the concentration gradient of immersion reagent at the reaction front remains constant, thereby inducing uniform pattern formation.

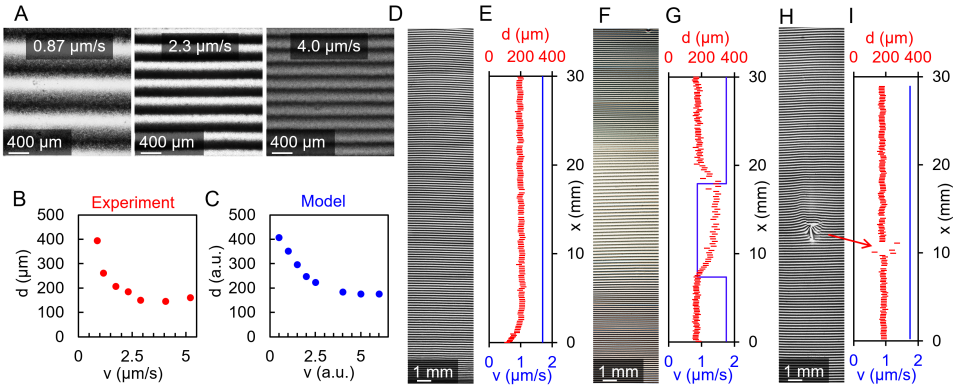

FIGURE 3.2: Patterning tunability (A) Experimentally obtained patterns for a range of immersion speeds v (B, C) Plotting the line distance d versus the immersion speed v for both the model and the experiments shows a trend of decreasing d for increasing v. (D, E) Large scale pattern obtained at constant v with highly uniform line spacing ($d = 200 \pm 6$ µm). (F, G) Dynamic tunability in a silver dichromate pattern by changing v during pattern formation showing that modulating v directly translates to a change in line distance d. (H, I) Patterning is self-correcting and recovers to the original line pattern swiftly after encountering a defect in the thin film. Note that the figures D, F, and H are stacks composed of multiple images.

The intricate interplay between diffusion of silver ions and immersion speed suggests that by modulating v we can tune the line distance d. Indeed, we find that increasing v results in decreasing line widths (Figure 3.2A), both in experiments (Figure 3.2B) and in our model (Figure 3.2C). This allows us to precisely tune the line pattern by controlling the immersion speed. At constant v, patterning is uniform over long distances (Figure 3.2D, E). Because pattern formation is directly dependent on the user-defined speed of the contact line, we can dynamically tune patterning within a thin film (Figure 3.2F, G). We demonstrate this dynamic tunability by modulating v from fast to slow ($v = 1.75 \rightarrow 0.87$ µm/s), which increases the line distance ($d = 172 \rightarrow 290$ µm). After going back to the initial immersion speed ($v = 1.75$ µm/s), the patterning restores to the initial spacing ($d = 172$ µm). Thus, v is directly tied to a specific line distance d and can be tuned during the process, enabling rational and precise steering of the self-organization process.

The uniformity of the pattern formation across large distances suggests that R-DIP has an inherent error-correction mechanism. To study this error-correction mechanism, we deliberately puncture the gel film and subsequently follow how pattern formation is influenced by this defect (Figure 3.2H, I). As soon as the reaction front reaches the defect, the reaction front and pattern become disturbed. However, already after fewer than 10 lines the reaction front is smoothened out by diffusion and subsequently deposited lines are straight again, demonstrating that R-DIP indeed offers error-correction for sustaining uniform micro-scale ordering over decimeter distances. The steady-state conditions at the reaction front thus offer both swift responsiveness to changes in the immersion speed and error-correction for defect tolerance.

Because R-DIP produces large-scale gel films containing uniform patterns of precipitate, where the gel matrix provides mechanical stability and thus transferability to the patterned thin films, we can produce higher-order complexity by stacking multiple user-defined line patterns. Here we provide some exemplary cases to illustrate this combinatorial approach (Figure 3.3). For example, by aligning and stacking two identical line patterns at 90°or 42°, we create highly regular square- or diamond motifs (Figure 3.3A, B). Because our strategy yields tunable line patterns, the line spacing of each layer can be selected independently, for instance allowing the formation of rectangle motifs by stacking two non-identical line patterns (Figure 3.3C).

Moreover, R-DIP can be readily applied to many other reaction-diffusion processes, enabling patterning of different chemical compositions and the manufacturing of multi-material hybrid motifs. To demonstrate this versatility we produce patterns of three additional materials: lead carbonate, silver chromate, and silver/silver oxide nanoparticles. For lead carbonate patterns, we modify a Liesegang patterning process developed by Isemura in 1936[89], using lead acetate as immersion reagent and sodium carbonate as gel reagent to produce diamond patterns of lead carbonate (Figure 3.3D, see the Materials and Methods for more details). Since each thin film pattern is formed independently, we can produce hybrid motifs by superimposing thin films with patterns of different materials, which we illustrate by producing a rectangular pattern of lead carbonate on silver dichromate (Figure 3.3E).

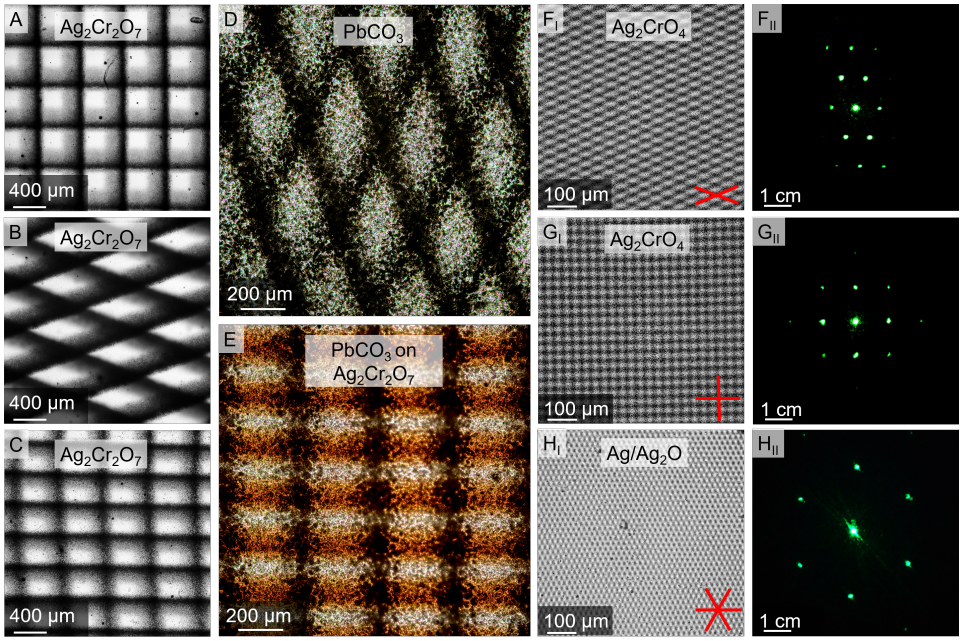

FIGURE 3.3: Aligning and stacking thin films generates higher-order patterning. All images are taken with a light microscope in transmission mode. (A, B) Stacking of identical silver dichromate patterns ($d_1 = d_2 = 285$ µm) at 90 and 42 angles yields square and diamond motifs respectively. (C) Stacking two patterns with non-identical line spacing ($d_1 = 206$ µm, $d_2 = 300$ µm) results in a rectangular motif. (D) Diamond motif produced by superimposing two identical line patterns of lead carbonate. (E) Rectangular hybrid motif produced by superimposing a line pattern of silver dichromate (orange-brown) with a line pattern of lead carbonate (black). (F, G) Diamond and square motifs produced by stacking identical line patterns $d = 31$ µm of silver chromate. Irradiating these microscopic patterns with a green laser ($\lambda = 532$ nm) produces a diffraction pattern that is in good agreement with the microscopic spacing ($d = \frac{m\lambda}{2sin(\theta)}$, diffraction: $d = 32$ µm, directly observed: $d = 31$ µm). (H) Triangular pattern produced by stacking three identical microscopic line patterns $d = 15$ µm of silver/silver oxide nanoparticles, and the diffraction pattern obtained upon irradiation of this pattern with a green laser ($\lambda = 532$ nm).

To display the application potential of R-DIP, we assemble tunable optical diffraction gratings with microscopic line patterns of both silver chromate and of silver nanoparticles. First, we react silver nitrate ($AgNO_3$) as immersion reagent with potassium chromate (K_2CrO_4) as gel reagent to precipitate microscopic lines of silver chromate ($d = 31$ μm). Then, by stacking these microscopic line patterns, we manufacture square and diamond motifs (Figure 3.3F, G), which upon irradiation with a green laser ($\lambda = 532$ nm) show distinct diffraction patterns that are in good agreement with the microscopic structure (diffraction: $d = 32$ μm, directly observed: $d = 31$ μm).

To produce microscopic line patterns of silver/silver oxide nanoparticles, we adapt a previously developed precipitation system, where patterning is induced by the reduction of silver nitrate in a gelatin film containing a small amount of ammonia [32]. Stacking three of these patterns at 60 angles yields a triangular diffraction grating (Figure 3.3H), where again the spacing is in good agreement with the microscopic structure (diffraction: $d = 15.5$ μm, directly observed: $d = 15$ μm), hence illustrating that such self-organized patterns can serve as diffraction gratings with user-defined tunability.

We demonstrate the scalability potential of R-DIP by taking advantage of the simplicity, inherent autonomous nature, and error-correction of our pattern formation process to produce a wafer-scale diffraction grating. For this demonstration, we precipitate silver/silver oxide nanoparticles in a gelatin film to demonstrate large scale patterning using only non-toxic materials. We achieve this by first casting a gelatin film containing a small amount of ammonia onto an A4-sized flexible acetate support sheet (21x29.7 cm), and subsequently inducing pattern formation by slowly immersing the film into a solution of silver nitrate (0.4M) (Figure 3.4A). After drying, this gel film is easily removed from the acetate support sheet to obtain a wafer-scale flexible thin-film (Figure 3.4B) containing a highly uniform pattern consisting of more than 20000 microscopic lines of silver/silver oxide nanoparticles that each have a well-defined and uniform spacing (Figure 3.4C), and which act as a diffraction grating throughout the entire film (Movie C3-S3).

To further explore the functionality potential of R-DIP and specifically demonstrate the large-scale uniformity of our approach, we manufacture an opto-mechanical sensor based on Moiré patterning. When two identical line-patterns are separated by a flexible spacer and aligned parallel, a compression sensor is made. Because deformation of such a sensor induces a misalignment of the two line patterns, higher-order Moiré patterns emerge, with a wavelength dependent on the amount of compression. In this example, we superimpose two identical line patterns of silver dichromate ($d = 200\mu m$), which upon compression reveal macroscopic Moiré patterns (Figure 3.4D, Movie C3-S4). The Moiré patterning wavelength (λ) is directly correlated to the amount of compression (c) with $c \propto \lambda^{-1}$ (Figure 3.4E), and can thus be used as a readout for compression, demonstrating the functionality potential of uniform patterning with microscopic precision in flexible films.

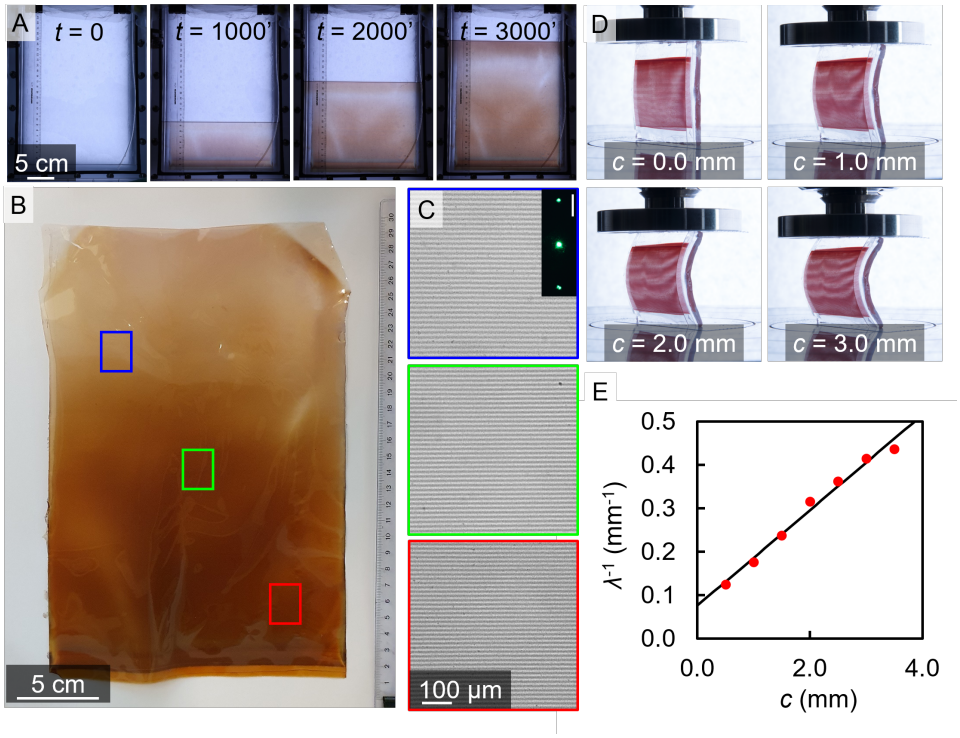

FIGURE 3.4: Scalability and applicability of R-DIP. (A) Snapshots at various times during the wafer-scale patterning of silver/silver oxide micropatterns (see Movie C3-S2). (B) Macroscopic image of the dried A4-sized thin-film after patterning. Note that the precipitated material intensifies during light exposure, which causes a slight color gradient throughout the film. (C) Post-patterning analysis of the wafer-scale pattern, revealing a highly uniform microscopic pattern throughout the entirety of the film. Inset shows the diffraction pattern obtained by irradiating the dried film with a 532 nm laser (see Movie C3-S3, scale-bar = 1 cm). (D) Optomechanical sensor composed of two parallel aligned identical stripe patterns that are separated by a spacer, such that compression results in the emergence of Moiré patterns (see Movie C3-S4). (E) Plot showing the amount of compression (c) versus the inverse of the observed Moiré pattern wavelength (λ^{-1}), with in black a linear fit to this relationship

3.3 Conclusion

Here we introduce reaction-diffusion driven immersion-controlled patterning (R-DIP) as method for creating complex user-defined line motifs in thin films. The power of this patterning strategy is that we exploit autonomous self-organization to create tunable equidistantly spaced microscale lines at wafer-scale that can combinatorially be superimposed into complex hybrid motifs. To demonstrate the functionality potential, we leverage our control over patterning and create tunable diffraction gratings and a sensitive mechanical sensor. An intriguing next step will be downscaling of the pattern spacing to sub-micrometer dimensions, to achieve for instance functionalities such as structural color or optical polarizers. In chapter 5 we investigate the key parameters for downscaling patterns using our immersion-reaction-diffusion model. We find that a challenge in downscaling patterning is that the minimal line spacing is mainly controlled by the rate of nucleation[90] and mobility of species in the gel, which may for instance be optimized by incorporating nucleation promoters in the gel matrix, by changing gel solvent, or by inducing pattern formation at different temperatures.

To demonstrate the proof-of-principle, we apply R-DIP for four different precipitation systems, but we anticipate that extension of this method is straightforwardly possible to many other chemical compositions. For this, the main requirement is that the combination of inner and out reagent results in abrupt self-limiting precipitation of a product. For many nanoparticle or metal-organic-framework syntheses this requirement is met, and recent work shows that combining such syntheses with reaction-diffusion provides control over morphology and size[36,91]. Combining these methods with R-DIP could therefore introduce an additional level of control and provide uniformity to the sizes and morphologies obtained. As such, we foresee that R-DIP can open routes to a large library of material compositions with interesting chemical, electronic or optical properties that can find applications in for instance optical gratings for spectrometers[92], capacitors for electronic devices[93] or electromagnetic shielding[94]. Moreover, we foresee that R-DIP can be extended to entirely different systems based on for instance polymerization or phase-separation, thus opening many directions for self-organizing a large diversity of chemical compositions.

Additionally, the simplicity, autonomous nature and inherent error-correction of R-DIP offers opportunities for robust manufacturing and practical scale-up. Specifically, we recognize that the immersion step and flexibility of the films can be exploited to translate R-DIP into a roll-to-roll process, in which a film is pulled through a solution with immersion reagent to achieve continuous pattern production. Intriguingly, faster immersion results in smaller patterns, such that, almost counter intuitively, faster production yields smaller patterns. Overall, R-DIP offers a versatile and scalable approach for creating complex user-defined line motifs in thin films, enabling a wide range of applications in materials science and manufacturing.

3.4 Materials and Methods

In this section we first state all patterning recipes used, after which we describe the gel casting procedure and the patterning process. All chemicals were used without additional purification. Gelatin was purchased from Sigma-Aldrich and was type A from porcine skin (roughly 300 g Bloom). Agarose was purchased from Sigma-Aldrich and was of type I, with low EEO. 3-[hydroxy(polyethyleneoxy)propyl] heptamethyltrisiloxane (CAS: 67674-67-3) was purchased from Gelest.

3.4.1 Wetting Agent

To mitigate detrimental effects of uneven wetting, we modify the gel by adding a wetting agent. Specifically, we add 3-[hydroxy(polyethyleneoxy)propyl] heptamethyltrisiloxane (HPEO-HMTS), which ensures complete wetting of the gelatin surface, completely negating any surface effects, without affecting pattern formation inside of the gel.

3.4.2 $Ag_2Cr_2O_7$ patterning gel recipe

Gelatin (2.0 g), potassium dichromate (40 mg), HPEO-HMTS (30 µL) and glacial acetic acid (180 µL) are added to DI water (13 mL). This mixture is heated to 65 °C to dissolve gelatin. Simultaneously, a solution of agarose (0.1 g) in water (5 mL) is prepared by microwave heating. These two solutions are combined at 65 °C to yield a liquid gel solution, which sets after cooling to room temperature. Patterning is then induced with an immersion reagent solution of silver nitrate (0.4 M) and acetic acid (0.9 v/v %).

3.4.3 Ag_2CrO_4 patterning gel recipe

Gelatin (2.0 g), potassium chromate (40 mg), HPEO-HMTS (30 µL) and ammonia (25% in water, 240 µL) are added to DI water (13 mL). This mixture is heated to 65 °C to dissolve gelatin. Simultaneously, a solution of agarose (0.1 g) in water (5 mL) is prepared by microwave heating. These two solutions are combined at 65 °C to yield a liquid gel solution, which sets after cooling to room temperature. Patterning is then induced with an immersion reagent solution of silver nitrate (0.4 M in water).

3.4.4 $PbCO_3$ patterning gel recipe

Gelatin (0.5 g) and potassium carbonate (166 mg) are added to DI water (13 mL). This mixture is heated to 65 °C to dissolve gelatin. Simultaneously, a solution of agarose (0.1 g) in water (5 mL) is prepared by microwave heating. These two solutions are combined at 65 °C to yield a liquid gel solution, which sets after cooling to room temperature. Patterning is then induced with an immersion reagent solution of lead acetate (1.0 M in water).

3.4.5 Gel Casting Procedure

Gels are typically cast onto large microscopy glass slides (75x50 mm). First, we preheat these slides to $>$ 65 °C to ensure that gels do not instantly solidify on the glass surface. Then we place a glass slide in a custom holder with edges 0.5 mm taller than the thickness of the glass slide. Roughly 2 mL of hot gel solution is then added onto the glass slide and spread out evenly with a polyoxymethylene (non-stick) block, resulting in a 0.5 mm layer of gel covering one side of the glass slide. After cooling to room temperature, the gel sheets have solidified and are ready for use.

3.4.6 Inducing pattern formation

After the gel films have solidified, they are mounted vertically in an empty chamber. Using a syringe pump, the immersion reagent solution is then added to the bottom of this chamber through PTFE tubing, filling the chamber. Note that the gel film is stationary, but by introducing immersion reagent we are effectively immersing the film (See Figure 3.1A for a schematic of this setup and supporting Figure S3.1 for a detailed explanation on the pattern formation setup).

3.4.7 Wafer-scale patterning of silver nanoparticles

First, gelatin (4.0 g), HPEO-HMTS (60 μL) and ammonia (25% in water, 180 μL) are added to DI water (36 mL)). This mixture is heated to 60°C to dissolve the gelatin. In a special holder, an A4 sized acetate support film is mounted, with a 0.5 mm frame on top. The hot gelatin solution is then poured onto the acetate film and spread evenly with a plastic fondant smoother. This yields a roughly 0.5 mm thick A4 gel sheet on an acetate support. Similarly to previous experiments, albeit scaled up to accommodate the large-scale sheet, the sheet is mounted vertically in an empty chamber, into which silver nitrate (0.4M in water) is slowly pump by a peristaltic pump.

3.5 Supporting Information

3.5.1 Patterning process

The patterning process described in this work uses only a few components, some of which are for inducing pattern formation and others are for live imaging (Figure S3.1).

Pattern formation

- New Era NE-1000 Syringe pump.
- Custom sample holder: two glass windows separated by 6 mm thick, u-shaped Viton rubber, tightened with a stainless steel frame. This effectively makes a big cuvette, in which we can mount glass slides containing gel films.
- 20 mL syringe, connected to PTFE tubing.

The patterning process starts by mounting a gel film supported on a glass slide (75x50 mm) inside an empty sample holder, such that the gel film faces the empty chamber. Then, PTFE tubing connected to a 20 mL syringe introduced to the bottom of this chamber. This syringe is then placed on a syringe pump, with the appropriate rate and volume settings. Starting the syringe pump now starts the patterning process.

Live imaging

- Halogen light source.
- Canon EOS 850D camera with Laowa 25mm F/2.8 2.5-5X Ultra-Macro lens
- xyz stage, with motorized y component.

The entire sample cell can be monitored by a camera equipped with an ultra-macro lens. In order to keep patterning in view, the entire sample holder is mounted on an xyz stage, of which the y component is motorized. As immersion reagent is pumped into the sample holder, the liquid-gel contact line starts moving upwards. By moving the entire sample holder down at the same speed we ensure that patterning occurs in view.

After patterning is complete, gel films are removed from the sample holder, rinsed with DI water and soaked twice in 200 mL DI water for 10 minutes to remove any unreacted reagent.

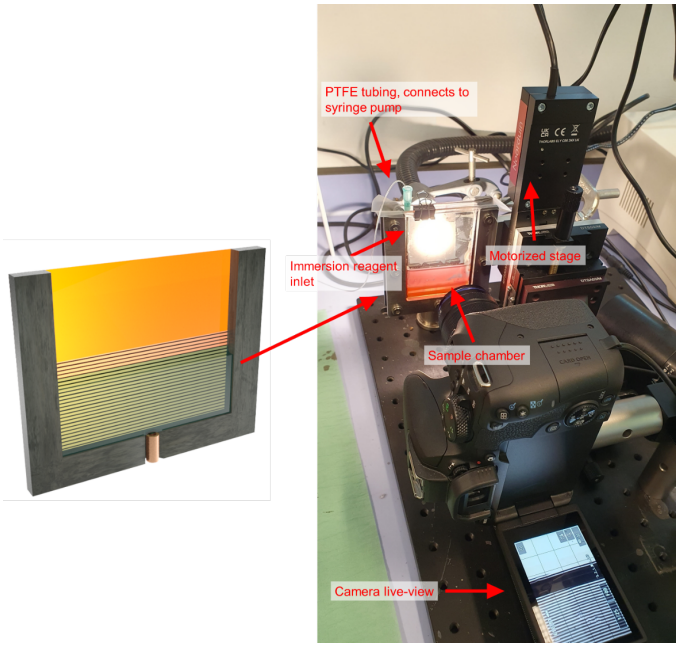

SUPPLEMENTARY FIGURE S3.1: Overview image showing the experimental setup, with the sample chamber containing a gel sheet in the middle connected to a motorized stage that moves the sample down as the liquid-gel contact line moves up. Note that a syringe pump is just out of view on the left, which pumps the immersion reagent through PTFE tubing into the bottom of the sample chamber. The stage, syringe pump and camera are all connected to a PC, which allows for remote monitoring and tuning.

3.5.2 Movies

All movies are publicly available via: `https://github.com/cvcampenhout/Scripts-and-Movies-Thesis`.

C3-S1 Silver Dichromate Patterning using R-DIP.mp4

This movie shows a timelapse of the R-DIP process, where 1 second of movie corresponds to 240 seconds in real time. Out of view, immersion reagent is injected into the empty chamber, which causes the contact line to move upwards. Simultaneously, the chamber is moved downwards at the same speed to keep the contact line and pattern formation in view.

C3-S2 Wafer-scale patterning of silver nanoparticles.mp4

This movie shows a timelapse of the wafer-scale R-DIP process, where the total movie time corresponds to 60 hours real-time. Because the patterns produced in this example are too small to see by naked-eye, we include three zoom-ins of the microscopic pattern taken at the location corresponding to the contact line position at that time in the video.

C3-S3 Large-scale diffraction grating.mp4

In this movie we shine a green (532 nm) laser light at the dried A4-sized diffraction grating, to demonstrate the uniformity of the pattern throughout.

C3-S4 Mechanical Sensing using Moire Patterns.mp4

In this movie we show an opto-mechanical sensor based on Moiré patterns, made by superimposing two identical line patterns of silver dichromate parallel, separated by a flexible spacer. We then slowly compress and decompress the sensor and observe the emerging Moiré pattern.

4 Photography Inspired Customization of Micropatterned Thin-Films

Thin-films patterned with complex motifs are of fundamental interest because of their advanced optical, mechanical and electronic properties, but fabrication of these materials remains challenging. Self-organization strategies, such as immersion controlled reaction-diffusion patterning, have shown great potential for production of patterned thin-films. However, the autonomous nature of such processes limits controllable pattern customizability and complexity. Here, we demonstrate that photography inspired manipulation processes can overcome this limitation to create highly-complex tapestries of micropatterned films (MPF's). Inspired by classical photographic processes, we develop, bleach, expose, fix, and contour MPF's into user-defined shapes and apply photographic toning reactions to convert the chemical composition MPF's, while preserving the original stripe patterns. By applying principles of composite photography, we design highly complex tapestries composed of multiple MPF layers, where each layer can individually be manipulated into a specific shape and composition. By overcoming fundamental limitations, our synergistic approach broadens the design possibilities of reaction-diffusion processes, furthering the potential of self-organization strategies for the development of complex materials.

The work described in this chapter is published in:
C. T. van Campenhout, M. H. Bistervels, J. Rietveld, H. Schoenmaker, M. Kamp, W. L. Noorduin, *Adv. Sci.*, **2024,** 2401625.

4.1 Introduction

Spatial organization of materials in thin films can enhance and exceed the properties that would be achievable by simply the sum of their parts.[1–5] These patterned materials possess many interesting properties and can for instance be used as diffraction gratings for optical devices, anti-reflection coatings for radiative cooling applications, or as nanoscopic capacitors for data storage.[6–11,14] To realize such remarkable properties, it is essential to order the right material at the right place. Already, top-down manufacturing can yield highly complex and user-defined patterns, but the requirement of high precision equipment and specialty chemicals, makes the process oftentimes costly and difficult to scale. From this perspective, bottom-up self-organization strategies are promising to produce complex materials in economically and environmentally friendly ways.[38,71,95–101] Specifically, reaction-diffusion processes are interesting, because they use a delicate interplay between reaction kinetics and diffusion to autonomously order materials into patterns.[21,22,50,56] Recently, we have developed a self-organization strategy to structure silver nanoparticles into well-defined micropatterned thin films (MPF's, Figure 4.1A).[102] By steadily immersing a gel thin-film into a solution with silver ions, we induce precipitation of silver nanoparticles in the gel. These nanoparticles order in highly uniform stripes, regulated by a reaction-diffusion process. Here, a balance between the rates of immersion and diffusion provides both hands-on tunability of the line spacing as well as error-correction against defects for scalable production of uniform patterns.

However, using reaction-diffusion patterning limits the customizability of patterns that can be generated: 1. the interplay between long-range chemical transport and short-range reaction-diffusion results in large-scale uniformity, restricting control in local shaping where patterning occurs;[85] 2. the necessary delicate interplay between reaction and diffusion requires specific combinations of materials, limiting the choice in chemical composition of patterns;[30] 3. the autonomous nature of reaction-diffusion induces specific types of patterns—typically stripes and dots, thus preventing the formation of complex and user-defined patterns.[103] Hence top-down and bottom-up methods offer complementary advantages and limitations. This analysis highlights that the development of synergistic combinations of such methods may offer the new routes for the synthesis of patterned thin films using both hands off self-organization and hands on customization.

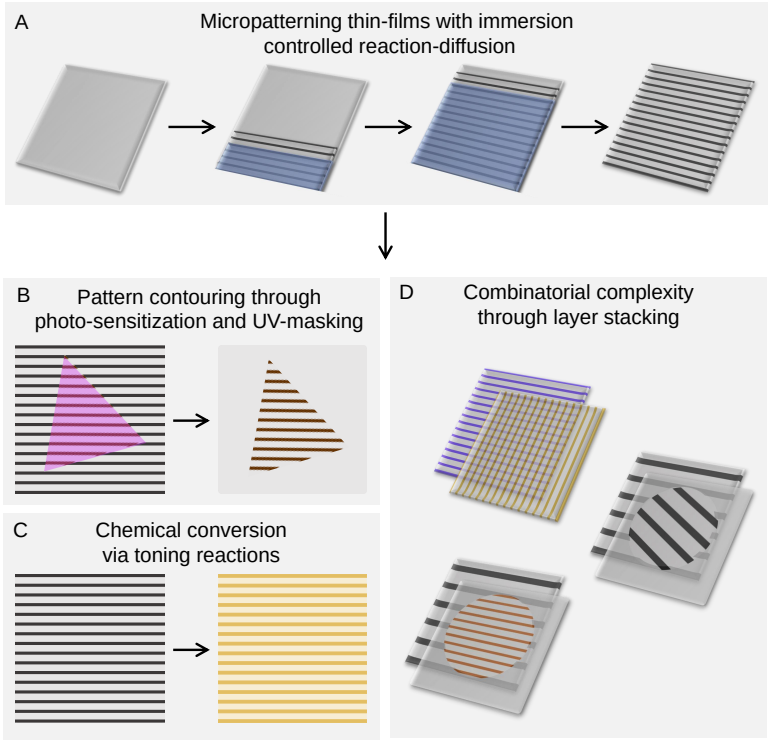

FIGURE 4.1: Photography inspired manipulation processes to customize micropatterned films. (A) Immersion controlled reaction-diffusion patterning to yield MPF's; by steadily immersing a gel thin-film into a solution with silver ions, we induce periodic precipitation of silver nanoparticles arranged in uniform stripes. (B) Contouring of MPF's with photo-sensitization and subsequent UV-masking. (C) Chemical conversion of MPF's by applying toning reactions. (D) Combinatorial complexity through stacking of multiple MPF layers allows for complex tapestry design.

The key insight is that photographic manipulation processes have the potential to overcome the limitations of self-organized reaction-diffusion patterning. For more than a century, research into classical silver halide photography has enabled production of high-resolution images.[104,105] Specifically, darkroom techniques such as development, bleaching and toning have been developed to change the exposure, contrast and color of photographic images.[106] Such photographic manipulation processes enable fabrication of artificial images such as composites. We hypothesize that these photographic techniques can be applied for top-down customization of self-organized patterns. Both photographic plates and MPF's consist of silver particles embedded in thin gelatin films, suggesting that adaptation of photographic manipulation for MPF customization is feasible.

However, there are also distinct differences between photographic plates and MPF's: for classical photography, microscopic silver particles are dispersed randomly throughout the entire film, whereas for MPF's nanoscopic silver particles are ordered in distinct stripes (Figure S1).[107,108] So, despite the chemical similarities, these structural differences render the adaptation of photographic manipulation for MPF customization non-trivial.

In this work, we introduce photography inspired manipulation processes for the customization of self-organized thin films. Analogous to classical photographic processes, we develop, bleach, expose, fix and contour MPF's into user-defined complex shapes (Figure 4.1B). We show that photographic toning processes can convert MPF's, thereby expanding the choice of chemical composition for these patterns (Figure 4.1C). We demonstrate the versatility and customizability of our strategy by applying principles of composition photography to produce stacks of MPF layers, each with independently designed shape and chemical composition, to produce highly complex patterned tapestries (Figure 4.1D).

4.2 Results and Discussion

To demonstrate the proof-of-principle, we first produce uniform MPF's and render them compatible with photographic processes. To produce uniform MPF's, we steadily immerse a gelatin thin film (0.3 mm) into a solution of silver nitrate (0.4 M), yielding silver chloride (AgCl) nanoparticles arranged in tunable uniform microscopic ($d = 10 - 30$ µm) stripe patterns (Figure 4.2A,B I).[32,102] To make these patterns compatible with subsequent photographic processes and to increase the contrast of the pattern, we immerse the MPF into a photographic developer solution that reduces and converts all (AgCl) particles to Ag/Ag_2O. Analysis with optical microscopy reveals a stark increase in contrast, and, importantly, shows that the original stripe pattern and spacing are preserved (Figure 4.2A,B II).

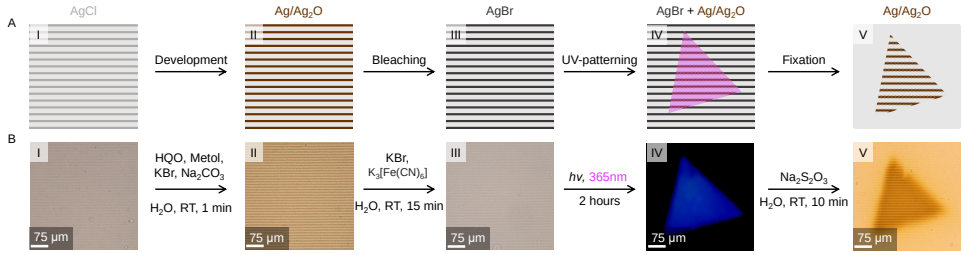

FIGURE 4.2: Photo-sensitization to customize MPF's, (A) schematic, and (B) experimental. The process starts with self-organized micropatterned silver film containing silver chloride, which is poorly visible due to low contrast (I). These MPF's are developed, which converts silver chloride into silver/silver oxide, making the pattern visible by increasing contrast and ensuring compatibility with subsequent processes (II). Then a photo-sensitization step is performed, converting all silver/silver oxide particles into light sensitive silver bromide (III). By illuminating a triangular section of this sensitized film with UV light (365 nm), a part of the MPF is converted from silver bromide back to silver/silver oxide (IV). All silver bromide is then solubilized using a fixation step, to yield an MPF with stripes only in the illuminated area (V).

We contour this MPF using ultraviolet (UV) light. For this, we first make the MPF light sensitive by performing a bleaching procedure. In such a procedure, silver/silver oxide (Ag/Ag_2O) particles convert into light sensitive silver bromide (AgBr) by immersing the MPF in an aqueous solution of potassium bromide and potassium ferricyanide ($K_3[Fe(CN)_6]$) for 15 minutes at room temperature (Figure 4.2A,B III). The AgBr MPF is locally illuminated with UV light (365 nm),[109] using a triangular photo-mask (Figure 4.2A,B IV, see SI for experimental details). In the illuminated region, AgBr is converted into Ag/Ag_2O. Because the particles in an MPF are at least an order of magnitude smaller than those found in photographic films, the particles are much less light sensitive. To counteract this insensitivity, we illuminate with a strong UV-LED (535 $\mu W/mm^2$) for much longer ($>$ 2 hours) than is common in traditional photography. Subsequently, we reveal the photo-pattern by applying a fixation process that removes unreacted AgBr, which is present in areas that have not been illuminated with UV-light. For this, the MPF is immersed in an aqueous solution of sodium thiosulfate ($Na_2S_2O_3$) and washed with water, which solubilizes and removes all unreacted AgBr (Figure 4.2A,B V). Although slight blurring is observed around the edges—attributed to imperfect photomasking, we find that the original stripe pattern is preserved and contoured precisely in the shape of the applied photo-mask, demonstrating the concept of photography inspired manipulation for customizing MPF shapes.

The success of the photo-sensitization process suggests that photographic manipulation processes may be applied to customize MPF's in different ways. Specifically, many reactions have been developed to change the color or longevity of photographs. These so-called toning reactions work by converting the chemical composition of photographs, while retaining the original image. We realize that these photographic toning reactions may enable the chemical conversion of MPF's, and thus hold the potential to disentangle the shape and composition of MPF's.

We investigate this potential of photographic toning recipes by first forming an MPF, which we then develop and tone using various toning recipes. We characterize the pattern and chemical composition before and after each processing step using optical microscopy and energy dispersive x-ray spectroscopy analysis (EDXA). We find that the insulating and flexible nature of the gelatin matrix hinders direct EDXA of the chemical composition of the pattern. To overcome this limitation, we analyze the chemical composition by first liquefying the gel, followed by centrifugation to extract the particles. The extracted particles are then re-dispersed and dropcasted for EDXA (see SI for experimental details and for SEM micrographs of the measured particles).

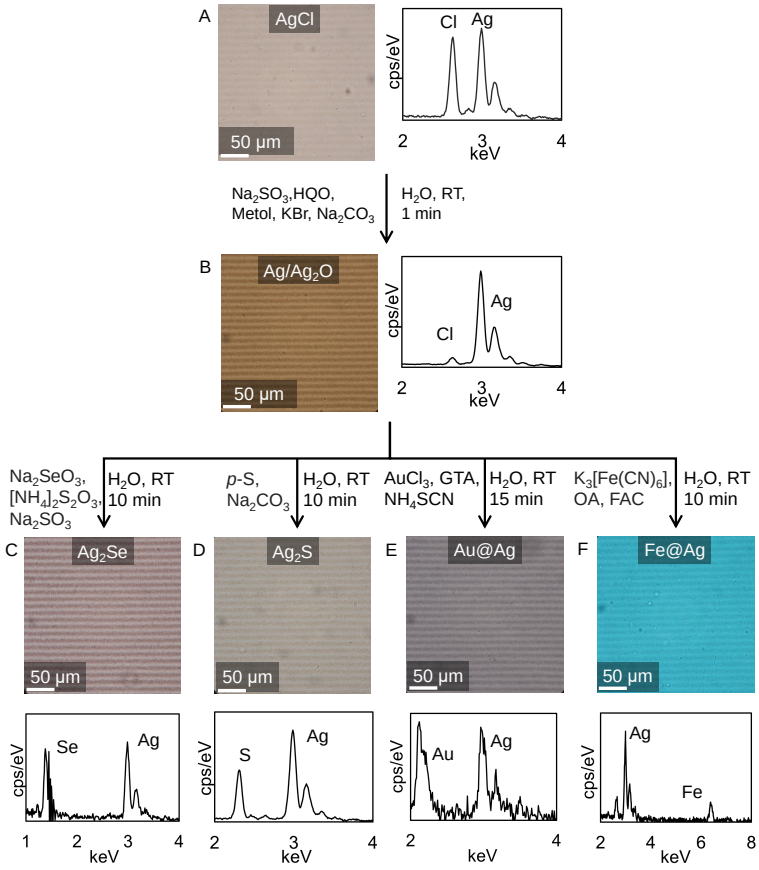

FIGURE 4.3: Chemical conversion through photographic toning reactions (A) Optical microscopy image of a non-processed MPF and EDXA, revealing that the pattern consists of silver chloride particles. (B) Optical microscopy image of a developed MPF and EDXA showing that additional silver is precipitated on top of existing silver chloride. Optical microscopy image and EDXA confirming conversion of developed MPF after different toning reactions to (C) silver selenide, (D) silver sulfide, (E) gold-silver core-shell particles, and (F) iron-silver core-shell particles. Note that all microscopy images were shot at identical contrast and magnification, without additional color correction, to show color changes after toning.

EDXA reveals that initially the MPF indeed consists of AgCl particles, where likely some metallic silver is present because of light exposure (atomic ratio Ag:Cl = 1.24:1, Figure 4.3A). We realize that by using a development step, we can convert these AgCl particles into Ag/Ag_2O, to ensure compatibility with toning processes. For this, we immerse the MPF in a commonly used aqueous developer solution containing sodium sulfite, hydroquinone, metol, potassium bromide and sodium carbonate for one minute. EDXA shows that nearly all AgCl is converted to Ag/Ag_2O (atomic ratio Ag:Cl = 22:1, Figure 4.3B), with preservation of the stripe pattern.

We explore how these developed MPF's can be converted into a range of different chemical compositions. Specifically, to demonstrate the proof-of-principle, we investigate both anionic and cationic toning conversions. For anionic conversions, we apply two commonly used toning processes: selenium and sulfide toning. For selenium toning, we immerse a developed MPF in an aqueous solution of sodium selenite, ammonium thiosulfate and sodium sulfite (commercially available Ilford Harman Selenium toner) for 10 minutes at room temperature to form silver selenide (Ag_2Se), as confirmed by EDXA (Figure 4.3C, atomic ratio Ag:Se = 1.68:1). For sulfide toning, we immerse a developed MPF in an aqueous solution of polysulfide and sodium carbonate at room temperature for 10 minutes to produce silver sulfide (Ag_2S) particles, again confirmed by EDXA (Figure 4.3D, atomic ratio Ag:S = 1.75:1). Importantly, in both cases the original stripe pattern and microscale spacing is preserved, showing pattern-preserving chemical conversion of MPF's using anionic toning processes.

To demonstrate cationic conversions, we apply two commonly used cationic toning reactions: gold toning and Prussian blue (iron) toning. For gold toning, we immerse a developed MPF in an aqueous solution of gold (III) chloride and ammonium thiocyanate in water (commercially available Bergger Goldtoner). This toning solution causes the gelatin matrix to swell. We prevent this undesired swelling by adding a small amount of the crosslinker glutaraldehyde (0.1%) to the toning solution. During this toning process, gold grows on pre-existing Ag/Ag_2O particles and forms a coating, yielding gold-silver (Au@Ag) core-shell particles,[110] consistent with EDXA of the resulting MPF (atomic ratio Au:Ag = 0.42:1). With Prussian blue toning, a similar coating of iron can be produced.[111] For this, a developed MPF is immersed in an aqueous solution of potassium ferricyanide, oleic acid and ferric ammonium citrate in water for 10 minutes at room temperature, yielding iron-silver (Fe@Ag) core-shell particles, demonstrated by a vibrant blue color and the appearance of a distinct iron peak at 6.4 keV in EDXA (molar ratio Fe:Ag = 0.51:1). These results demonstrate that both anionic and cationic conversions can be realized using photographic toning reactions, to customize the chemical composition of MPF's with preservation of the original stripe pattern.

Thus, by combining self-organized pattern formation with photographic manipulation processes we gain three levels of control over MPF's: 1. spacing of tunable stripe patterns through immersion controlled reaction-diffusion; 2. contouring using photo-sensitization and UV-masks; 3. converting chemical composition via toning reactions. These three levels of control can be combined into higher-order complex motifs.

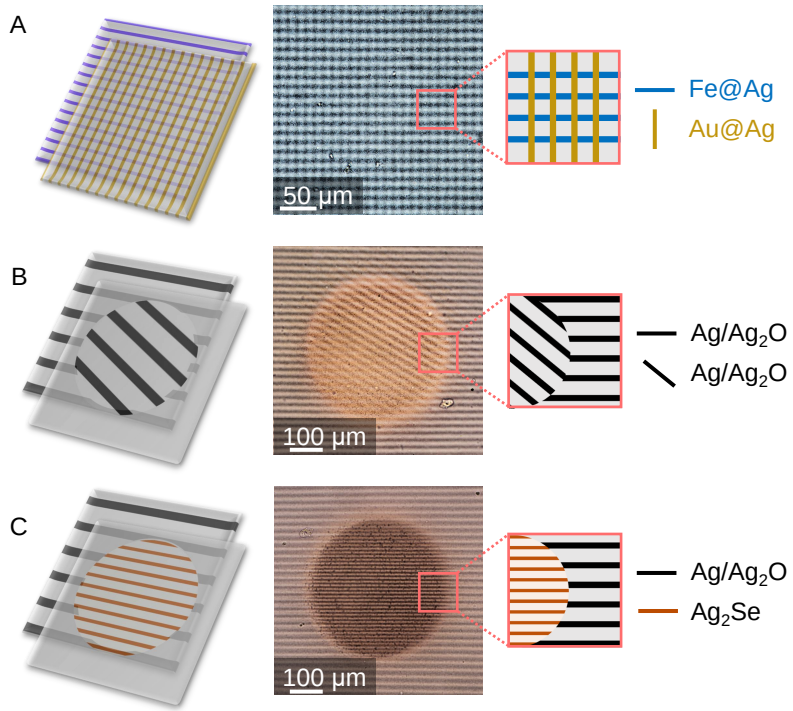

FIGURE 4.4: Inspired by composite photography, stacking of MPF layers provides a combinatorial complex design space. (A) Stacking two spatially identical MPF's of different chemical composition produces a grid where horizontal stripes consist of Fe@Ag and vertical lines consist of Au@Ag. (B) Stacking two UV-patterned MPF's, where the first layer contains stripes only in the positive image of a circle and the second layer only in the negative image of a circle, generates a complex tapestry. (C) Stacking two MPF's with non-identical pattern spacing, varying chemical composition and different UV-patterns demonstrates the full combinatorially complex design space.

We realize that in traditional photographic manipulation processes, multiple layers of photographic negatives can be stacked to create composite images. Akin to such composite photographs, we can produce higher-order complex motifs by stacking layers of MPF's. This opens a combinatorial and versatile design space: by manipulating each individual layer with UV-contouring and chemically conversion, we can create highly complex user-defined tapestries.

We demonstrate this design potential with three examples. First, by stacking two MPF layers of different chemical composition at 90° we produce square patterns, where the horizontal lines contain Fe@Ag and the vertical lines contain Au@Ag (Figure 4.4A). Second, by stacking MPF layers contoured with different UV-masks, we enable the formation of complex motifs with arbitrary selected patterning directions. Here, we demonstrate this by contouring a negative circular image into one MPF, and a positive circular image into another. By stacking these opposite motifs, we obtain a tapestry where the orientation of the pattern is different in and outside of the circle (Figure 4.4B). Third, to demonstrate an even more refined level of complexity, we design a tapestry composed of two MPF layers, each with different line spacing, different shape and different chemical composition. For the first layer, we produce a stripe pattern with line spacing 22 μm and contour a negative circle. For the second layer, we produce a stripe pattern with line spacing 10 μm and contour a positive circle, followed by selenium toning. Stacking these two layers yields a highly complex tapestry, with user-defined pattern spacing, shape and chemical composition (Figure 4.4C).

4.3 Conclusion

In summary, we introduce photography inspired manipulation processes to design complex tapestries of self-organized thin-films. Intriguingly, there exists an historical connection between self-organized patterning and photography: in the late 19th century, the German scientist R. E. Liesegang pioneered photography techniques, and serendipitously discovered self- organized patterns.[29] These so-called Liesegang patterns are at the core of the immersion controlled reaction-diffusion process used to create MPF's. Now, 130 years later, we reunite Liesegang patterns with their photographic roots, to design complex thin-film tapestries. We realize that with immersion controlled reaction-diffusion we can create MPF's that are chemically very similar to classical silver halide photographs. Leveraging these similarities unlocks the complete toolbox of darkroom techniques for user-defined manipulation of MPF's.[106] Using photography inspired techniques we can independently control the shape via photo-sensitization combined with UV-masking, and alter the chemical composition through conversion with toning reactions. Akin to composite photographs, we stack multiple individually manipulated MPF layers to create complex tapestries.

The power of our approach is that it combines the strengths of self-organization and photographic manipulation. By harnessing the autonomy of self-organization and exploiting the automated mass-production of photographic materials, this synergistic approach grants user-control across length-scales: from microscopic control over shape and chemical composition to macroscopic scale-up.

The success of this strategy is surprising: darkroom techniques have been developed for photographs, not MPF's. Nevertheless, we demonstrate that these century old techniques can be readily adapted for recently developed pattern formation processes. Building upon these results, we foresee that other interesting photographic reactions and processes can be extended to fields outside of photography. Specifically, we project exciting opportunities for the field of ion-exchange, where insights from photographic toning processes could inspire the design of new conversion reactions.

Additionally, we foresee new functionalities that exploit the unique combination of tunable long-range ordering with local customization. For instance, already layer stacking allows the formation of Moiré patterns,[102] which combined with local customization could now be designed for information processing, sensing, and advanced optical devices. Furthermore, if self-organized patterns are scaled down one order of magnitude, these structures could exhibit structural coloration. In combination with the local customizability of photography inspired manipulation processes, these structures would allow the fabrication of structurally colored images.

To summarize, we have shown a synergistic approach combining hands-off self-organization and hands-on manipulation for the synthesis of complex thin-film tapestries. We envisage that top-down customization of self-organized patterns using photography inspired manipulation processes will lead to exciting opportunities for the generation of complex patterns with advanced functionalities.

4.4 Supporting Information

4.4.1 Materials

All chemicals were used without additional purification. Gelatin was purchased from Sigma-Aldrich and was type A from porcine skin (roughly 300 g Bloom). 3-[hydroxy(polyethyleneoxy)propyl] heptamethyltrisiloxane (CAS: 67674-67-3) was purchased from Gelest.

4.4.2 Self-Organization Process

Micropatterned films are made using a previously developed reaction-diffusion driven, immersion controlled patterning process (R-DIP). For details on this process, see chapter 3. In short, a thin hydrogel film is cast onto a glass substrate. This film is then slowly immersed in reagent, which diffuses into the hydrogel thereby triggering a reaction-diffusion process that forms periodic precipitation stripes.

Here, we produce microscopic patterns of silver chloride. First, gelatin (1.0 g), 3-[hydroxy(polyethyleneoxy)propyl] heptamethyltrisiloxane (15 μL) and ammonia (25% in water, 40 μL) are added to DI water (9 mL). This mixture is heated to 60° C to dissolve the gelatin, after which 0.3 mm thick gels are cast. These gels are then immersed (1.5 μm/s) in a silver nitrate solution (0.4M in water). Note that chloride ions are already present in type A gelatin, and are not added separately.

4.4.3 Photographic Manipulation Recipes

Developer (Kodak D-19)[106]

- Potassium bromide 50 mg
- Sodium Sulfite 0.90 g
- Hydroquinone 80 mg
- Metol 20 mg
- Sodium carbonate 0.45 g
- Water 8.5 mL

Dissolve at 52 °C, use at room temperature for 1 to 5 minutes.

Bleacher (Print Rehalogenating Bleach)[106]

- Potassium bromide 80 mg
- Potassium ferricyanide 120 mg

- Water 9.8 mL

Use at room temperature for 5 to 10 minutes.

Fixer (Plain Hypo)[106]

- Sodium thiosulfate 4.8 g
- Water 20 mL

Fix at room temperature for 5 to 10 minutes.

Sulfide toner (Kodak T-8)[106]

- Polysulfide 75 mg
- Sodium carbonate 25 mg
- Water 10 mL

Use at room temperature for 5 to 10 minutes.

Selenium toner

Commercially available Ilford Harman Selenium Toner, contains:

- Sodium selenite
- Ammonium thiosulfate
- Sodium sulfite
- Water

Use at room temperature for 5 to 10 minutes.

Iron toner (Kodak T-12)[106]

- Ferric ammonium citrate 20 mg
- Oxalic acid 20 mg
- Potassium ferricyanide 20 mg

Dissolve each separately in water (10 mL), mix equal portions and filter directly prior to use. Use in the dark. Precipitation occurs in light exposed aqueous solutions of ferric ammonium citrate, resulting in particles depositing on the film surface during toning if the toner is exposed to light and/or not filtered properly. Use at room temperature for 5 to 10 minutes.

Gold toner[106]

Commercially available Bergger Goldtoner, contains:

- Gold(III)chloride
- Ammonium thiocyanate
- Water

To prevent MPF swelling, glutaraldehyde (0.1%) was added. Use at room temperature for 5 to 10 minutes.

4.4.4 SEM and EDX analysis

To characterize the chemical composition of the MPF's, we perform energy dispersive x-ray analysis (EDXA), using a FEI Verios 460 scanning electron microscope equipped with an Oxford X-Maxn energy dispersive X-ray spectrometer. Because the gelatin matrix is non-conductive, direct analysis of the particles is impossible. Via critical point drying, collapse of the gel network can be prevented, and spatial information of the particle distribution through the pattern can be obtained (Figure S4.1). However, because the matrix is flexible in this state, particles move away from the e-beam, making high resolution imaging and high acceleration voltages required for EDXA impractical. Therefore, we remove particles from the gelatin matrix prior to SEM/EDXA.

To this aim, MPF sections are placed into a 10 mL Falcon tube, to which boiling water (7 mL) is added. By vortexing directly, all gelatin is solubilized and partially hydrolyzed, such that it no longer forms a gel. By centrifuging at 6500 rpm for 1 hour the particles are separated from the gelatin solution. The supernatant is discarded and again boiling water (7 mL) is added, to remove any leftover gelatin. After again centrifuging at 6500 rpm for 1 hour, the supernatant is removed. The particles are then redispersed in 2-propanol (1 mL) and drop casted onto an aluminum substrate. Figure S4.2 shows the particles used for EDXA.

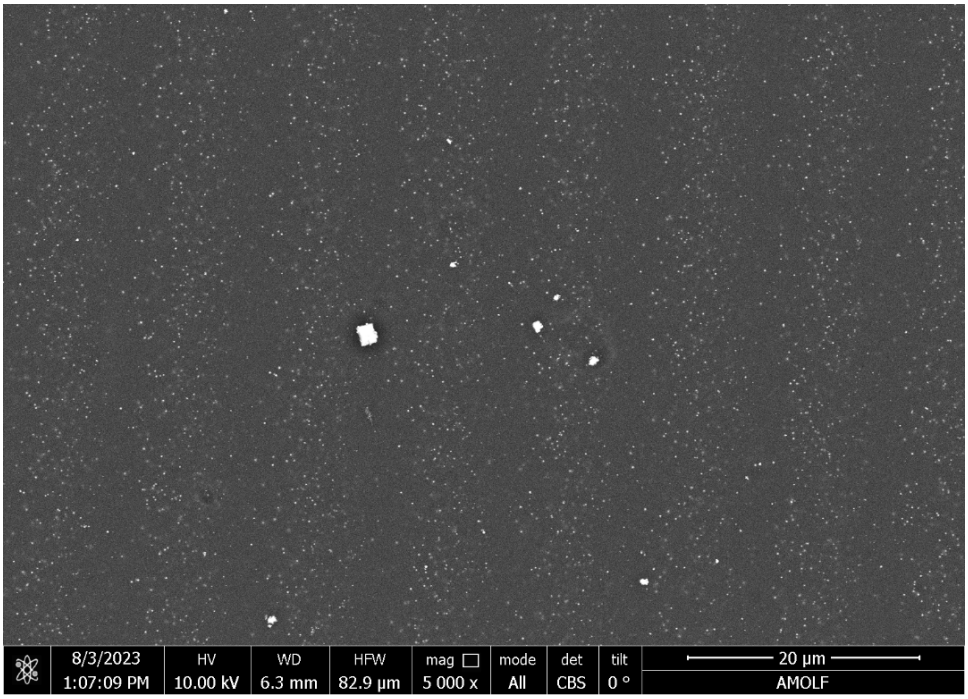

SUPPLEMENTARY FIGURE S4.1: SEM micrograph of an MPF using a Concentric Backscatter (CBS) detector. This sample was prepared by first immersing the MPF in increasing amounts of ethanol (25% EtOH in water -> 50% EtOH in water -> 100% EtOH), followed by critical point drying using a Autosamdri 815 serie B super critical point dryer and sputter coating a 10 nm chromium layer using a Leica EM ACE600 Double sputter coater. The white dots in this micrograph are silver chloride nanoparticles (150-200 nm).

4.4.5 UV patterning

UV patterning was performed using a custom-built microscopy setup. For more details on this setup, see Bistervels et al.[109] This custom microscope contains three main sections: an irradiation parts, a sample holder stage, and an imaging part. For the UV LED irradiation, a lens (Edmund Optics 84–337, focal length (f) = 20.0 mm) collects the light from a 365 nm mounted LED (Thorlabs M365L3, 1290 mW output power). An UV anti-reflection coated plano-convex lenses (Thorlabs LA4148-UV, f = 50.0 mm) projects custom-made photomasks onto the sample through a 10X/0.30 magnification objective (Nikon Plan Fluor). The light intensities of the UV LED is controlled by adjustments of the driving current of the drivers (Thorlabs LEDD1B). The sample holder stage is attached to a Huber CC-K6 cooling bath thermostat.

Developed MPF's were immersed in the bleaching solution for 10 minutes and washed four times in a large excess of DI water for 10 minutes directly prior to UV-patterning. This converts all silver particles to silver bromide, which are light sensitive, and care was taken to keep samples out of direct light. Using the custom microscopy setup described above, samples were photopatterned with 365 nm UV light for $>$ 12 hours, whilst cooled at 10 °C to prevent sample heating and gel decomposition, after which the MPF was removed from the sample holder and directly placed in a fixing bath. After 10 minutes the sample was washed four times with a large excess of DI water.

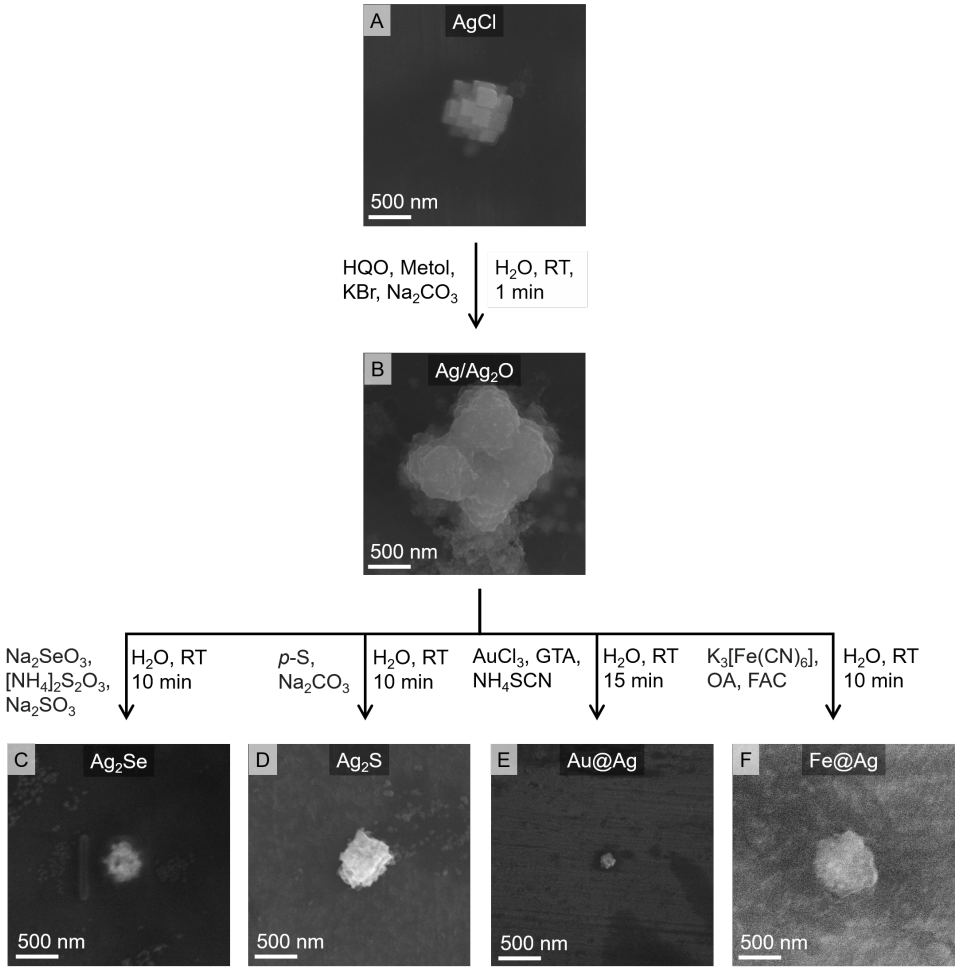

SUPPLEMENTARY FIGURE S4.2: SEM micrographs of the particles used for the EDX analysis shown in Figure 3. (A) Silver chloride particles before any modification. (recorded at 20 kV, 100pA) (B) Silver/silver oxide particles obtained after development (recorded at 20 kV, 100pA). (C) Silver selenide particles obtained after selenium toning (recorded at 20 kV, 100pA). (D) Silver sulfide particles obtained after sulfide toning (recorded at 20 kV, 100pA). (E) Gold-silver particles obtained after gold toning (recorded at 20 kV, 100pA). (F) Iron-silver particles obtained after iron toning (recorded at 30 kV, 100pA).

5 Reaction-Diffusion Modeling

Here, we provide an introduction into reaction-diffusion modeling and provide an in-depth explanation of the numerical models used throughout this theses. This chapter is divided into four sections: first, we explain the basis of numerically approximating reaction-diffusion processes. Then, building on existing reaction-diffusion models, we describe the changes made to accurately capture both mechanical responsiveness as well as immersion controlled patterning. Lastly, we provide an outlook for future experimental Liesegang patterning, with a focus on producing smaller-scale patterns towards the fabrication of advanced functional materials.

The numerical models described in this chapter have been created by me and are used in the following publications:
C. T. van Campenhout, D. N. ten Napel, M. van Hecke, and W. L. Noorduin, *Proc. Natl. Acad. Sci*, 119(39):e2123156119, 2022.
C. T. van Campenhout, H. Schoenmaker, M. van Hecke, and W. L, Noorduin. *Adv. Mater.*, 5(39): 2305191, 2023.
All scripts used in this chapter are publicly available via: `https://github.com/cvcampenhout/Scripts-and-Movies-Thesis`.

5.1 Reaction-diffusion modeling

In this chapter we will describe a model that predicts Liesegang patterning by numerically solving the following one-dimensional reaction-diffusion equation (Equation 5.1):

$$\frac{\partial u}{\partial t} = D\frac{\partial^2 u}{\partial x^2} + R(u). \tag{5.1}$$

Inspired by several well-established Liesegang models[22,30], we create a pre-nucleation model. To this end, we first create discrete grid in which the reaction-diffusion process will take place, then we approximate diffusion and introduce reaction kinetics. Lastly, we combine reactivity and diffusion to form a set of reaction-diffusion equations that accurately reproduce Liesegang patterning.

5.1.1 Discretization

We start by defining the one-dimensional space in which our reaction-diffusion process will take place, x, and divide this into discrete boxes of size Δx. Similarly, we define the total process time t and divide this into discrete time-steps Δt. This discretization effectively creates a 2D-grid, where one axis denotes a specific location and the other axis describes a specific moment in time. Every point on this 2D-grid can hold the concentration of one species.

5.1.2 Diffusion

With the framework of the model in place, we now start modeling diffusion. For this, we use the *forward in time, central in space* (FTCS) scheme, which reads as follows (Equation 5.2):

$$\begin{aligned} &u_x^{t+\Delta t} = u_x^t - \phi_{out} + \phi_{in}, \\ &with\ \phi_{out} = -2\frac{D\Delta t}{\Delta x^2}u_x^t, \\ &and\ \phi_{in} = \frac{D\Delta t}{\Delta x^2}(u_{x-\Delta x}^t + u_{x+\Delta x}^t). \end{aligned} \tag{5.2}$$

A

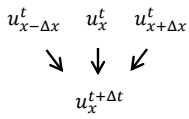

B

t \ x	0	1	2	3	4	5	6
0	0	0	0	100	0	0	0
1	0	0	10	80	10	0	0
2	0	1	16	66	16	1	0
3	0.1	2.4	19.5	56	19.5	2.4	0.1

C

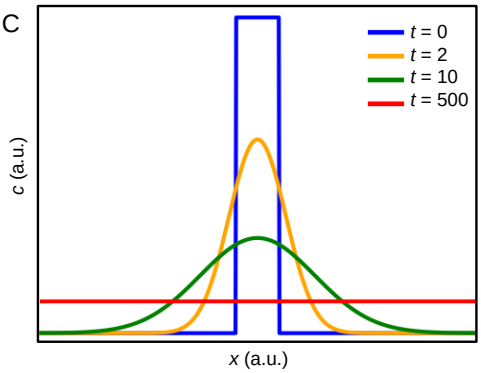

FIGURE 5.1: Approximating diffusion with the FTCS scheme. (A) The FTCS scheme uses the concentration at $t = t$ from three locations, middle (x), left ($x - \Delta x$) and right ($x + \Delta x$), to calculate the concentration at $t = t + \Delta t$ and $x = x$. (B) Example showcasing the FTCS approximation on small scale, showing the concentration will spread throughout the system. (C) By increasing the system size and total time of the process, we can accurately approximate diffusion numerically with the FTCS-scheme.

5

where u is the concentration of a species and D is the diffusion coefficient of that species. This approximation computes the future concentration of a species based on current concentrations in the system. Specifically, the concentration of a *middle* box at a future time-step ($u_x^{t+\Delta t}$) is calculated from both the flux out (ϕ_{out}) and flux in (ϕ_{in}) into that *middle* box. The outward flux is described by a pre-term that describes the discretization size and diffusion coefficient ($\frac{D\Delta t}{\Delta x^2}$) times the current concentration in that space (u_x^t), doubled because for one dimension concentration is lost in two directions. The inward flux (ϕ_{in} is described by the same pre-term ($\frac{D\Delta t}{\Delta x^2}$) times the concentrations directly to the *left* ($u^t_{x-\Delta x}$) and to the *right* ($u^t_{x+\Delta x}$) of *middle* box (Figure 5.1A). This approximation effectively moves concentrations based on the gradient between adjacent boxes: if the concentration in the middle box is higher than that of its neighbors, the total flux will be negative and thus the concentration in that space will decrease. If the concentration of the middle box is lower than that of its neighbors, the total flux will be positive and thus the concentration in that space will increase. Only when concentrations are equal in all spaces will be there be a net-zero flux and thus no change in concentration. Using the FTCS approximation allows us to calculate concentrations at future time-steps with only known current values.

To demonstrate the FTCS approximation, we provide a small-scale example (Figure 5.1B). Here, we start by setting the concentration of species u to 100 at $x = 3$ and $t = 0$ ($u_3^0 = 100$), and concentrations of 0 in all other spaces at $t = 0$. Now, to find the concentration of u at $x = 3$ for the next time-step $t = 1$, we need only three values: the current concentration at $x = 3$ ($u_3^0 = 100$), the concentration the left of $x = 3$ ($u_2^0 = 0$) and the concentration to the right of $x = 3$ ($u_4^0 = 0$). Filling out the FTCS equation (Equation 5.2) for these values shows that the concentration at $x = 3$ will decrease. Because the concentrations at $x = 2$ and $x = 4$ are lower than the concentration at $x = 3$, the flux out from $-2D\frac{\Delta t}{\Delta x^2}(u_3^0)$ will be greater than the flux in from $+ D\frac{\Delta t}{\Delta x^2}(u_2^0 + u_4^0)$. For $D = 0.1$, $\Delta t = 1$ and $\Delta x = 1$ this gives a concentration value: $u_3^1 = 80$. Performing this same calculation for all values of x gives a new set of concentration values for $t = 1$. By repeating these calculations for multiple time-steps, we already see that the initial concentration of u is spreading through the system. If we now decrease the discretization size ($\Delta x = 0.01$) and increase the total system time, we can already accurately approximate diffusive motion (Figure 5.1C).

5

5.1.3 Reactivity

Now that species are able to diffuse through the system, the reaction-diffusion system modeled here is the periodic precipitation of silver dichromate as a result of silver nitrate diffusing into a gel matrix and reacting with potassium dichromate to produce an insoluble salt (Equation 5.3):

$$2\mathrm{Ag}^+(aq) + \mathrm{Cr_2O_7}^{2-}(aq) \rightarrow \mathrm{Ag_2Cr_2O_7}(s). \tag{5.3}$$

In this thesis, we have focus on the pre-nucleation theory for Liesegang pattern formation. This theory divides the above reaction into three steps: 1. sol formation, 2. nucleation and 3. growth.

1. First a sol of $\mathrm{Ag_2Cr_2O_7}$ is formed (Equation 5.4):

$$2\mathrm{Ag}^+(aq) + \mathrm{Cr_2O_7}^{2-}(aq) \underset{k_1}{\longrightarrow} \mathrm{Ag_2Cr_2O_7}(aq). \tag{5.4}$$

2. This sol only nucleates after a specified nucleation threshold c^* is exceeded (Equation 5.5):

$$\mathrm{Ag_2Cr_2O_7}(aq) \underset{k2}{\longrightarrow} \mathrm{Ag_2Cr_2O_7}(s). \tag{5.5}$$

3. Growth onto these nuclei is auto-catalytic and extremely rapid (Equation 5.6):

$$\mathrm{Ag_2Cr_2O_7}(aq) + \mathrm{Ag_2Cr_2O_7}(s) \underset{k3}{\longrightarrow} 2\mathrm{Ag_2Cr_2O_7}(s). \tag{5.6}$$

For each step, a separate rate equation can be written up that describes the change in concentration of specific species over time as the result of that reaction (Equations 5.7 - 5.9):

$$r_1 = -2k_1[Ag^+]^2[Cr_2O_7{}^{2-}], \tag{5.7}$$

$$r_2 = k_2[Ag_2Cr_2O_7]_{aq}\theta([Ag_2Cr_2O_7]_{aq} - c^*), \tag{5.8}$$

$$r_3 = k_3[Ag_2Cr_2O_7]_{aq}[Ag_2Cr_2O_7]_s. \tag{5.9}$$

where r describes a change in concentration over time, k is the rate constant of that specific reaction and θ describes a function that return 0 for $[Ag_2Cr_2O_7]_{aq} < c^*$ and 1 for $[Ag_2Cr_2O_7]_{aq} > c^*$. This theta function models nucleation by only allowing solid material to form after a specified nucleation threshold (c^*) is surpassed. These three rate equations describe all the reactivity required for Liesegang patterning. Note that these rate equations only rely on a species' concentration in a single discrete space, and not on any spatial information, greatly simplifying their incorporation in a discrete reaction-diffusion model.

5.1.4 Combining reaction and diffusion

In the Liesegang patterning process modeled here, there are a few concentrations of species to keep track of: silver ions ($[Ag^+]$); dichromate ions ($[Cr_2O_7{}^{2-}]$); dissolved silver dichromate ($[Ag_2Cr_2O_7]_{aq}$) and precipitated silver dichromate ($[Ag_2Cr_2O_7]_s$). For each of these species, we create a separate reaction-diffusion equation, based on the reactions that species is involved in:

$$\frac{\partial[Ag^+]}{\partial t} = D\frac{\partial t}{\partial x^2}[Ag^+] - 2k_1[Ag^+]^2[Cr_2O_7{}^{2-}], \tag{5.10}$$

$$\frac{\partial[Cr_2O_7{}^{2-}]}{\partial t} = D\frac{\partial t}{\partial x^2}[Cr_2O_7{}^{2-}] - 2k_1[Ag^+]^2[Cr_2O_7{}^{2-}], \tag{5.11}$$

$$\begin{aligned}\frac{\partial[Ag_2Cr_2O_7]_{aq}}{\partial t} &= D\frac{\partial t}{\partial x^2}[Ag_2Cr_2O_7]_{aq} + 2k_1[Ag^+]^2[Cr_2O_7{}^{2-}] \\ &- k_2[Ag_2Cr_2O_7]_{aq}\theta([Ag_2Cr_2O_7]_{aq} - c^*) \\ &- k_3[Ag_2Cr_2O_7]_{aq}[Ag_2Cr_2O_7]_s,\end{aligned} \tag{5.12}$$

$$\begin{aligned}\frac{\partial[Ag_2Cr_2O_7]_s}{\partial t} &= k_2[Ag_2Cr_2O_7]_{aq}\theta([Ag_2Cr_2O_7]_{aq} - c^*) \\ &+ k_3[Ag_2Cr_2O_7]_{aq}[Ag_2Cr_2O_7]_s.\end{aligned} \tag{5.13}$$

Solving this set of reaction-diffusion equations numerically produces precipitation bands at distinct, increasing, intervals (Figure 5.2A, B). Comparing this numerically generated pattern to an experimental Liesegang pattern confirms that this reaction-diffusion model accurately captures Liesegang patterning (Figure 5.2B, C).

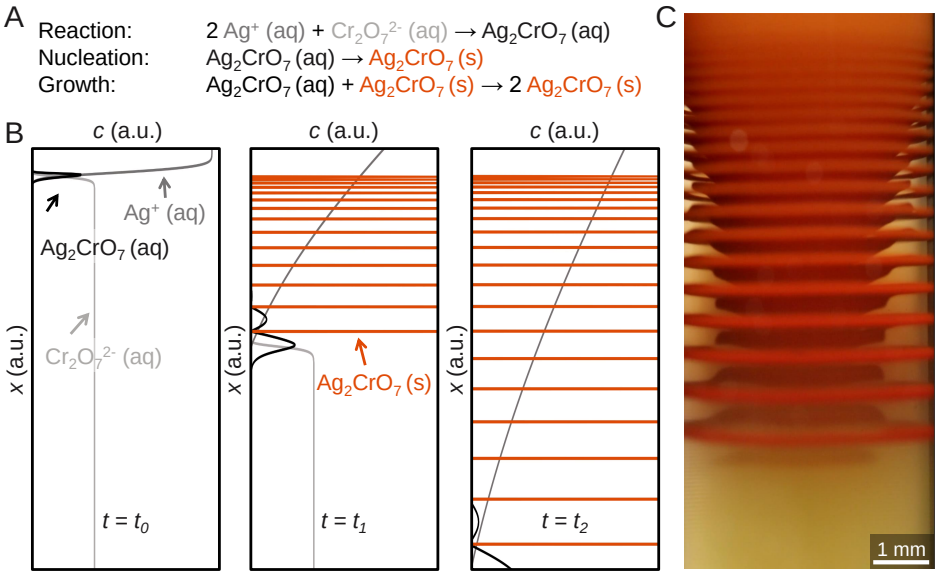

FIGURE 5.2: Classical Liesegang patterns reproduced with reaction-diffusion modeling. (A) Reaction, nucleation and growth equations that describe this Liesegang process. (B) Time-series produced by the numerical reaction-diffusion model, showing the formation of Liesegang patterns over time. (C) Experimental Liesegang pattern of silver dichromate.

5.2 Reaction-diffusion coupled to mechanical responsiveness

In chapter 2, we embed Liesegang processes in mechanical responsive gels (MRGs) to produce highly uniform patterns. In short, calcium ions react with alginate strands present in the MRG matrix, which induces shrinkage, resulting in the formation of a transport channel (Figure 5.3A, B). Through this channel species flow from a reservoir that sits on top of the gel matrix to the reaction-diffusion region. To approximate this self-regulated channel formation, we first compute the crosslinking of alginate (A^-) by Ca^{2+}, to yield a Ca-alginate ($Ca:2A$) complex (Equation 5.14):

$$Ca^{2+} + 2A^- \underset{k_5}{\overset{k_4}{\rightleftharpoons}} Ca:2A. \tag{5.14}$$

The loss of free Ca^{2+} ions caused by this is given by a second order rate equation. Since this coordination is an equilibrium reaction, we also include the opposite de-coordination. This gives the following reaction-diffusion equations for $[Ca^{2+}]$, $[A^-]$ and $[Ca:2A]$ (Equations 5.15 - 5.17):

$$\frac{\partial[Ca^{2+}]}{\partial t} = D\frac{\partial t}{\partial x^2}[Ca^{2+}] - k_4[Ca^{2+}][A]^2 + k_5[Ca:2A], \tag{5.15}$$

$$\frac{\partial[A^-]}{\partial t} = -2k_4[Ca^{2+}][A]^2 + 2k_5[Ca:2A], \tag{5.16}$$

$$\frac{\partial[Ca:2A]}{\partial t} = k_4[Ca^{2+}][A]^2 - k_5[Ca:2A]. \tag{5.17}$$

To add channel formation we first define the leading edge of channel formation, x_e, as the final instance where $[Ca:2A]$ exceeds a specified threshold a^*. For $x < x_e$ chemical transport is instantaneous and solutes are evenly distributed, whereas for $x > x_e$ chemical transport is diffusion limited. To compensate for dilution effects we have introduced V_{in} and V_{out}, the volume of inner and outer electrolyte used respectively. This results in the following equation for solute concentrations where $x < x_e$ (Equation 5.18, X = any solute):

$$[X]_{channel} = [X]_0 \frac{V_{out}}{V_{out} + \beta V_{in}}$$
$$with\ \beta = \frac{l_{channel}}{l_{system}}. \tag{5.18}$$

Here the concentration of solute in the channel $[X]_{channel}$ is calculated from its starting concentration $[X]_0$, the starting volumes used V_{in} and V_{out} and β, which uses the length of the channel and the length of the entire system to describe the relative distance the channel has opened (returns 0 at t_0 and 1 at t_∞). Combining this self-regulated channel formation with the aforementioned periodic precipitation reactions (Equations 5.4 - 5.6) in this MRG model results in a highly uniform periodic precipitation pattern, accurately reproducing the experimental patterns observed (Figure 5.3C, D). As described in chapter 2 modulating the calcium concentration in this model confirms observed experimental trend, where pattern spacing decreases for increasing calcium concentrations (Figure 5.3E).

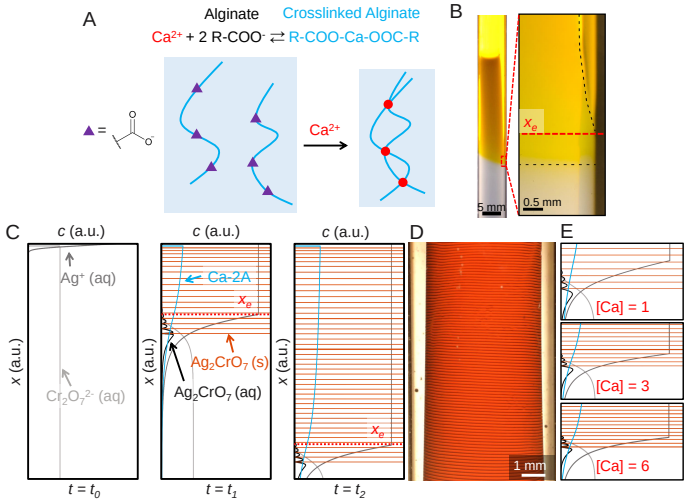

FIGURE 5.3: Liesegang patterning in MRG's. (A) Schematic representation of gel shrinkage as a result of calcium ions crosslinking alginate strands. (B) Experiment showing the formation of a transport channel, where we denote the position of the open transport channel with x_e. (C) Time-series of the MRG reaction-diffusion model, where the self-regulated opening of a transport channel results in highly uniform precipitation bands. (D) Experimental pattern obtained via periodic precipitation of silver dichromate in a gelatin-alginate MRG. (E) Patterns obtained through MRG modelling at varying calcium concentrations, showing a decrease in pattern spacing for increasing calcium concentrations.

5.3 Immersion controlled reaction-diffusion

In chapter 3, we introduce reaction-diffusion driven immersion controlled patterning (R-DIP), a process where Liesegang patterning is controlled by steadily immersing a thin film into a solution (Figure 5.4). In this process, we again look at the periodic precipitation of silver dichromate (Equation 5.3). For this immersion-reaction-diffusion model, we change from a one- to a two-dimensional system, because this more accurately represents reaction-diffusion in thin-films. This changes only the diffusion equation to the following (Equation 5.19):

$$\frac{\partial u}{\partial t} = D\left(\frac{\partial^2 u}{\partial x^2} + \frac{\partial^2 u}{\partial y^2}\right). \tag{5.19}$$

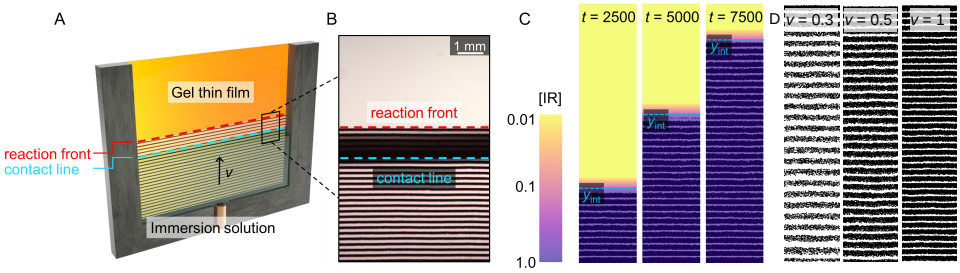

FIGURE 5.4: Immersion controlled reaction-diffusion. (A) Schematic of the experimental setup: a gel thin film is steadily immersed in an immersion solution, inducing periodic precipitation of silver dichromate. (B) Snap-shot during the experimental patterning process, showing the reaction front and contact line. (C) R-DIP model, where we approximate a moving contact line by incorporating a moving y_{int}, yielding highly uniform patterns. (E) Patterns obtained at varying immersion speeds v, reproducing the experimental trend that stripe distances decreases for increasing immersion speeds.

With the FTCS approximation, this change to two dimensions is easily made: we perform the same adjacency calculation as before, but now twice; once for the x-direction and once for the y-direction. Because reactivity only depends on concentration in a specific discrete space, and does not take the surroundings into account, changing to two dimensions does not affect the reaction rate equations. Thus, combining the two dimensional diffusion equation with the periodic precipitation reactions of silver dichromate used before (Equations 5.4-5.6) yields the following set of two-dimensional reaction-diffusion equations (Equations 5.20 - 5.23):

$$\frac{\partial[\mathrm{Ag}^+]}{\partial t} = D\left(\frac{\partial^2[\mathrm{Ag}^+]}{\partial x^2} + \frac{\partial^2[\mathrm{Ag}^+]}{\partial y^2}\right) - 2k_1[\mathrm{Ag}^+]^2[{\mathrm{Cr_2O_7}}^{2-}], \tag{5.20}$$

$$\frac{\partial[{\mathrm{Cr_2O_7}}^{2-}]}{\partial t} = D\left(\frac{\partial^2[{\mathrm{Cr_2O_7}}^{2-}]}{\partial x^2} + \frac{\partial^2[{\mathrm{Cr_2O_7}}^{2-}]}{\partial y^2}\right) - 2k_1[\mathrm{Ag}^+]^2[{\mathrm{Cr_2O_7}}^{2-}], \tag{5.21}$$

$$\begin{aligned}\frac{\partial[\mathrm{Ag_2Cr_2O_7}]_{\mathrm{aq}}}{\partial t} &= D\left(\frac{\partial^2[\mathrm{Ag_2Cr_2O_7}]_{aq}}{\partial x^2} + \frac{\partial^2[\mathrm{Ag_2Cr_2O_7}]_{aq}}{\partial y^2}\right) + 2k_1[\mathrm{Ag}^+]^2[{\mathrm{Cr_2O_7}}^{2-}] \\ &- k_2[\mathrm{Ag_2Cr_2O_7}]_{aq}\theta([\mathrm{Ag_2Cr_2O_7}]_{aq} - c^*) \\ &- k_3[\mathrm{Ag_2Cr_2O_7}]_{aq}[\mathrm{Ag_2Cr_2O_7}]_s,\end{aligned} \tag{5.22}$$

$$\begin{aligned}\frac{\partial[\mathrm{Ag_2Cr_2O_7}]_s}{\partial t} &= k_2[\mathrm{Ag_2Cr_2O_7}]_{aq}\theta([\mathrm{Ag_2Cr_2O_7}]_{aq} - c^*) \\ &+ k_3[\mathrm{Ag_2Cr_2O_7}]_{aq}[\mathrm{Ag_2Cr_2O_7}]_s.\end{aligned} \tag{5.23}$$

Now, to incorporate immersion, we introduce a time-dependent immersion reagent interface y_{int}, which moves at a constant, user-defined speed speed v (Equation 5.24):

$$y_{int} = v \times t \tag{5.24}$$

Subsequently, for all immersed points we set the concentration of immersion reagent ($[Ag]_{y<y_{int}}$) as equal to the starting concentration ($[Ag]_0$). Again, to compensate for dilution effects we take the total volumes of immersion and gel reagent (V_{im} and V_{gel} respectively) into account, as well as the portion of the chamber that has been filled (β). (Equation 5.25):

$$\begin{aligned}&[Ag]_{y<y_{int}} = [Ag]_0 \times \frac{V_{im}}{V_{im} + \beta V_{gel}}, \\ &with\ \beta = \frac{y_{int}}{l_{system}}.\end{aligned} \tag{5.25}$$

This set of reaction-diffusion equations combined with a moving immersion reagent interface reproduces uniform patterning, again closely resembling the experimentally observed pattern (Figure 5.4B, C).

5.4 Downscaling Liesegang patterning

In this section, we will use the immersion controlled reaction-diffusion model to investigate the key parameters for downscaling pattern formation. To this end, we adapt the immersion-reaction-diffusion model described above to incorporate the silver chloride periodic precipitation system (see chapter 3and 4). In this periodic precipitation system, a gel containing sodium chloride is steadily immersed into a solution of silver nitrate to produce microscopic patterns of silver chloride nanoparticles (Figure 5.5A). Seeing as most optical applications require submicrometer patterns, it is of great interest to reduce this length-scale by at least one order of magnitude. To this aim, we investigate the parameter space of this periodic precipitation system using our numerical model.

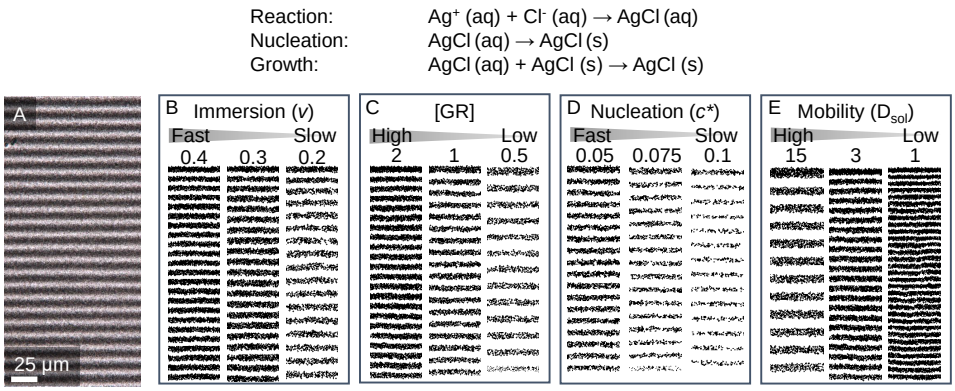

FIGURE 5.5: Modeling reveals key parameters for smaller stripe patterns. (A) Experimental silver chloride pattern with stripe distance $d = 12$ µm. Modeling shows that: (B) increasing the immersion speed (v) results in decreased stripe distances; (C) increasing the gel reagent concentration ([GR]) results in decreased in stripe distances; (D) reducing the nucleation threshold ($c*$) causes fast nucleation resulting in a decrease in stripe distance; (E) mobility of the crystallizing phase (here D_{sol} for $[AgCl_{aq}]$) is critical for patterning, where low mobility results in significantly reduced stripe distances.

From chapter 3 we know that controlling immersion speeds allows for tuning of the stripe distance, which plateaus around $d = 5$ µm. With this immersion controlled reaction-diffusion model, we accurately reproduce this trend, where increasing immersion speeds result in smaller stripe distances (Figure 5.5B). Besides immersion speeds, modeling allows us to easily screen other parameters of this reaction-diffusion process.

First, we screen a range of both immersion- and gel-reagent concentrations, and find that stripe distances are especially dependent on gel reagent concentration, where increasing concentrations result in smaller stripe distances (Figure 5.5C). Additionally, we investigate two parameters that are difficult to test experimentally: nucleation rates and species mobility. For nucleation rates, we find that fast nucleation is key: if nucleation becomes too slow, patterns become poorly defined and low-fidelity (Figure 5.5D). Investigating mobility, specifically mobility of the crystallizing phase ($[AgCl_{aq}]$), reveals that there is a strong dependency of stripe distance on mobility: lower mobility drastically reduces stripe distances (Figure 5.5E).

Combining these results provides a solid foundation for future experimental work on reducing stripe distances to sub-micrometer length-scales. Specifically, the system needs to show fast nucleation, with high gel reagent concentration and low species mobility. Experimentally, this can be achieved by for instance lowering the processing temperature, which would decrease mobility and potentially increase nucleation rates. Additionally, other solvents besides water can be tested, which will drastically change the mobility and solubility of all species. Using numerical modeling has demonstrated that downscaling patterns is theoretically possible, and has provided key pointers for experimental design to achieve this goal.

Bibliography

[1] Philip Ball. *The self-made tapestry: pattern formation in nature*. Oxford University Press, Inc., 1999.

[2] Ulrike GK Wegst, Hao Bai, Eduardo Saiz, Antoni P Tomsia, and Robert O Ritchie. Bioinspired structural materials. *Nature Materials*, 14(1):23–36, 2015.

[3] Michaela Eder, Shahrouz Amini, and Peter Fratzl. Biological composites—complex structures for functional diversity. *Science*, 362(6414):543–547, 2018.

[4] Jingyun Huang, Xudong Wang, and Zhong Lin Wang. Controlled replication of butterfly wings for achieving tunable photonic properties. *Nano Letters*, 6 (10):2325–2331, 2006.

[5] Yael Helfman Cohen, Yoram Reich, and Sara Greenberg. Biomimetics: structure–function patterns approach. *Journal of Mechanical Design*, 136(11): 111108, 2014.

[6] Matthew R Begley, Daniel S Gianola, and Tyler R Ray. Bridging functional nanocomposites to robust macroscale devices. *Science*, 364(6447):eaav4299, 2019.

[7] Lars Wågberg and Johan Erlandsson. The use of layer-by-layer self-assembly and nanocellulose to prepare advanced functional materials. *Advanced Materials*, 33(28):2001474, 2021.

[8] Yuanyuan Wang, Igor Fedin, Hao Zhang, and Dmitri V Talapin. Direct optical lithography of functional inorganic nanomaterials. *Science*, 357(6349): 385–388, 2017.

[9] André R Studart. Towards high-performance bioinspired composites. *Advanced Materials*, 24(37):5024–5044, 2012.

[10] Evelijn Akerboom, Tom Veeken, Christoph Hecker, Jorik Van De Groep, and Albert Polman. Passive radiative cooling of silicon solar modules with photonic silica microcylinders. *ACS Photonics*, 9(12):3831–3840, 2022.

[11] Woo Lee, Hee Han, Andriy Lotnyk, Markus Andreas Schubert, Stephan Senz, Marin Alexe, Dietrich Hesse, Sunggi Baik, and Ulrich Gösele. Individually addressable epitaxial ferroelectric nanocapacitor arrays with near tb inch- 2 density. *Nature Nanotechnology*, 3(7):402–407, 2008.

[12] Parag Banerjee, Israel Perez, Laurent Henn-Lecordier, Sang Bok Lee, and Gary W Rubloff. Nanotubular metal–insulator–metal capacitor arrays for energy storage. *Nature Nanotechnology*, 4(5):292–296, 2009.

[13] Yejing Liu, Hao Wang, Jinfa Ho, Ryan C Ng, Ray JH Ng, Valerian H Hall-Chen, Eleen HH Koay, Zhaogang Dong, Hailong Liu, Cheng-Wei Qiu, et al. Structural color three-dimensional printing by shrinking photonic crystals. *Nature Communications*, 10(1):4340, 2019.

[14] Yan Gu, Yishuo Zhang, Jieqiong Lin, Huibo Zhao, Haihang Ma, Hongwei Yao, Mingshuo Kang, Bin Fu, and Silin Liu. The fabrication of high-performance diffraction gratings via vibration-assisted uv nanoimprinting lithography. *Colloids and Surfaces A: Physicochemical and Engineering Aspects*, 679:132569, 2023.

[15] Yi-Long Li, Nan-Nan Li, Di Wang, Fan Chu, Sin-Doo Lee, Yi-Wei Zheng, and Qiong-Hua Wang. Tunable liquid crystal grating based holographic 3d display system with wide viewing angle and large size. *Light: Science & Applications*, 11(1):188, 2022.

[16] A Gibbons, Orsolya Láng, Y Kojima, M Ito, K Ono, K Tanaka, and E Sivaniah. Real-time visualization of cardiac cell beating behaviour on polymer diffraction gratings. *RSC Advances*, 7(81):51121–51129, 2017.

[17] Bai-Ou Guan, Long Jin, Yang Zhang, and Hwa-Yaw Tam. Polarimetric heterodyning fiber grating laser sensors. *Journal of Lightwave Technology*, 30(8): 1097–1112, 2011.

[18] Tiia Monto, 2016. URL `https://commons.wikimedia.org/wiki/File:Tetraodon_mbu_2.jpg`.

[19] Didier Descouens, 2011. URL `https://commons.wikimedia.org/w/index.php?curid=15656403with`.

[20] Fabian Heinemann, 2007. URL `https://commons.wikimedia.org/wiki/File:Bruchfl%C3%A4che_eines_Perlmuttst%C3%BCcks.JPG`.

[21] A. M. Turing. The chemical basis of morphogenesis. *Philosophical Transactions of the Royal Society of London. Series B, Biological Sciences*, 237(641):37–72, 1952.

[22] Bartosz A Grzybowski. *Chemistry in motion: reaction-diffusion systems for micro-and nanotechnology*. John Wiley & Sons, 2009.

[23] Salva Duran-Nebreda, Jordi Pla, Blai Vidiella, Jordi Pinero, Nuria Conde-Pueyo, and Ricard Solé. Synthetic lateral inhibition in periodic pattern forming microbial colonies. *ACS Synthetic Biology*, 10(2):277–285, 2021.

[24] James Dickson Murray, E Ann Stanley, and David L Brown. On the spatial spread of rabies among foxes. *Proceedings of the Royal society of London. Series B. Biological sciences*, 229(1255):111–150, 1986.

[25] Sergey N Semenov, Lewis J Kraft, Alar Ainla, Mengxia Zhao, Mostafa Baghbanzadeh, Victoria E Campbell, Kyungtae Kang, Jerome M Fox, and George M Whitesides. Autocatalytic, bistable, oscillatory networks of biologically relevant organic reactions. *Nature*, 537(7622):656–660, 2016.

[26] Michael G Howlett and Stephen P Fletcher. From autocatalysis to survival of the fittest in self-reproducing lipid systems. *Nature Reviews Chemistry*, 7 (10):673–691, 2023.

[27] Giulietta Maruggi, Jeffrey B Ulmer, Rino Rappuoli, and Dong Yu. Self-amplifying mrna-based vaccine technology and its mode of action. In *mRNA Vaccines*, pages 31–70. Springer, 2021.

[28] Wiktor, 2015. URL `https://commons.wikimedia.org/wiki/File:Belousov-Zhabotinsky_reaction.jpg`.

[29] Raphael E Liesegang. Über einige eigenschaften von gallerten. *Naturwissenschaftliche Wochenschrift*, 11:353–362, 1896.

[30] Hideki Nabika, Masaki Itatani, and István Lagzi. Pattern formation in precipitation reactions: The liesegang phenomenon. *Langmuir*, 36(2):481–497, 2019.

[31] Gerhard Ammon and R Ammon. Über diffusionen in gelatine und rhythmische fällungen von magnesiumhydroxyd. *Kolloid-Zeitschrift*, 73(2):204–219, 1935.

[32] Roché M Walliser, Rita Tóth, István Lagzi, Daniel Mathys, Laurent Marot, Artur Braun, Catherine E Housecroft, and Edwin C Constable. Understanding the formation of aligned, linear arrays of ag nanoparticles. *RSC Advances*, 6(34):28388–28392, 2016.

[33] Christopher J. Campbell, Eric Baker, Marcin Fialkowski, Agnieszka Bitner, Stoyan K. Smoukov, and Bartosz A. Grzybowski. Self-organization of planar microlenses by periodic precipitation. *Journal of Applied Physics*, 97:126102, 2005.

[34] Mohammad Morsali, Muhammad Turab Ali Khan, Rahym Ashirov, Gábor Holló, H Tarik Baytekin, Istvan Lagzi, and Bilge Baytekin. Mechanical control of periodic precipitation in stretchable gels to retrieve information on elastic deformation and for the complex patterning of matter. *Advanced Materials*, 32(10):1905779, 2020.

[35] Muhammad Turab Ali Khan, Joanna Kwiczak-Yiğitbaşı, Pedram Tootoonchian, Mohammad Morsali, Istvan Lagzi, and Bilge Baytekin. Chemical tracking of temperature by concurrent periodic precipitation pattern formation in polyacrylamide gels. *ACS Applied Materials & Interfaces*, 14(5):7252–7260, 2022.

[36] Szabolcs Farkas, Gábor Holló, Gábor Schuszter, Ágota Deák, László Janovák, Viktória Hornok, Masaki Itatani, Hideki Nabika, Dezso Horváth, Agota Tóth, et al. Reaction–diffusion assisted synthesis of gold nanoparticles: Route from the spherical nano-sized particles to micrometer-sized plates. *The Journal of Physical Chemistry C*, 125(47):26116–26124, 2021.

[37] George M. Whitesides and Bartosz Grzybowski. Self-assembly at all scales. *Science*, 295:2418–2421, 3 2002.

[38] Luca Cera and Christoph A. Schalley. Under diffusion control: from structuring matter to directional motion. *Advanced Materials*, 30:1707029, 9 2018.

[39] Richard M. Parker, Giulia Guidetti, Cyan A. Williams, Tianheng Zhao, Aurimas Narkevicius, Silvia Vignolini, and Bruno Frka-Petesic. The self-assembly of cellulose nanocrystals: Hierarchical design of visual appearance. *Advanced Materials*, 30:1704477, 5 2018.

[40] Alexander Finnemore, Pedro Cunha, Tamaryn Shean, Silvia Vignolini, Stefan Guldin, Michelle Oyen, and Ullrich Steiner. Biomimetic layer-by-layer assembly of artificial nacre. *Nature Communications*, 3:966, 2012.

[41] L.-B. Mao, H.-L. Gao, H.-B. Yao, L. Liu, H. Colfen, G. Liu, S.-M. Chen, S.-K. Li, Y.-X. Yan, Y.-Y. Liu, and S.-H. Yu. Synthetic nacre by predesigned matrix-directed mineralization. *Science*, 354:107–110, 10 2016.

[42] Anthony McDougal, Benjamin Miller, Meera Singh, and Mathias Kolle. Biological growth and synthetic fabrication of structurally colored materials. *Journal of Optics*, 21:073001, 6 2019.

[43] Michaela Eder, Shahrouz Amini, and Peter Fratzl. Biological composites—complex structures for functional diversity. *Science*, 362:543–547, 11 2018.

[44] André R. Studart. Towards high-performance bioinspired composites. *Advanced Materials*, 24:5024–5044, 9 2012.

[45] Sylvain Deville, Eduardo Saiz, Ravi K. Nalla, and Antoni P. Tomsia. Freezing as a path to build complex composites. *Science*, 311:515–518, 1 2006.

[46] M. Valentina Dinu, M. Murat Ozmen, E. Stela Dragan, and Oguz Okay. Freezing as a path to build macroporous structures: Superfast responsive polyacrylamide hydrogels. *Polymer*, 48:195–204, 1 2007.

[47] Zhe Tan, Shengfu Chen, Xinsheng Peng, Lin Zhang, and Congjie Gao. Polyamide membranes with nanoscale turing structures for water purification. *Science*, 360:518–521, 5 2018.

[48] Shigeru Kondo and Takashi Miura. Reaction-diffusion model as a framework for understanding biological pattern formation. *Science*, 329(5999): 1616–1620, 2010.

[49] Judit Horváth, István Szalai, and Patrick De Kepper. An experimental design method leading to chemical turing patterns. *Science*, 324:772–775, 5 2009.

[50] Mark C Cross and Pierre C Hohenberg. Pattern formation outside of equilibrium. *Reviews of Modern Physics*, 65(3):851, 1993.

[51] Amanda J Ackroyd, Gábor Holló, Haridas Mundoor, Honghu Zhang, Oleg Gang, Ivan I Smalyukh, István Lagzi, and Eugenia Kumacheva. Self-organization of nanoparticles and molecules in periodic liesegang-type structures. *Science Advances*, 7:3801–3817, 2021.

[52] Hideki Nabika, Masaki Itatani, and István Lagzi. Pattern formation in precipitation reactions: The liesegang phenomenon. *Langmuir*, 36:481–497, 1 2020.

[53] Elias Nakouzi and Oliver Steinbock. Self-organization in precipitation reactions far from the equilibrium. *Science Advances*, 2, 8 2016.

[54] Oscar Giraldo, Stephanie L. Brock, Manuel Marquez, Steven L. Suib, Hugh Hillhouse, and Michael Tsapatsis. Spontaneous formation of inorganic helices. *Nature*, 405:38, 5 2000.

[55] Stoyan K. Smoukov, Agnieszka Bitner, Christopher J. Campbell, Kristiana Kandere-Grzybowska, and Bartosz A. Grzybowski. Nano- and microscopic surface wrinkles of linearly increasing heights prepared by periodic precipitation. *Journal of the American Chemical Society*, 127:17803–17807, 12 2005.

[56] Bartosz A. Grzybowski, Kyle J.M. Bishop, Christopher J. Campbell, Marcin Fialkowski, and Stoyan K. Smoukov. Micro- and nanotechnology via reaction-diffusion. *Soft Matter*, 1:114–128, 7 2005.

[57] Yixiao Dong, Allison N Ramey-Ward, and Khalid Salaita. Programmable mechanically active hydrogel-based materials. *Advanced Materials*, page 2006600, 2021.

[58] Yizeng Li, Konstantinos Konstantopoulos, Runchen Zhao, Yoichiro Mori, and Sean X. Sun. The importance of water and hydraulic pressure in cell dynamics. *Journal of Cell Science*, 133, 10 2020.

[59] Muamer Kadic, Graeme W. Milton, Martin van Hecke, and Martin Wegener. 3d metamaterials. *Nature Reviews Physics*, 1:198–210, 3 2019.

[60] Alexander Finnemore, Pedro Cunha, Tamaryn Shean, Silvia Vignolini, Stefan Guldin, Michelle Oyen, and Ullrich Steiner. Biomimetic layer-by-layer assembly of artificial nacre. *Nature Communications*, 3(1):966, 2012.

[61] Anthony McDougal, Benjamin Miller, Meera Singh, and Mathias Kolle. Biological growth and synthetic fabrication of structurally colored materials. *Journal of Optics*, 21(7):073001, 2019.

[62] Eric SA Goerlitzer, Robin N Klupp Taylor, and Nicolas Vogel. Bioinspired photonic pigments from colloidal self-assembly. *Advanced Materials*, 30(28): 1706654, 2018.

[63] Katherine R Phillips, Grant T England, Steffi Sunny, Elijah Shirman, Tanya Shirman, Nicolas Vogel, and Joanna Aizenberg. A colloidoscope of colloid-based porous materials and their uses. *Chemical Society Reviews*, 45(2):281–322, 2016.

[64] Dhriti Nepal, Saewon Kang, Katarina M Adstedt, Krishan Kanhaiya, Michael R Bockstaller, L Catherine Brinson, Markus J Buehler, Peter V Coveney, Kaushik Dayal, Jaafar A El-Awady, Luke C Henderson, David L Kaplan, Sinan Keten, Nicholas A Kotov, George C Schatz, Silvia Vignolini, Fritz Vollrath, Yusu Wang, Boris I Yakobson, Vladimir V Tsukruk, and Hendrik Heinz. Hierarchically structured bioinspired nanocomposites. *Nature Materials*, 22(1):18–35, 2023.

[65] Michael M Lerch, Alison Grinthal, and Joanna Aizenberg. Homeostasis as inspiration—toward interactive materials. *Advanced Materials*, 32(20):1905554, 2020.

[66] Anne-Déborah C Nguindjel, Pieter J de Visser, Mitch Winkens, and Peter A Korevaar. Spatial programming of self-organizing chemical systems using sustained physicochemical gradients from reaction, diffusion and hydrodynamics. *Physical Chemistry Chemical Physics*, 24(39):23980–24001, 2022.

[67] Haixiang Han, Shantanu Kallakuri, Yuan Yao, Curtis B Williamson, Douglas R Nevers, Benjamin H Savitzky, Rachael S Skye, Mengyu Xu, Oleksandr Voznyy, Julia Dshemuchadse, Lena F Kourkoutis, Steven J Weinstein, Tobias Hanrath, and Richard D Robinson. Multiscale hierarchical structures from a nanocluster mesophase. *Nature Materials*, 21(5):518–525, 2022.

[68] José María De Teresa. *Nanofabrication: Nanolithography techniques and their applications*. IOP Publishing, 2020.

[69] Martin Feldman. *Nanolithography: the art of fabricating nanoelectronic and nanophotonic devices and systems*. Woodhead publishing, 2014.

[70] Bülent Öktem, Ihor Pavlov, Serim Ilday, Hamit Kalaycıoğlu, Andrey Rybak, Seydi Yavaş, Mutlu Erdoğan, and F Ömer Ilday. Nonlinear laser lithography for indefinitely large-area nanostructuring with femtosecond pulses. *Nature Photonics*, 7(11):897–901, 2013.

[71] George M Whitesides and Bartosz Grzybowski. Self-assembly at all scales. *Science*, 295(5564):2418–2421, 2002.

[72] Pete Vukusic and J Roy Sambles. Photonic structures in biology. *Nature*, 424 (6950):852–855, 2003.

[73] Richard M Parker, Giulia Guidetti, Cyan A Williams, Tianheng Zhao, Aurimas Narkevicius, Silvia Vignolini, and Bruno Frka-Petesic. The self-assembly of cellulose nanocrystals: Hierarchical design of visual appearance. *Advanced Materials*, 30(19):1704477, 2018.

[74] C Nadir Kaplan, Ning Wu, Shreyas Mandre, Joanna Aizenberg, and Lakshminarayanan Mahadevan. Dynamics of evaporative colloidal patterning. *Physics of Fluids*, 27(9):092105, 2015.

[75] Richard D Piner, Jin Zhu, Feng Xu, Seunghun Hong, and Chad A Mirkin. " dip-pen" nanolithography. *Science*, 283(5402):661–663, 1999.

[76] Benjamin Hatton, Lidiya Mishchenko, Stan Davis, Kenneth H Sandhage, and Joanna Aizenberg. Assembly of large-area, highly ordered, crack-free inverse opal films. *Proceedings of the National Academy of Sciences*, 107(23): 10354–10359, 2010.

[77] Joseph J Richardson, Jiwei Cui, Mattias Bjornmalm, Julia A Braunger, Hirotaka Ejima, and Frank Caruso. Innovation in layer-by-layer assembly. *Chemical Reviews*, 116(23):14828–14867, 2016.

[78] Michael A Boles, Michael Engel, and Dmitri V Talapin. Self-assembly of colloidal nanocrystals: From intricate structures to functional materials. *Chemical Reviews*, 116(18):11220–11289, 2016.

[79] Marek Grzelczak, Jan Vermant, Eric M Furst, and Luis M Liz-Marzán. Directed self-assembly of nanoparticles. *ACS Nano*, 4(7):3591–3605, 2010.

[80] Younan Xia and George M Whitesides. Soft lithography. *Annual review of materials science*, 28(1):153–184, 1998.

[81] Elias Nakouzi and Oliver Steinbock. Self-organization in precipitation reactions far from the equilibrium. *Science Advances*, 2(8):e1601144, 2016.

[82] Zerong Xing, Genpei Zhang, Jiao Ye, Zhuquan Zhou, Jianye Gao, Bangdeng Du, Kai Yue, Qian Wang, and Jing Liu. Liesegang phenomenon of liquid metals on au film. *Advanced Materials*, 35(7):2209392, 2023.

[83] Haiyan Qiao, Shengtong Sun, and Peiyi Wu. Non-equilibrium-growing aesthetic ionic skin for fingertip-like strain-undisturbed tactile sensation and texture recognition. *Advanced Materials*, page 2300593, 2023.

[84] Masaki Itatani, Qing Fang, István Lagzi, and Hideki Nabika. Phase separation mechanism for a unified understanding of dissipative pattern formation in a liesegang system. *Physical Chemistry Chemical Physics*, 24(4):2088–2094, 2022.

[85] Christiaan T van Campenhout, Daniël N Ten Napel, Martin van Hecke, and Willem L Noorduin. Rapid formation of uniformly layered materials by coupling reaction–diffusion processes with mechanical responsiveness. *Proceedings of the National Academy of Sciences*, 119(39):e2123156119, 2022.

[86] Roché M. Walliser, Rita Tóth, István Lagzi, Daniel Mathys, Laurent Marot, Artur Braun, Catherine E. Housecroft, and Edwin C. Constable. Understanding the formation of aligned, linear arrays of ag nanoparticles. *RSC Advances*, 6:28388–28392, 2016.

[87] István Lagzi and Daishin Ueyama. Pattern transition between periodic liesegang pattern and crystal growth regime in reaction–diffusion systems. *Chemical Physics Letters*, 468(4-6):188–192, 2009.

[88] ME Losi, C Amrhein, and WT Frankenberger Jr. Environmental biochemistry of chromium. *Reviews of Environmental Contamination and Toxicology*, pages 91–121, 1994.

[89] Toshizo Isemura. Studies on rhythmic precipitates. *Bulletin of the Chemical Society of Japan*, 14(6):179–237, 1939.

[90] Masaki Itatani, Qing Fang, Kei Unoura, and Hideki Nabika. Role of nuclei in liesegang pattern formation: Insights from experiment and reaction-diffusion simulation. *The Journal of Physical Chemistry C*, 122(6):3669–3676, 2018.

[91] Rita Zakhia Douaihy, Mazen Al-Ghoul, and Mohamad Hmadeh. Liesegang banding for controlled size and growth of zeolitic-imidazolate frameworks. *Small*, 15(28):1901605, 2019.

[92] Christopher Palmer and Erwin G Loewen. *Diffraction grating handbook*. Newport Corporation New York, 2005.

[93] Cletus J Kaiser. *The capacitor handbook*. Springer Science & Business Media, 2012.

[94] E Unal, A Gokcen, and Y Kutlu. Effective electromagnetic shielding. *IEEE Microwave magazine*, 7(4):48–54, 2006.

[95] Douglas Philp and J Fraser Stoddart. Self-assembly in natural and unnatural systems. *Angewandte Chemie International Edition in English*, 35(11):1154–1196, 1996.

[96] Pamela Knoll and Oliver Steinbock. Inorganic reactions self-organize life-like microstructures far from equilibrium. *Israel Journal of Chemistry*, 58(6-7): 682–692, 2018.

[97] Wim L Noorduin, Alison Grinthal, Lakshminarayanan Mahadevan, and Joanna Aizenberg. Rationally designed complex, hierarchical microarchitectures. *Science*, 340(6134):832–837, 2013.

[98] Zhihao Bao, Michael R Weatherspoon, Samuel Shian, Ye Cai, Phillip D Graham, Shawn M Allan, Gul Ahmad, Matthew B Dickerson, Benjamin C Church, Zhitao Kang, et al. Chemical reduction of three-dimensional silica micro-assemblies into microporous silicon replicas. *Nature*, 446(7132):172–175, 2007.

[99] Nicolas Vogel, Markus Retsch, Charles-André Fustin, Aranzazu Del Campo, and Ulrich Jonas. Advances in colloidal assembly: the design of structure and hierarchy in two and three dimensions. *Chemical Reviews*, 115(13):6265–6311, 2015.

[100] Jie Zhang, Jing Yan, and Steve Granick. Directed self-assembly pathways of active colloidal clusters. *Angewandte Chemie*, 128(17):5252–5255, 2016.

[101] Mateusz Odziomek, Fanny Thorimbert, Cedric Boissiere, Glenna L Drisko, Stephane Parola, Clément Sanchez, and Marco Faustini. Periodic nanoporous inorganic patterns directly made by self-ordering of cracks. *Advanced Materials*, 34(36):2204489, 2022.

[102] Christiaan T van Campenhout, Hinco Schoenmaker, Martin van Hecke, and Willem L Noorduin. Patterning complex line motifs in thin films using immersion-controlled reaction-diffusion. *Advanced Materials*, 35(39):2305191, 2023.

[103] J Boissonade, E Dulos, and P De Kepper. Turing patterns: from myth to reality. In *Chemical waves and patterns*, pages 221–268. Springer, 1995.

[104] JF Hamilton. The silver halide photographic process. *Advances in Physics*, 37 (4):359–441, 1988.

[105] Robert Hirsch. *Seizing the light: a social & aesthetic history of photography*. Taylor & Francis, 2017.

[106] Steve Anchell. *The Darkroom Cookbook*. Routledge, 2016.

[107] Vladimir P Oleshko. I. photographic process and structure/morphology relationships. *Industrial Applications Of Electron Microscopy*, page 51, 2002.

[108] Bob D Guenther and Duncan Steel. *Encyclopedia of modern optics*. Academic Press, 2018.

[109] Marloes Bistervels, Niels Hoogendoorn, Marko Kamp, Hinco Schoenmaker, Albert Manfred Brouwer, and Willem Noorduin. Light-controlled morphological development of self-organizing bioinspired nanocomposites. *Nanoscale*, 2024.

[110] Philip Ellis. Gold in photography: Evolution from early artistry to modern processing. *Gold Bulletin*, 8:7–12, 1975.

[111] Tim Rudman. *The Photographer's Toning Book: The Definitive Guide*. Amphoto Books, 2003.

Summary

Spatial organization of components can enhance and exceed properties of materials beyond what would be achievable by simply the sum-of-their-parts. As such, precise patterning of components is key for the next generation of materials. Specifically, precise micro- and nanoscale patterning is critical for the generation of complex functional materials with advanced optical, thermal and electronic properties. However, manufacturing of such patterns remains challenging, with costly lithography techniques being the leading method to produce nanoscale complexity. Therefore, straightforward and scalable strategies towards functional patterning are highly sought after.

Alternative strategies can perhaps be found in the natural world: nature possesses the remarkable ability to produce complex shapes seemingly out of thin air. These *grown* patterns are certainly a match in terms of complexity and functionality for the patterns we so painstakingly create, and demonstrate the potential of spontaneous pattern formation for the fabrication of advanced materials. For this, nature employs self-organization of self-assembly: autonomous processes where building blocks spontaneously arrange into complex shapes and patterns, driven by local physical and chemical interactions.

To study this potential of self-organization for scalable fabrication of complex patterned materials, we have investigated reaction-diffusion processes, where a delicate interplay between reaction kinetics and diffusion spontaneously induces pattern formation. Because these processes rely on chemical feedback loops, there is the potential to achieve large scale production of uniform patterns. One class of reaction-diffusion process shows great potential for this goal: Liesegang patterning. In Liesegang patterning, precipitation or crystallization is induced by diffusing a first reagent into a gel matrix containing a second reagent, which together form an insoluble product. Surprisingly, in some cases, this precipitation occurs not evenly distributed throughout the gel, but rather appears in distinct precipitation band or stripe patterns.

This periodic precipitation behavior is explained by an autocatalytic nucleation-growth-depletion mechanism, leading to Liesegang pattern formation. Because precipitation is induced by diffusion of a reagent, Liesegang patterns classically show specific undesirable characteristics: precipitation bands grow increasingly further apart and wider the further patterning occurs from the initial reagent interface. These characteristics instilled by diffusion drastically limit the applicability of Liesegang patterning for the fabrication of large-scale functional materials.

In this thesis, we demonstrate that the classical limitations of Liesegang patterning can be overcome, to enable reaction-diffusion driven self-organization of complex functional materials. We have developed fundamentally new principles for Liesegang patterning, allowing for the formation of large-scale, highly uniform, tunable and customizable patterns.

Specifically, in **chapter 2** we show that diffusive limitations of Liesegang patterning can be overcome by embedding the process in mechanically responsive hydrogels. Here, coupling a moving reaction front to hydrogel contraction induces the self-regulated opening of a transport channel, through which species can freely flow. The transport channel allows for a unique combination large-scale flow of material with short-range diffusion, ensuring controlled reaction-diffusion driven pattern formation at the reaction front. This unique combination ensures rapid and uniform patterning, and allows for the formation of large scale ($>$5 cm) uniform banding patterns with tunable band distance. As chemical transport plays essential roles in artificial and natural processes, we envisage that using mechanically active materials to bypass diffusion limitations will enhance our understanding of, and control over, chemical transport in complex artificial and living matter.

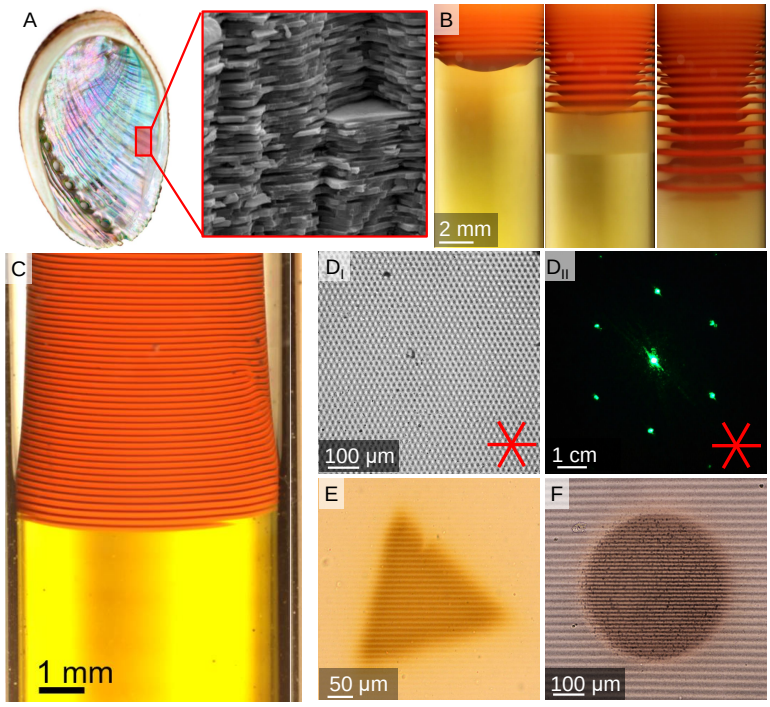

Figure: Guiding Lines: a study into the potential of self-organization for scalable fabrication of complex patterned materials. (A) Irridiscent nacreous shell, where the coloration comes from highly ordered nanoscale building blocks. (B) The archetypical silver dichromate Liesegang pattern, grown by diffusing silver nitrate into a gel containing potassium dichromate. (C) Highly uniform pattern of silver dichromate grown in chapter 2 by incorporating the Liesegang in a mechanically responsive hydrogel. (D) Microscopic line patterns made in chapter 3 with R-DIP, here stacked threefold at 60° angles to create a triangular diffraction grating. (E) Contoured micropattern created in chapter 4 through photosensitization and subsequent UV-masking. (F) Micropattern stack demonstrating the full design customizability of self-organized micropatterned films combined with photography inspired manipulation processes.

In **chapter 3** we apply what we have learned about chemical transport and Liesegang patterning, and come up with a completely new strategy: reaction-diffusion driven, immersion controlled patterning (R-DIP). In this self-organization strategy, immersion of hydrogel thin-film controls the movement of a reaction-diffusion front, inducing highly uniform stripe formation. Here, a balance between the immersion speed and diffusion provides both hands-on tunability of the line spacing ($d = 10 - 300$ μm) as well as error-correction against defects. We demonstrate the scalability of R-DIP by growing a microscopic pattern in an A4-sized thin film, which acts as a diffraction grating. Additionally, by applying R-DIP to several Liesegang patterning processes, we produce uniform line patterns of silver dichromate, silver chromate, lead carbonate and silver/silver oxide nanoparticles. Through combinatorial stacking of different line patterns, we create hybrid materials with multi-dimensional patterns such as square-, diamond-, rectangle- and triangle-shaped motifs. Lastly, using this stacking approach, we create an opto-mechanical compression sensor based on Moiré patterning. Overall, R-DIP offers a versatile and scalable approach for creating complex user-defined line motifs in thin films, enabling a wide range of applications in materials science and manufacturing.

With diffusive limitations tackled, we aim to increase pattern customizability in **chapter 4**. Reaction-diffusion patterning limits the customizability of patterns that can be generated: 1. the large-scale uniformity restricts user-control in shaping where patterning occurs; 2. the necessary delicate interplay between reaction and diffusion requires specific combinations of materials, limiting the choice in chemical composition of patterns; 3. the autonomous nature of reaction-diffusion prevents the formation of complex and user-defined patterns. In this chapter, we introduce a synergistic approach, combining hands off self-organization with hands on customization. Specifically, we show that photographic manipulation processes can be applied for top-down customization of self-organized micropatterned thin-films (MPF's). Because of chemical similarities between micropatterned thin films and classical silver halide photographs, we are able to apply over a century's worth of darkroom techniques to develop, bleach, expose, fix and contour MPF's into user-defined complex shapes. Furthermore, we show that photographic toning processes can convert MPF's, thereby expanding the choice of chemical composition for these patterns. Akin to composition photography, we produce stacks of MPF layers, each with independently designed shape and chemical composition, to produce highly complex patterned motifs. Building upon our results, we foresee that other interesting photographic reactions and processes can be extended to fields outside of photography. Specifically, we project exciting opportunities for the field of ion-exchange, where insights from photographic toning processes could inspire the design of new conversion reactions for components with advanced functionalities.

In the final **chapter 5**, we describe the numerical reaction-diffusion models used throughout this thesis. These models accurately reproduce the experimental patterning behavior observed, and have been used to analyze the broad parameter space of the Liesegang process.

In short, in this thesis we have explored how to overcome several limitations of reaction-diffusion patterning, with the goal of enabling scalable manufacturing of functional patterned materials. In doing so, we are now able to grow and shape extremely uniform patterns on large-scale and with hands-on tunability. However, for the next-generation of advanced functional materials the patterns shown in this thesis are simply too large: comparing the nacreous shell from chapter 1 to the smallest micropatterned thin-films ($d = 7$ μm) from chapter 3 reveals that downscaling of patterns to sub-micrometer distances is crucial. Using numerical modeling, we have gained insights into the key parameters towards this downscaling: the immersion speed, the mobility of species and the rate of nucleation. For future work, screening this parameter space experimentally would be of great interest. I believe that by performing the Liesegang process with the right experimental conditions, downscaling reaction-diffusion patterning to the nanoscale is almost certainly possible.

Samenvatting

Door onderdelen ruimtelijk te ordenen kunnen materialen toepassingen krijgen die superieur zijn aan de individuele materiaal eigenschappen. Zodoende is het precies ordenen van onderdelen cruciaal voor de volgende generatie materialen. Specifiek micro- en nanoschaal fabricage is van groot belang voor het maken van materialen met geavanceerde optische, thermische en elektronische eigenschappen. Echter, het maken van dit soort materialen blijft uitdagend, met dure lithografie technieken als meest gebruikte techniek om patronen op de nanoschaal te producen. Daarom is het van groot belang om eenvoudige en schaalbare strategieën te ontwikkelen voor het maken van functionele patronen.

Alternatieve routes kunnen wellicht gevonden worden in de natuur: in de natuur ontstaan complexe vormen en patronen schijnbaar uit het niets. Deze **gegroeide** patronen doen qua complexiteit en functionaliteit niet onder aan de patronen die wij met veel moeite fabriceren, en laten de potentie zien van het spontane patroonformatie voor het maken van geavanceerde materialen. Voor deze patroonformatie benut de natuur zelforganisatie of zelfassemblage: autonome processen waar bouwblokken spontaan ordenen in complexe vormen en patronen als gevolg van lokale fysische en chemische interacties.

Om deze potentie van zelforganisatie voor eenvoudige fabricage van complexe patronen te onderzoeken hebben wij gekeken naar reactie-diffusie processen, processen waarbij een fijne balans tussen reactie kinetiek en diffusie spontaan tot patroonformatie leiden. Omdat deze processen gebruik maken van chemische terugkoppeling is er de potentie om op grote schaal regelmatige patronen te maken. Een soort reactie-diffusie proces lijkt hiervoor erg geschikt: Liesegang patroonformatie. Bij Liesegang patroonformatie wordt een neerslagreactie uitgevoerd in een gel, door een reagens de gel in te laten diffunderen, waar de tweede reagens al in opgelost zit. Samen vormen deze reagentia een slecht oplosbaar product, waardoor kristallen neerslaan. Verassend genoeg vormt deze neerslag zich niet overal in de gel, maar in specifieke banden of strepen. Deze periodieke neerslagvorming wordt verklaar door een autocatalytisch nucleatie-groei-depletie mechanisme. Omdat de neerslagreactie gestart wordt door diffusie van een reagens laten Liesegang patronen vaak ongewenste karakteristieken zien: neerslagbanden groeien steeds breder en verder van elkaar af naar mate het proces zich dieper in de gel afspeelt. Deze diffusieve karakteristieken beperken de toepasbaarheid van Liesegang patronen voor het maken van functionele materialen.

In dit proefschrift laten we zien dat deze klassieke beperkingen overkomen kunnen worden, om zo met reactie-diffusie processen complexe functionele materialen te groeien. We hebben fundamenteel nieuwe principes voor Liesegang patroonformatie ontwikkeld, waarmee we op grote schaal extreem regelmatige, afstelbare en aanpasbare patronen kunnen creëren.

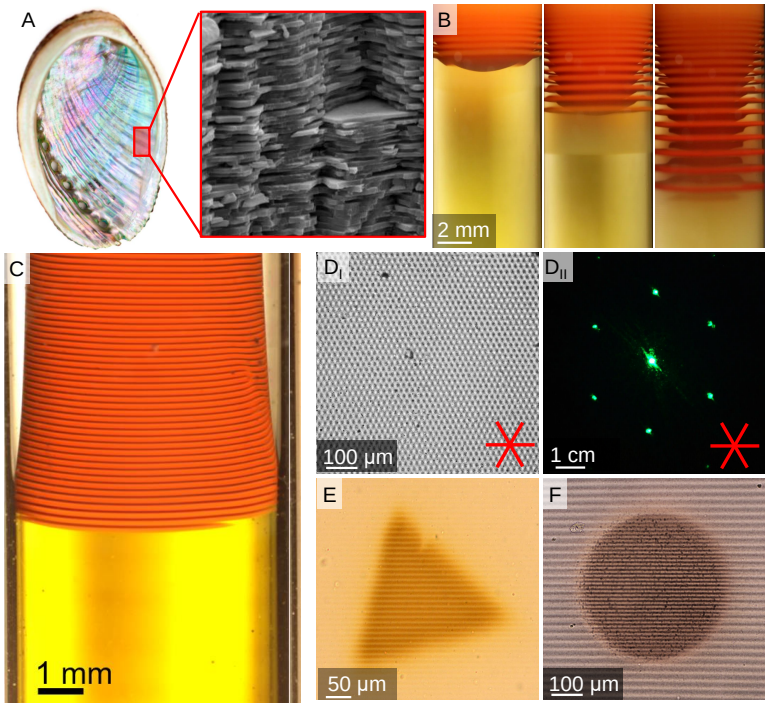

Figuur: Guiding Lines: een onderzoek naar de mogelijkheden van zelforganisatie als een methode om materialen met complexe patronen te creëren. (A) Iridiscentie van parelmoer, waar de kleur afkomstig is van op nanoschaal geordende bouwblokken. (B) Het archetypische Liesegang patroon van zilver dichromaat, gegroeid door diffusie van zilvernitraat in een gel met natrium dichromaat. (C) Extreem regelmatige zilver dichromaat patronen gegroeid in hoofdstuk 2 door het Liesegang proces te koppelen aan een mechanisch responsieve hydrogel. (D) Microscopische strepen gegroeid in hoofdstuk 3 met behulp van R-DIP, hier driedubbel gelaagd onder een hoek van 60° om zo een driehoekig diffractierooster te maken. (E) Driehoekig gecontourd patroon gemaakt in hoofdstuk 4 door het eerst lichtgevoelig te maken en vervolgens te vormen met ultraviolet licht. (F) Twee micropatronen gestapeld, beide met andere vorm, chemische samenstelling en streepafstand om de ontwerp mogelijkheden te demonstreren van zelforganisatie gecombineerd met fotografische manipulatie processen.

In **hoofdstuk 2** laten we zien dat de diffusieve beperkingen van Liesegang patroonformatie verholpen kunnen worden door het proces uit te voeren in een mechanisch responsieve hydrogel. Doordat het bewegende reactiefront gekoppeld wordt aan mechanische krimp opent er een zelf-regulerend transportkanaal, waardoor reagentia kunnen stromen. Dit transport kanaal zorgt voor een unieke combinatie van stroming op grote schaal en diffusie op korte schaal, waardoor bij het reactie-front het proces gecontroleerd plaatsvindt. Deze unieke combinatie zorgt voor extreem regelmatige patroonformatie op grote schaal ($> 5cm$), met afstelbare streepafstand. Aangezien chemisch transport een essentiële rol speelt in veel artificiële en natuurlijke processen, voorzien wij dat het gebruik van mechanisch actieve materialen ons begrip van, en onze controle over, chemisch transport in complexe artificiële en levende materialen zal verbreden.

In **hoofdstuk 3** passen we de lessen over chemisch transport en Liesegang patroonformatie toe en ontwerpen we een compleet nieuwe strategie: dompelgecontroleerde reactie-diffusie (R-DIP). Bij deze strategie controleert het onderdompelen van een hydrogel dunne-film de beweging van een reaction-diffusie front, wat leidt tot het vormen van extreem regelmatige streeppatronen. Een balans tussen de onderdompel snelheid en diffusie geeft ons controle over de streepafstand ($d = 10 - 300$ μm) en autonome foutcorrectie tegen defecten. We laten zien dat R-DIP schaalbaar is door een microscopisch patroon te groeien op A4 formaat, wat opereert als diffractierooster. Daarnaast passen we R-DIP toe op verschillende Liesegang systemen en maken zo patronen van zilver dichromaat, zilver chromaat, loodcarbonaat en zilver/zilver oxide nanodeeltjes. Door deze patronen over elkaar heen te leggen creëren we hybride materialen met multidimensionele patronen, zoals vierkanten, diamanten, rechthoeken en driehoeken. Met deze strategie maken we vervolgens een opto-mechanische compressie sensor gebaseerd op Moiré patronen. R-DIP biedt een eenvoudige en schaalbare oplossing voor het maken van complexe ontwerpen, voor verschillende toepassing in materiaalkunde en microfabricage.

Met de diffusieve beperkingen opgelost, onderzoeken we in **hoofdstuk 4** of de aanpasbaarheid van patronen uitgebreid kan worden. Reactie-diffusie geeft namelijk om verschillende redenen een beperkte set aan patronen: 1. de regelmatigheid op grote schaal beperkt de controle over waar patronen eindigen; 2. de benodigde precieze balans tussen reactie en diffusie vereist specifieke materialen, wat de keuze in chemische samenstelling beperkt. 3. de autonomie van reactie-diffusie processen beperkt de complexiteit van patronen. In dit hoofdstuk introduceren we een synergistische strategie, waar we zelf-organisatie verrijken met fotografische manipulatie processen. Specifiek laten we zien dat gegroeide microscopische patronen (MPF's) aangepast kunnen worden met eeuwenoude fotografische processen. Omdat de chemische samenstelling van MPF's en zilverhalide foto's erg op elkaar lijken, zijn we in staat meerdere donkere kamer technieken te gebruiken om zo micropatronen te ontwikkelen, bleken, belichten, fix en contouren in complexe ontworpen vormen. Daarnaast laten we zien dat toning reacties de chemische samenstelling van micropatronen kan omzetten, om zo de materiaalkeuze van gegroeide micropatronen uit te breiden. Vergelijkbaar met composietfotografie leggen we lagen van micropatronen over elkaar heen, waarbij elke laag een unieke chemische samenstelling, vorm en streepafstand kan hebben. Gebaseerd op deze resultaten verwachten wij dat er meerdere fotografische processen bestaan die interessant zijn voor onderzoeksgebieden buiten de fotografie. Specifiek verwachten we ontiwkkelingen op het gebied van ion-omzettingsreacties, waar inzichten vanuit de fotografie tot het ontwerp van nieuwe reacties kan leiden.

In het laatste **hoofdstuk 5** beschrijven we het numerieke reactie-diffusie model wat in dit proefschrift gebruikt is. Deze modellen beschrijven accuraat de experimentele patronen en zijn gebruikt om de grote parameter ruimte van het Liesegang proces te onderzoeken.

In dit proefschrift hebben we onderzocht hoe verschillende beperkingen van reactie-diffusie patroonformatie verholpen konden, met als doel om schaalbare functionele patronen te kunnen groeien. Zodoende zijn we nu in staat om op grote schaal regelmatige en ontwerpbare patronen te creëren. Echter, voor de geavanceerde toepassing die in dit proefschrift genoemd worden zijn deze patronen simpelweg te groot: als we de parelmoerschelp vergelijken met de kleinste strepen gegroeid zien we dat de patronen een orde-grootte te groot zijn, en dat patronen naar de sub-micrometer schaal teruggebracht moeten worden. Met ons model hebben we laten zien wat hiertoe de belangrijkste parameters zijn: de onderdompelsnelheid, de mobiliteit van reagentia en snelheid van nucleatie. Voor toekomstig onderzoek is het screenen van deze parameters dus erg interessant. Ik geloof dat, door het Liesegang proces onder de juiste experimentele condities uit te voeren, reactie-diffusie patroonformatie op de nanoschaal zeker mogelijk is.

Publications

Included in this thesis:

- Chapter 2: C. T. van Campenhout, D. N. ten Napel, M. van Hecke and W. L. Noorduin, *Proc. Natl. Acad. Sci*, **2022,**119(39):e2123156119.
- Chapter 3: C. T. van Campenhout, H. Schoenmaker, M. van Hecke, and W. L, Noorduin. *Adv. Mater.*, **2023,** 5(39): 2305191.
- Chapter 4: C. T. van Campenhout, M. H. Bistervels, J. Rietveld, H. Schoenmaker, M. Kamp, W. L. Noorduin, *Adv. Sci.*, **2024,** 2401625.

Not included in this thesis:

- L. Helmbrecht, S. W. van Dongen, A. van der Weijden, C. T. van Campenhout and W. L. Noorduin, *Environ. Sci. Technol.*, **2023,** 57(49), 20494-20500. L.H., S.D., A.W. and C.C. contributed equally to this work.
- C. T. van Campenhout, S. W. van Dongen, S. A. Rigter, E. C. Garnett, W. L. Noorduin, *Synthesis of organic-inorganic lead halide perovskite nanocrystals in green solvent*, manuscript in preparation C.C, S.D. and S.R. contributed equally to this work.

Acknowledgments

First of all, I have to acknowledge all the wonderful people at AMOLF who made working there an absolute joy. I would like to thank both my incredible supervisors, Wim and Martin: Wim, your enthusiasm and creativity gave me so much motivation during these past years. From writing papers, to brainstorming new ideas working with you always felt easy and after every meeting I was instantly excited to go back into the lab. Martin, although our music tastes may differ (I generally dislike the sound of a disintegrating washing machine), having you around was invaluable and genuinely a lot of fun. After the first 20 minutes of our 1 hour meeting were inevitably spend on discussing anything but science, you were always there to keep the two overeager chemists a bit in check. Thank you both for all the freedom and guidance you have given me. It has made working with you a real pleasure, and our coffees, meetings and lunches will be dearly missed.

Thanks to my paranymphs Sjoerd and Tjip for taking on this special role. Sjoerd, working next to you and collaborating with you was always a pleasure. Especially our day of lead detection experiments, where after a hunt through all of AMOLF we found Intratuin hydrokorrels as the perfect substrate, is a day I will never forget. Tjip, I should maybe put you down as co-author on some of these papers with how often we discussed reaction-diffusion and pattern formation at home. There are too many fond memories to share here, but know that I appreciate you dearly.

I would also like to thank my committee members for taking time out of their busy schedules to be on this committee and giving me incredibly useful comments on my thesis.

Then there is Hinco. To be honest, I was somewhat intimidated by you when I first started, but what an amazing person you are. You take *support* staff to the next level, from the obvious lab and technical support, to always being there for someone when they are going through a difficult time. Take it easy and I hope to see you again sometime on one of your wonderful boat parties!

To the fantastic AFC AMOLF, and especially our captain Dhawal, it was amazing to be part of this great team. What we lack in football skills we more than make up for in spirit.

To my colleagues from the Self-Organizing matter group: you are all amazing people, and I really enjoyed all the time we spend together. Marloes and Arno, working with you in the lab was so much fun. You are incredible persons, and I really missed the both of you during the last stretch of my PhD. Lukas and Hans, even though you finished a bit earlier during my PhD, I learned so much from you and thank you for shaping the group to be as great as it is. Marius and Juan, hit me up if you ever want to go bouldering again. And let me know if the stripes ever go submicron! Ariane, you are an extremely thoughtful person, and it has been a pleasure getting to know you. To Tess and Pepijn, all the best for the coming four years, I am sure it will be great!

I of course have to thank my mom for so many things. In short, she to a very large extent made me the person I am today and I do not think I would be in science without her. Thanks to my dad for showing me how to be creative and that all ideas are worthwhile. And of course, thanks dad for designing this cover with me. Ron, thank you for always being so enthusiastic. Even if my work was sometimes very abstract, you were always eager to learn and hear about it, which I greatly appreciate. Annel, thank you for always being there for me. You mean the world to me, and I am so glad you were by my side during this whole process.